UNIVERSIDADE
BEIRA INTERIOR

Thermoelastic Modelling of Additive Manufacturing by Selective Laser Melting

(versão final após defesa)

Mariana dos Santos Ribeiro

Dissertação para obtenção do Grau de Mestre em

Engenharia Aeronáutica

(mestrado integrado)

Orientador: Professor Doutor Pedro Vieira Gamboa

Co-orientador: Doutor Fernando António dos Santos Simões

Janeiro de 2022

Once an elderly lady told me she dreamed of becoming a pilot, but "flying was not a job for a woman". I am not a pilot, but I am free to make my own decisions.

To the ones that were not given that chance.

Agradecimentos

Gostaria de exprimir o meu profundo agradecimento à Active Space Technologies por me acolher durante este período e àquele que foi o meu orientador, tanto de dissertação como de estágio, Fernando Simões. A sua dedicação, interesse e disponibilidade durante o desenvolvimento deste projeto foram fundamentais para o seu sucesso.

Quero da mesma forma agradecer ao professor Pedro Gamboa por acompanhar este projeto com empenho e por estimular discussões pertinentes e construtivas sobre o mesmo.

Uma palavra de agradecimento aos meus pais por me encorajarem a aceitar os desafios aos quais me proponho, e também aos meus avós e tios, sem nunca esquecer a importância que a tia Manuela teve neste meu trajeto.

Um generoso obrigada àqueles que me acolheram naquela que seria a minha nova casa nos cinco anos seguintes, aos que ingressaram nesta viagem comigo e àqueles que fizeram as suas próprias viagens levando-me num cantinho dos seus corações.

A todos, *obrigada*.

Resumo

O fabrico aditivo representa uma ferramenta poderosa na produção de componentes aeroespaciais leves e otimizados capazes de reduzir a massa do sistema onde estão inseridos e, consequentemente, o consumo de combustível e das emissões de poluentes. Em particular, a combinação de métodos aditivos e ligas de titânio é uma solução atraente para minimizar o peso ao mesmo tempo que confere integridade estrutural ao produto graças às suas excelentes propriedades mecânicas específicas. Os problemas associados ao fabrico de titânio por processos tradicionais, nomeadamente o elevado desperdício de matéria-prima em relação ao material efetivamente aproveitado, podem ser resolvidos através da adoção de métodos aditivos, em particular da Fusão Seletiva a Laser.

A Active Space Technologies começou a investigar soluções de titânio em conjunto com técnicas de fabrico aditivo no âmbito do projeto ADVANSS, cujo intuito era a investigação, desenvolvimento e fabrico de uma estrutura de suporte, o Large Lens Mounting. No entanto, as consideráveis trocas de calor entre o substrato, a cama de pó, a poça de material fundido e o ambiente circundante envolvidas no processo são responsáveis por induzir grandes concentrações de tensões que podem resultar em falhas na peça.

O objetivo principal deste trabalho é o desenvolvimento de um modelo termoelástico capaz de replicar os fenómenos presentes durante a Fusão Seletiva a Laser, incluindo a fusão do material e o posterior arrefecimento, com boa flexibilidade na variação dos parâmetros. Ao prever as tensões térmicas induzidas durante o processo de fabrico é possível estabelecer um conjunto de parâmetros de processamento capazes de mitigar as imperfeições das peças. Um conjunto de objetivos complementares também foi proposto: a realização de estudos paramétricos para prever tensões induzidas por um conjunto específico de parâmetros para uma única camada e, posteriormente, para um componente inteiro, com n camadas; a construção de uma hierarquia de parâmetros de acordo com sua capacidade de minimizar tensões e o enriquecimento das competências da Active Space Technologies no que diz respeito a tecnologias de manufatura aditiva.

A perspectiva é que o conhecimento adquirido com este projeto contribua para o desenvolvimento de um modelo semelhante para otimizar o processo de fabricação do Large Lens Mounting.

Palavras-chave

Fabrico Aditivo de Metais; COMSOL Multiphysics; Transformações de Fase; Tensões Residuais; Parâmetros de Processamento; LiveLink for MATLAB.

Abstract

Additive manufacturing represents a powerful tool for the production of lightweight and optimised aerospace components capable of enabling an overall mass reduction of the system they are embedded in and, consequently, minimising fuel consumption and pollutant emissions. In particular, combining additive methods with titanium alloys is an attractive solution for saving weight while ensuring structural integrity due to their outstanding specific mechanical properties. The problems associated with the manufacturing of titanium by traditional processes, namely the waste of raw material in relation to the material actually utilised, can be solved by the adoption of additive methods, in particular Selective Laser Melting.

Active Space Technologies has been investigating additive-titanium solutions in the scope of the ADVANSS project whose aim was the research, development and manufacturing of a support structure, the Large Lens Mounting. However, the considerable heat exchanges between the substrate, the powder bed, the melt pool and the surrounding environment involved in the process are responsible for inducing large stress concentrations that may cause part failure.

The main objective of this work is the development of a thermoelastic model capable of replicating the phenomena occurring during Selective Laser Melting, including material melting and subsequent cooling, with good flexibility in parameter variation. By predicting thermal stresses induced during manufacturing, it is possible to establish a set of process parameters capable of mitigating part imperfections. A series of complementary goals have been proposed as well: carrying out parametric studies to predict stresses induced by a specific set of parameters for a single layer, and later of a whole component, with n layers; building a hierarchy of parameters according to their ability to minimise stresses; and enriching Active Space Technologies expertise in additive manufacturing technologies.

The prospect is that the knowledge acquired with this project contributes to the development of a similar model that would optimise the fabrication process of the Large Lens Mounting.

Keywords

Metal Additive Manufacturing; COMSOL Multiphysics; Phase Change; Residual Stresses; Process Parameters; LiveLink for MATLAB.

Contents

List of Figures

List of Tables

List of Acronyms

2D	Two Dimensions
3D	Three Dimensions
ABS	Acrylonitrile Butadiene Styrene
AM	Additive Manufacturing
ARTA	Ariane Research and Technology Accompaniment
AST	Active Space Technologies
ASTM	American Society for Testing and Materials
CAD	Computer-aided Design
CSAM	Cold Spray Additive Manufacturing
DAE	Differential Algebraic Equation
DED	Directed Energy Deposition
EASA	European Aviation Safety Agency
EBM	Electron Beam Melting
ESA	European Space Agency
FAA	Federal Aviation Administration
FEA	Finite Element Analysis
FEM	Finite Element Method
GE	General Electric
HAZ	Heat Affected Zone
HIP	Hot Isostatic Pressing
LBM	Laser Beam Melting
LLM	Large Lens Mounting
LOM	Laminated Object Manufacturing
MOXIE	Mars Oxygen In-Situ Resource Utilization Experiment
ODE	Ordinary Differential Equation
PBF	Powder Bed Fusion
PH	Precipitation-hardening
PIXL	Planetary Instrument for X-ray Lithochemistry
PLA	Polylactic Acid
SLA	Stereolithography
SLM	Selective Laser Melting
SLS	Selective Laser Sintering

SMA	Small Mirror Assembly
STL	Stereolithography or Standard Triangle Language or Standard Tessellation Language
TO	Topology Optimisation

Nomenclature

α_m	Mass fraction	1
α_T	Linear coefficient of thermal expansion	K^{-1}
γ	Ratio of specific heats	1
δ	Kronecker delta	1
$\partial\Omega$	Boundary	1
ε	Emissivity of the radiating surface	1
ϵ	Strain	1
η	Energy absorption coefficient of the material	1
ν	Poisson's ratio	1
ρ	Density	$kg\ m^{-3}$
σ	Stress	MPa
σ_a	Stress amplitude	MPa
σ_{comp}	Compressive stress	MPa
σ_{max}	Maximum stress	MPa
σ_{sb}	Stefan-Boltzmann constant	$W\ m^{-2}\ K^{-4}$
$\sigma_{tensile}$	Tensile stress	MPa
ϕ	Porosity fraction	1
θ	Phase indicator	1
Ω	Domain	1
A	Area of the upper surface	cm^2
A_c	Area fraction of the cavities	1
C	Fourth order elastic stiffness tensor	MPa
C_p	Specific heat capacity	$J\ kg^{-1}\ K^{-1}$
C_{p_0}	Average specific heat capacity	$J\ kg^{-1}\ K^{-1}$
E	Young's modulus	GPa
ED_v	Volumetric energy density	$J\ mm^{-3}$
F	Body forces	N
f	Mass fraction	1
H	Enthalpy	J
h	Hatch spacing	µm
h_{cond}	Conductive heat transfer coefficient	$W\ m^{-2}\ K^{-1}$
h_{conv}	Convective heat transfer coefficient	$W\ m^{-2}\ K^{-1}$

I_0	Maximum irradiance	$\mathrm{W\,m^{-2}}$
L	Latent heat	$\mathrm{J\,g^{-1}}$
l	Length of the spiral	cm
$\bar{l}$	Average length of the spiral	cm
k	Thermal conductivity	$\mathrm{W\,m^{-1}\,K^{-1}}$
n	Number of layers	1
n_t	Number of spiral turns	1
P	Laser power	W
Q	Heat source	$\mathrm{W\,m^{-2}}$
$\mathbf{q}$	Heat flux vector	$\mathrm{W\,m^{-2}}$
q_{cond}	Conductive heat flux	$\mathrm{W\,m^{-2}}$
q_{conv}	Convective heat flux	$\mathrm{W\,m^{-2}}$
q_{ext}	Heat flux to the exterior of the build chamber	$\mathrm{W\,m^{-2}}$
q_{rad}	Radiative heat flux	$\mathrm{W\,m^{-2}}$
r'	r-coordinate of an unspecific point	1
r_0	r-coordinate of the centre of the layer	1
r_b	r-coordinate of the border of the layer	1
r_f	r-coordinate of the laser focal point	1
R	Distance from r to r_f	cm
R_{load}	Stress ratio	1
$\bar{R}$	Average radius of the spiral	cm
R_g	Radius of the laser beam	cm
T	Temperature	K
t	Time	s
T_a	Temperature of the gas	K
T_b	Lower temperature of the phase change interval	K
T_{amb}	Ambient temperature	K
t_k	Layer thickness	µm
T_{max}	Maximum temperature	K
T_{pb}	Temperature of the powder bed	K
T_{pc}	Phase change temperature	K
T_{pf}	Temperature of the platform	K
T_{ref}	Strain reference temperature	K
T_t	Higher temperature of the phase change interval	K

$\mathbf{u}_a$	Velocity vector of the gas	$\mathrm{m\,s^{-1}}$
v	Scan velocity	$\mathrm{mm\,s^{-1}}$
$\mathbf{w}$	Displacement vector	mm

Chapter 1

Introduction

1.1 Motivation

The pursuit of flying might have been stimulated by the observation of the soaring birds. Ironically, the biomimicking of flapping wings delayed the fulfilment of the dream. Success was only achieved in 1903 with the acknowledgement of proper methods and principles that allowed for the construction of wings capable of producing sufficient lift and engines capable of generating sufficient thrust [1].

Air mobility has since proven to be an important contribution without which the interconnection of cultures and easy access to distant places, foreign goods and locally unavailable services would not have been possible. This has unleashed a new desire: the age-old dream of learning to fly evolved to become the dream of flying faster and further. However, despite the tremendous impact of aviation in the world's social and economical development [2], aircraft pollution has been receiving increased attention.

Electric aerial vehicles and alternative fuels are perhaps the most sought solutions for the reduction of aircraft emissions; meanwhile, light-weighting solutions have been extensively explored for the same matter. The purpose of reducing the aircraft mass is to increase energy efficiency, i.e., reducing fuel consumption [3], by lowering lift force and thrust needed during flight. This can be achieved by two approaches: (i) replacement of dense materials with lightweight ones and (ii) removal of material where it is not critical for the maintenance of structural integrity. Therefore, one can conclude that, in addition to a decrease in pollutant emissions and fuel consumption, (ii) allows for a cut in material use, while both (i) and (ii) provide a decrease in the final expenses.

The demand for project cost reduction is not exclusive to the aviation sector. Any machine that features a propulsive system can benefit from weight savings and spacecraft are no exception.

Thermoelastic Modelling of Additive Manufacturing by Selective Laser Melting

The invention of the aircraft and the growing curiosity about the extent of the universe inspired the onset of the space age where learning was the purpose of flying. The sky was no longer the limit as space exploration became the new target. Since the launch of the first artificial satellite in 1957, mankind has been able to get a closer look at the farthest reaches of the solar system and to finally walk on a different ground.

Stating that space above Earth's atmosphere is devoid of matter may mistakenly lead one to disregard the threat it represents to the durability of space structures, as degradation can arise from multiple forms of radiation, debris collisions, meteoroid impact and extreme temperatures. Therefore, the need for space components capable of resisting harsh environments justifies the importance of high performance materials used in space, where metals play an important role. The same applies to aircraft structures that must be capable of bearing the various forces acting upon them during flight.

Because of excellent specific mechanical properties, good corrosion behaviour and moderated resistance to high temperatures, titanium alloys are a feasible option for the construction of structural and propulsive components of spacecraft and aeroplanes, namely fuel tanks [4], airframes, jet engines and gas turbines [5].

A problem arises when the low thermal conductivity of titanium is combined with its high reactivity at high temperatures during machining, resulting in increased cost of titanium parts and an enormous waste of material during the process. In fact, the difficulty of machining titanium alloys leads to a buy-to-fly ratio between 12:1 and 25:1 by conventional methods, meaning that 12-25 kilograms of raw titanium are needed to produce 1 kilogram of finalised product [6].

The high cost of titanium alloys increased the demand of a manufacturing technology that wastes as little material as possible. Additive Manufacturing (AM) can reduce the buy-to-fly ratio to between 3:1 and 12:1 [6] - with minimal waste allocated for support structures. At the same time, the possibility of reaction is minimised during the process, as it occurs in a controlled environment, and forming operations are unnecessary.

As opposed to subtractive processes, additive methods allow for the manufacturing of three-dimensional parts through the addition of feed stock in layers without the aid of tools and moulds. For a plethora of reasons, some methods are more appropriate to process one class of materials than others. The selection of metals for aircraft and spacecraft makes it suitable to choose Selective Laser Melting (SLM) as manufacturing method. SLM is a powder bed

laser-based method that represents 54 % of the metal AM market as of 2020 [7] and is mostly responsible for components with complex shapes, high accuracy and adequate mechanical properties.

Additive methods stand out for the ability to create designs that are impossible to achieve using subtractive methods, to reduce material waste and to obtain lightweight high-strength structures that are difficult to manufacture conventionally.

If complex structures were at all possible to manufacture by traditional methods, the process would consume extra time and resources [8]. Additive manufacturing allows for the fabrication of multiple assembled parts as one in a simpler, less expensive and time consuming way, without the need for fasteners, thereby reducing the total weight [9].

The production of final part components by additive methods is responsible for a dramatic reduction of material waste [10]. Moreover, when powder is utilised as feed stock, unused particles can be recycled [11]. Therefore, the reduction of material, energy and other possible costs implies a significant minimisation in environmental impact [12] - not only in the fabrication process, but also in the system where the component is embedded in.

Topologically optimised structures can be obtained by the control of part porosity and by the replacement of bulk material with lattice structures [13]. Another attractive option for the aerospace industry is the possibility of creating components with multiple functions for a more efficient performance in a specific situation such as turbine blades with cooling channels for enhanced heat dissipation.

Furthermore, additive technologies enable the replication of difficult-to-find components (e.g., 30-year old aircraft components) [8] and the production of different personalised parts [10], since there is no added mould making and tooling costs to increase the price of different parts when compared to identical ones; for the same reason, small production batches and quick design changes are easy and economical [14].

The reduction of costs and complications has predicted the partial replacement of conventional methods by additive manufacturing. While complete replacement is a more vulnerable subject, the combination of both additive and subtractive techniques would be ideal to eliminate the obstacles of both procedures and would introduce the interesting possibility of investing in hybrid manufacturing.

The substantial demand for additively manufactured components and the solid expertise on conventional manufacturing already acquired have motivated Active Space Technologies (AST) to engage on the research, development and manufacturing of a support structure in the scope of the ADVANSS project. However, a global lack of information on final part properties is postponing the dissemination of both hybrid manufacturing and additive manufacturing itself. The necessity to fill the literature gap on the subject adds further value to the contribution of Active Space Technologies.

The major hurdle of this technology is the lack of predictability and consistency [15]. The correct set of process parameters (e.g., scanning speed, scanning pattern, laser power, layer thickness and hatch space) varies from part to part and an incorrect selection of these may cause residual stresses and distortions that can jeopardise the entire product. These defects are inherent to the thermal gradients experienced during the process and cannot be avoided, but only minimised [16]. For this reason, numerical models to predict residual stresses and distortions are of great importance.

This thesis describes the development of a thermoelastic model by means of the integration of COMSOL Multiphysics with MATLAB, as well as the determination of a set of process parameters that result in the minimisation of residual stresses in the component developed within the ADVANSS project. Moreover, the identification of global strategies based on process parameters to reduce part stresses is assessed and listed.

1.2 ADVANSS Project

The opportunity to contribute to the manufacturing of lightweight and adaptive space components encouraged Active Space Technologies to accept, in 2018, the challenge proposed by the German multinational OHB. The challenge consisted in the development of a mechanical structure to function as a lens support for a space observatory.

The core of the ADVANSS project (Advanced Additive Manufacturing for High-Recurrence Satellites) was the design and fabrication of the Large Lens Mounting (LLM) by additive procedures in titanium (see Figure 1.1), which strategically resulted in the acquisition of expertise on the topic by AST.

Figure 1.1: Large Lens Mounting: the final result.

In a first approach, a smaller part, the Small Mirror Assembly (SMA), was selected to be designed. The subsequent development of the LLM occurred with the realisation of the pedagogical profits of designing a more complex part. Based on the strict requirements of the project imposed by OHB and ESA, and the ASTM technical regulations, the part design suffered topology optimisation by means of open-source and commercial software. The aim was the minimisation of the final weight while preserving the structural integrity and the functionality of the part [17]. As the foremost titanium alloy used in the space industry, Ti-6Al-4V was utilised for the construction of the structure.

Disregarding some obstacles [17], not only the main goal was achieved but also internal capabilities in metallic AM were matured. Nonetheless, guidelines on the subject are still insufficient to develop a product with good predictability of the final properties. For that reason, a model to predict final distortions and residual stresses with high parameter flexibility represents a valuable tool.

1.3 Research Objectives

The prospects of identifying strategies to minimise final part stresses serve as an incentive for undertaking the studies initiated in the scope of the ADVANSS project. Therefore, the principal objective is to develop a thermoelastic model capable of simulating additive manufacturing by Selective Laser Melting of a whole component (n layers) and predicting thermal-induced stresses, with all the necessary physical aspects and good flexibility in parameter variation (e.g., material properties and simulation time). The prospect is that the knowledge acquired with this project contributes to the development of a similar model that would

optimise the fabrication process of the Large Lens Mounting.

Additionally, in order to better fulfil the primary objective, a series of complementary goals have been proposed:

1. carry out parametric studies to predict stresses induced by a specific set of parameters for a single layer;
2. build a hierarchy of parameters according to their ability to minimise stresses;
3. expand Active Space Technologies expertise on additive manufacturing technologies.

All in all, the model must be able to find the best set of parameters that allow for the manufacturing of a component with the highest possible quality for a certain geometry and material, but that may be applicable to other geometries and materials, allowing for a list of guidelines for the achievement of an optimised manufacturing methodology.

1.4 Thesis Outline

This thesis is structured in a logical and organised manner. A brief description of each chapter is presented below.

Chapter 1 provides a summary of the reasons that motivated the author to perform a stress minimisation analysis, along with an overview of the objectives proposed.

The literature review is described in **Chapter 2** and mentions the basic knowledge needed to fully comprehend this project and the decisions made throughout it. This includes additive metal technologies, industries in which these methods have offered innovative solutions, processable materials, problems of Selective Laser Melting and the state of the art of numerical thermoelastic models.

The formulation of the problem is presented in **Chapter 3** along with the adequate governing equations and boundary and initial conditions for both heat transfer and structural modules, as well as the thermoelastic coupling.

The first model is detailed step-by-step in **Chapter 4**. This chapter is coherently structured, in order to combine each step of the model development with the corresponding explana-

tions.

While **Chapter 5** details the final model, highlighting its progresses regarding the initial model and its validation by means of fatigue studies, **Chapter 6** analyses the results of the parametric simulations, discussing optimisation strategies towards the manufacturing process of the final specimen.

Finally, **Chapter 7** presents the conclusions and future work.

Chapter 2

Literature Review

There is no consensus on the dates additive manufacturing was invented: the majority claims it emerged in the mid-1980s with Stereolithography (SLA) while others believe it was invented long before, in the nineteenth century, with the invention of photo sculpture. Both of these assumptions are correct; as much as photo sculpture could have been the pioneer of 3D printing, additive manufacturing technologies as known today have been more influenced by SLA. In fact, SLA-1 was the first modern AM machine: introduced in 1987, the first sale occurred in 1988 by 3D Systems [18].

When additive manufacturing methods were initially adopted, the aim was almost exclusively the fabrication of prototypes for design verification and marketing purposes [13]. Only later, with further developments and the expiration of founding patents on AM fabrication, these technologies gained popularity in the fabrication of workpieces. Nowadays, the proliferation of low-cost 3D printers for the fabrication of polymeric parts and the development of easy-to-use computer-aided design (CAD) software for the creation of designs resulted in the acquisition of printing technologies by the general public.

This chapter contains a critical synthesis of the state of the knowledge on the topic. The review of the selected concepts is anticipated to assist the full comprehension of the decisions and strategies adopted throughout this thesis.

2.1 Metal Additive Manufacturing Methods

Conventional, or subtractive, manufacturing corresponds to a group of techniques responsible for material removal by means of controlled machining in order to attain a desired shape. By contrast, additive manufacturing enables the fabrication of three-dimensional parts through the addition of feed stock in a layer-wise approach. Without the aid of tools and moulds, this technology only relies on a 3D CAD file that is subsequently converted into a

triangular approximated design file called STL, which also stands for Stereolithography[1], and sliced in layers. Each layer represents a 2D mathematical design that is read by the printing machine. The further fabrication process varies according to the method.

Some of the most relevant AM methods are Vat Photopolymerization, Material Jetting, Powder Bed Fusion (PBF), Directed Energy Deposition (DED), Binder Jetting, Laminated Object Manufacturing (LOM) and Material Extrusion [19]. The range of processable - or at least, suitable - materials for AM depends on the method. Thus, the analysis of metal processes excludes Vat Photopolymerization and Material Jetting.

Powder Bed Fusion represents the largest share of the metal-based AM market in 2020 [7]. According to the type of energy source used, PBF unfolds in two main categories: Laser Beam Melting (LBM) and Electron Beam Melting (EBM). Both heat sources require an adequate control of the chamber atmosphere: when dealing with a laser beam, the build chamber is filled with an inert gas; on the other hand, due to the high energy density of electron beams, the build chamber of EBM processes must be evacuated, so the process occurs in vacuum conditions. The following steps are common to both categories:

1. the platform is lowered by one layer thickness;
2. the powder is spread over the platform, forming a powder bed;
3. the heat source is activated over the powder following a predefined pattern controlled by a mirror galvanometer [14], in the x- and y-directions;
4. as a consequence of the rising of the temperature on the powder bed, the powder forms a melt pool that solidifies as it cools down;
5. when the heat source has passed over the entire layer and all the powder is consolidated, the sequence is repeated until the part is finished.

The differences that distinguish EBM and LBM have an important effect on the final parts: low residual stresses are found in EBM parts when compared to LBM, which allows for the stress relieving treatments to be dismissed [20]. However, vacuum systems increase EBM costs and the nature of the beam makes the process applicable only to electrically conductive powders [21], thereby reducing the range of processable materials [22]. Moreover, while the

[1] there is some inconsistency concerning the definition of STL as it can be found in some documents translated in Standard Triangle Language and Standard Tessellation Language.

cooling process in LBM is assisted by convection, the same does not apply to electron beam methods as vacuum environments cannot sustain convective heat transfer [15] [23].

The PBF methods are mostly responsible for components with complex shapes and high accuracy, which partially results in long manufacturing times. Hence, PBF is specially suitable to produce small parts.

For larger parts, **Direct Energy Deposition** methods are more suitable. These are grouped according to the type of feed stock. Either it is wire or metal powder, the feed stock is deposited directly on the focus of the energy source. The absence of a powder bed in DED gives additional degrees of freedom to the manufacturing process compared to PBF methods, which makes them more suitable for repairing parts or adding features, as feed stock can be added to less accessible surfaces. Thus, welding processes are being replaced by these methods in the repair works due to their complexity, high cost and the lack of precision [15]. DED is able to combine different alloys into a single structure and fabricate large parts at a high manufacturing rate, but with poorer surface quality.

Metal parts, although less commonly, can be produced by **Binder Jetting**. The setup is similar to the one described in PBF methods. However, instead of an energy source to melt the powders, a liquid adhesive is used as agglutination mechanism. When all the layers are glued together, the manufacturing is not completed as the part still requires powders sintering. This implies longer production times than other methods.

Laminated Object Manufacturing is a more peculiar AM process, since metal sheets are used as feed stock. Sheets are supplied from a feed roller to a platform. The first layer is adhered to the platform, where a cutting tool such as laser cuts the sheet with the desired shape. The wasted material is removed, the platform moves down and a fresh metal sheet is rolled into position. The bonding of the layers is obtained by thermocompression by means of a heated roller [24]. The sequence is repeated until the final part is obtained.

LOM is the closest to the conventional processes as a build chamber is not required due to the absence of chemical reactions. Therefore, it is suitable for large parts fabrication, with the additional benefit of being five to ten times faster than other methods [25]. However, LOM is not recommended for the creation of components with structural purposes and good geometric accuracy, which makes it unfeasible for the aerospace industry.

Material Extrusion makes use of thermoplastic filaments that contain metal powder. As

feed stock is forced out of an extruder heated nozzle, it is deposited layer by layer until the workpiece is finished. Additionally, the thermoplastic content in the printed part is removed by thermal or chemical means and a sintering treatment is required afterwards [13].

There is a sixth, more recent manufacturing method that has became increasingly relevant. **Cold Spray Additive Manufacturing** (CSAM) is able to fabricate 3D metal parts and repair built components by means of particle collisions with the part. Fine metal powder particles are accelerated in a high-velocity compressed gas stream. Upon the impact of the particles on the substrate, high kinetic energy causes deformation and a layer is formed by metallurgical and mechanical bonds [13].

All of these methods share advantages and disadvantages when compared to convectional methods.

The increasing demand for metal AM methods primarily comes from the necessity of (i) creating designs that are impossible to achieve using subtractive methods, (ii) obtaining lightweight high-strength structures - which often implies complex designs - and (iii) reducing material waste - that would allow for a minimisation of feedstock and energy costs.

Aeronautical and aerospace industries have a great interest in these benefits. Firstly, the necessity of precise component shapes makes subtractive methods unpractical due to an intrinsic difficulty in fabricating complex designs. Despite complex structures, basic geometries with elaborate assemblies, e.g., a sphere containing another sphere, take more time to manufacture by subtractive processes as parts have to be sliced and assembled, while additive manufacturing enables a faster and simpler fabrication of multiple assembled parts as one, without additional fasteners.

Weight reduction has always been an attractive topic to engineers. Particularly in the aeronautical sector, lighter aeroplanes suggest having more passengers on board, bulkier payloads and higher manoeuvre capacities [26]. However, more recently, a different cause has motivated the implementation of additional measures: the increasing awareness on environmental threats by the aviation sector appeals for a reduction of aircraft emissions.

Alternative options, e.g., electrical aircraft, have contributed to the sustainability of air mobility and approaches regarding the minimisation of weight implicitly have the same impact: by decreasing an aircraft weight, there is a reduction on fuel consumption, which redundantly implies a minimisation of the aircraft take off weight [27].

Light-weighting can be achieved by replacing dense materials with low-density alloys or by means of structural optimisation. Either by controlling porosity or replacing bulk regions with lattice [13] and cellular structures, the latter solution is attained by means of numerical models that estimate where material can be iteratively removed without threatening the structural integrity of the component. The redesign of Airbus A380 seat buckles is a good example of the combination of both light-weighting approaches. The original bulk seat buckles made of steel (8000 kg m^{-3}) were replaced by hollow titanium (4500 kg m^{-3}) buckles manufactured by a LBM process. The optimisation study was conducted by Finite Element Analysis (FEA) in order to ensure safety in case of shock loading. The 155-gram buckle suffered a weight reduction of 55 % corresponding to a saving of 85 grams per buckle. Accounting for the 853 seats in an Airbus A380, the total weight saving reaches about 72.5 kilograms [20].

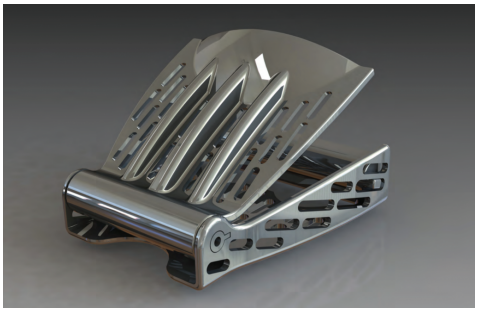

Figure 2.1: Topologically optimised seat buckle manufactured using an LBM process [28].

According to some research [27], saving 1 kilogram can correspond to a 45 000 litres of fuel saving over the life of a large passenger plane. Therefore, Airbus could have saved 3.3 million litres of fuel, which is equivalent to 2.5 million €, whilst the total cost of equipping the A380 with lightweight AM titanium buckles is about 215 000 €.

Topological optimisation (TO) also contributes to the fabrication of multi-functional parts that are only possible thanks to design freedom offered by additive methods. There are some examples of optimised parts for functionalities such as structural, protective, stress distribution, heat dissipation or airflow patterns [29]. For instance, Ferro et al. [30] introduced a single-piece anti-ice component designed to promote heat exchange inside the wing. Ice prevention on an aircraft is vital to preserve aerodynamic performance and the total weight and to allow for proper control of the movable surfaces. The novel system was composed by a sandwich panel with an external aerodynamic skin, an internal skin containing “hot air passageways and feeding tube” and a core produced with a non-stochastic lattice structure.

Weight saving is very convenient for the space industry as well: measuring the cost of space

travel in currency per kilogram, each kilogram launched to Low Earth Orbit costs about 2 050 €, according to Ngo et al. [10]. In this context, a limitation in weight, as well as in material waste, results in a more cost-effective mission.

Some authors claim that AM has a material efficiency of 100 % [31]. However, the utilisation of support structures usually required during the manufacturing and later discarded contradict this statement. Additionally, there is minimal waste assigned to the recycling process.

The utilisation of support structures expand the range of attainable shapes, but their usage might increase surface roughness, manufacturing time and compromise the component after removal [32]. A correct inclination angle could eradicate the need for support, thereby solving these problems. Furthermore, recycling in powder-based methods [11] reflects a significant minimisation in environmental impact [12] during fabrication and the lifespan of the system where the manufactured part is installed.

Aircraft have a long working life - up to 30 years [10]. Consequently, older aircraft components may be difficult to find [8]; alternatively, old parts may be kept in storage, but it would incur an important cost of inventory where stored parts could more easily be damaged [25]. Hence, internal and on demand production is desirable and attainable with additive manufacturing machines. Moreover, it makes feasible the production of different personalised parts [10] as these do not imply additional mould making and tooling costs when compared to identical ones; for that reason, quick design changes, repairs and low volume production are easy and economical [14] and maintenance time is reduced.

The most notable difference between both fabrication classes is probably the method of geometry characterisation: the innovative solution of building a product thought a CAD file offers the possibility of printing the same part in separate places due to its easy access and sharing [10]; in addition, it becomes a more autonomous process.

The next decade is likely to witness a partial replacement of conventional methods by additive manufacturing. Complete replacement is a more sensitive subject owing to the advantages of subtractive methods - that should not be ignored - and the disadvantages of additive methods. In any case, AM metal parts often still require finishing. Hence, additive manufacturing must be seen more as a complementary technique where these methods are merged with machining operations and surface and heat treatments, thereby making it possible to obtain complex parts with improved surface quality and optimal mechanical properties [13]. In the literature, this combination is generally denoted by *hybrid manufacturing*.

Efforts are to be continued in order to overcome some of the novel problems of this manufacturing merger, namely the uncertainty of part dimensions that may interfere with subsequent tooling and cause possible crashes or deficient cutting, contamination and powder oxidation (that an inert atmosphere failed to avoid) [13].

Safety is a key word when it comes to the aviation and aerospace sectors; for that reason, AM components must meet all the requirements and obtain all relevant certifications. The harsh nature materials are subjected to during processing and powder recycling, to name a few, may negatively affect the final result [14]. While interior components, such as furniture and accessories, and some non-structural components are less critical, the failure of structural and propulsive components can cause catastrophic scenarios with irreplaceable losses. Thus, airworthiness and safety must be assured and in accordance with the competent authority.

FAA and EASA, authorities responsible for aircraft regulations, have issued some notices related to the use of AM technologies in aircraft maintenance and modification of components [29]. Additionally, various committees and organisations, in particular ASTM F42 Committee and ISO/TC 261, have been identifying topics for standardisation such as qualification and certification methods, design and powder recycling guidelines, terminology, test techniques and quality controls[2] [7] [14]. Unfortunately, the immaturity of additive processes has hampered the certification task, due to the lack of predictable and repeatable results [15].

Additive manufacturing is a multi-variable process; depending on the manufacturing part, there is a set of process parameters that allows for a higher quality part. An incorrect selection of these parameters may cause discontinuities, e.g., porosity, chemical degradation, cracks and surface roughness, which may jeopardise the entire product. Moreover, residual stresses and distortions have a similar outcome, but unlike other defects, cannot be avoided, but only reduced [16]. If not minimised, these can be responsible for some of the defects aforementioned. For this reason, numerical models to predict residual stresses and distortions are of great importance.

There are other factors responsible for postponing the adoption of this method at a large scale such as mass production, size and material limitations [8].

The high machine and material costs [13] and the relatively low production rates [10] are the principal causes of the impracticality of mass production. Both metal powder production, commonly obtained by atomisation [35], and additive processes are quite energy con-

[2] further details on the current and under development standards for metal AM can be found in [33] and [34].

suming; hence, energy savings would only be applicable to small production batches [29]. Nevertheless, aerospace is a rather strict industry where mass production is not customary.

Part size limitation is mainly a consequence of the small build chambers of the printing machines; even supposing that these were sufficiently big to build larger parts, high stresses and distortions would be an issue.

Because of the high costs of powder production, additive manufacturing materials per weight are more expensive than materials used in conventional methods. However, the low buy-to-fly ratio[3] of the materials processed by additive methods - a consequence of recycling and waste minimisation - counterbalances in part the price of the powders.

Special care must be taken with powder recycling: affected powders - partially melted or highly heated particles - must be removed due to possible contamination during processing that causes changes in the composition of powders and may, therefore, affect the final mechanical properties of a part [13]. Also, collisions during layer deposition and powder recovery may change powder morphology [35]. Moreover, there are health issues when handling metallic powder particles.

2.2 Materials

While there is an extensive knowledge about the application of polymers in 3D printing, where polylactic acid (PLA) and acrylonitrile butadiene styrene (ABS) have a leading role [10], it is not the case with metals. Considering the harsh conditions these materials are submitted to when additively manufactured, the range of processable materials by powder-based methods is rather limited. Generally, weldable and castable metals are suitable for melt-based AM methods [36]. For instance, advanced materials selected for aerospace industries, e.g., titanium and aluminium alloys, nickel-based super-alloys and stainless steels, have been manufactured for that purpose [25]. However, many metal alloys currently used are unsuccessfully processed due to different factors such as high melting temperatures, relatively low viscosities [21] and the creation of inadequate microstructures because of melting and solidification dynamics [10].

The list of commercially available alloys for AM purposes represented in Table 2.1 tends to

[3] a term referring to the weight ratio between the raw material and the manufactured component, mainly used in the aerospace community.

expand with further research. For instance, high-entropy and high-strength alloys, magnetic alloys, metal composites [10], bulk metallic glasses, functionally graded materials and nano-architected metals [7] are some of the new metal options being investigated. Additionally, studies regarding ultrafast lasers, such as femtosecond lasers, are being conducted in order to allow for the materials with a high thermal conductivity (above 100 $W\ m^{-1}\ K^{-1}$) and high melting points (above 3000°C), such as tungsten, rhenium and some ceramics, to be easily processed [10] [37].

Stainless Steel Alloys	**Aluminium Alloys**	**Nickel-based Alloys**
Stainless steel AISI 310	AlSi10Mg	Nickel 200
Stainless steel AISI 316L	AlSi7Mg0.6 A357	Inconel 625
Stainless steel AISI 420	A20X (A205)	Inconel 718
Stainless steel 17-4 PH	Scalmalloy®	Inconel 939
Stainless steel 15-5 PH	M174+	Hastelloy X
Stainless steel CX	AlSi12	Alloy 263/Nimonic 263
Stainless steel M789 Böhler	AlSi9Cu3	Alloy 282/Nimonic 282
Stainless steel W360 Böhler	**Titanium Alloys**	**Other Alloys**
Steel Alloys	Pure Titanium (Grades 1 & 2)	Refractory metals (W, Mo, Ta, Nb)
Maraging steel 1.2709	Ti-6Al-4V Grade 23 ELI	Precious metals (Pt, Rh, Pd, Ag, Au)
E185 Böhler steel	Ti-6Al-4V Grade 5	Co28Cr6Mo
H11, H13, M300 (tool steels)	Titanium Ti6242	Copper alloys (Pure, CuNi2SiCr, CuSn10)

Table 2.1: List of available metallic alloys for additive manufacturing [38] [39] [40] [41].

2.2.1 Stainless Steel and Steel Alloys

Steels started gaining popularity in the early publications of AM laser-based methods [42]. First attempts were reported to be only partially successful due to defects that were only comprehended later. Nowadays, austenitic stainless steels, precipitation-hardening (PH) stainless steels and maraging steels [10] represent about one third of the overall publications about the topic [43], being the vast body of literature about the alloy 316L.

Although lighter materials are preferred over steels for aircraft components, they are still the first choice for components that require structural integrity and corrosion resistance. The fact that they offer good mechanical properties such as high ductility, strength, hardness and wear and corrosion resistance makes it desirable to produce landing gears, fuel tanks, fasteners, turbine components, propeller spinners, etc. [44].

While stainless steels exhibit a good behaviour when in contact with corrosive media at modest temperatures, maraging stainless steels are recommended when corrosion resistance, high strength and hardness are simultaneously required [42]. As long as yield strength, hard-

ness and abrasion resistance are looked for, mainly in the tool making industry, tool steels are the imminent choice.

When additively manufactured, steels exhibit properties that typically match or exceed those of their conventionally produced counterparts, namely hardness, tensile strength and corrosion properties [42]; however, ductility and fatigue behaviour are often found to be poorer.

2.2.2 Aluminium Alloys

Aluminium and its alloys usually account for more than 50 % of an entire aircraft. Good specific strength (with a density of about 2700 kg m^{-3}) and corrosion resistance [45] makes it the material of choice in several aerospace structural applications, e.g., fuselage panels and wing skins. At the same time, these alloys are economical in comparison to titanium alloys. Nevertheless, their high thermal conductivity makes some traditional manufacturing processes such as welding a challenge [35], because of the presence of volatile elements such as zinc.

Additive manufacturing faces similar problems: in addition to a high thermal conductivity, aluminium powders have high reflectivity [10] and low laser absorptivity for the wavelengths commonly used [31]. Furthermore, aluminium is lightweight and has a poor flowability during recoating [35] [45]. On the plus side, its high thermal conductivity contributes to inferior thermal stresses and faster AM processes [10].

Processable aluminium alloys are limited to cast alloys, where attention goes to AlSi10Mg, followed by AlSi12 [10] [31]. The presence of Al-Si eutectic prevents excessive part shrinkage, but offers moderated tensile strength and low ductility.

Alloys with properties suitable for aerospace industries (2xxx, 5xxx, 6xxx and 7xxx series) require significant materials redesign before being considered compatible with AM techniques [31]. Exclusive additive alloys have already been developed, namely Scalmalloy® developed by the Airbus group, but require further maturation. For these reasons, conventional manufacturing methods still have more commercial interest than additive methods for aluminium alloys.

2.2.3 Nickel-based Alloys

Nickel-based superalloys have been particularly designed for aerospace high-temperature applications [10] such as aircraft turbine components. Owing to their outstanding mechanical properties under extremely high temperatures and pressures and in corrosive environments, these alloys can be identified in over 50 % of the mass of an advanced aircraft engine [46]. In addition, their low thermal conductivity, good damage tolerance and oxidation resistance [14] make superalloys difficult to machine due to high tool wear rates [13] and poor surface integrity [47].

The introduction of non-traditional manufacturing methods are of great interest to nickel-based alloys. Superalloys have been successfully manufactured using AM technologies with evidence of a different microstructure when compared to that obtained by cast and wrought methods and mechanical properties that match those of their counterparts [48].

2.2.4 Titanium Alloys

Aerospace and biomedical fields have extensively explored titanium and its alloys for commercial applications [10]. Excellent specific mechanical properties, biocompatibility and corrosion behaviour [20] make it an interesting metal for both fields and encourage the replacement of different alloys such as steel and aluminium. While aluminium is considerably lighter than titanium, steel would preferentially be replaced by titanium because of its outstanding mechanical properties. Due to its inherent strength, less titanium is required in order to achieve the same physical performance of a certain amount of aluminium. Additionally, titanium supersedes aluminium alloys when exceptional corrosion resistance [4] and good composite compatibility are mandatory and aluminium, steel and nickel alloys when high-temperature resistance is a primal requirement [9]. Therefore, the alloys in study are used to manufacture aircraft components such as compressor disks, airframe parts, fuselage and landing gears [44].

On a negative note, the complexity of extraction and machining processes notably raises the cost of titanium. The combination of a low thermal conductivity and high reactivity at high temperatures is responsible for an excessive material waste corresponding to a buy-to-fly ratio as high as 25:1 [7] by conventional methods. Therefore, a procedure capable of manufacturing a near net shape component results in an obvious cost reduction [20], which is a

very attractive solution for titanium and its alloys.

The buy-to-fly ratio of titanium can be minimised to, at least, 12:1 [7] with additive manufacturing. The possibility of reaction during manufacturing is reduced because of the inert gas-controlled environment and machining operations are no longer needed. Furthermore, the additively manufactured components exhibit similar or superior mechanical properties without any post-processing treatments [12], but reduced ductility. Extensive studies have been carried out in order to improve some properties such as fatigue behaviour and ductility [36].

Titanium alloys are divided in three classes, i.e., α, β and $\alpha - \beta$, that, along with other factors, dictate the final properties of a part. The α-alloys exhibit better corrosion and creep resistance and β-alloys reveal high strength and fatigue behaviour, while $\alpha - \beta$-alloys combine the properties of both classes [35]. As a result, $\alpha - \beta$-alloys are extensively used in the fields of interest with special emphasis on Ti-6Al-4V.

Since 1950 [6], Ti-6Al-4V is recognised as the most popular titanium alloy in the aerospace industry for its suitability in designing heavily loaded airframe structures, jet engines, etc. [5]. Nowadays, this alloy represents almost a half of all titanium commercial applications [6].

2.3 Applications

Additive manufacturing has become a prominent technology in areas such as aerospace and biomedical. However, its presence is being intensified in many other fields. In architecture, for example, printing machines symbolise a very powerful tool for architects by being able to rapidly create a detailed 3D model [8] or even a relatively cheap house, identical to the ones massively printed by WinSun, a Chinese architectural firm, in less than a day [10].

Sculptures, furniture and even musical instruments have been created by additive methods as well. For instance, a Yamaha polymer flute was replicated in titanium [49]. The novel instrument offered an innovative design, a richer musical sound (as titanium does not absorb the sound waves), higher lifetime, assembling optimisation and high biocompatibility for touch contact.

3D printers could also be useful during mining projects operated in remote regions [7] as,

for example, in case of equipment failure, access limitation could delay the replacement of goods and, consequently, the project itself.

Other fields are experimenting major changes due to the proliferation of additive manufacturing.

2.3.1 Biomedical

Biocompatibility and corrosion behaviour are crucial properties for medical applications. These combined with the density and mechanical performance of titanium alloys [50] make them exceptional biomaterials for bone transplants, dental crowns, etc. [25].

Bones shapes differ between individuals; due to the design freedom offered by additive methods, it is possible to bioprint a precise porous-controlled transplant with osteoconductivity similar to the original bone. Besides, many parameters can be modified in order to manipulate tissue ingrowth and mechanical properties that can allow for less time recovery and better cosmetic results [8]. Additionally, the mechanical strength of implants can be improved with AM, causing a reduction in the possibility of inflammation due to microdebris.

Besides bones, prosthetics and tissues can be also printed. In fact, in 2019, Israeli researchers bioprinted a vascularised engineered heart using an hydrogel-based bioink. This accomplishment demonstrates the potential of engineering tissues and organs [51] that will eventually assist the discovery of new treatments for heart diseases.

2.3.2 Tooling

Aside from the obvious repercussions of the COVID-19 pandemic, the semiconductor microchip market suffered unexpected consequences. The lack of semiconductors due to the disruption of production threatened the production of systems that require these components. The situation motivated 3D Systems and Diabatix to explore how AM could aim the fast production of semiconductors through a novel design approach that automatically generated optimal self-supporting cooling structures that reduced thermal gradients, maintained fluid pressure within system requirements and presented a reduction in manufacturing time. This solution could have aided the production of the out-of-stock component during this period [52].

Comparatively with the requirements to utilise printed aerospace components, certification processes concerning tooling are less stringent [29]. The combination of this with efficient material usage and complexity increased the interest in printing tooling such as moulds, jigs or dies. Tools would be economical because of the low volume production and could integrate other functionalities.

A good example of the success of AM in tooling is the case concerning the manufacture of an automobile armrest conducted by Innominia [53]. The production of the plastic central armrest is based on a classic injection moulding process, where heat dissipation plays an important role in the quality of the part and controls the production cycle time: as long as the plastic solidifies, the part can be extracted from the mould and the next component produced.

The moulds used to date were made of beryllium-copper alloy and only allowed for heat dissipation from one side of the insert. This caused uneven temperature distribution and, eventually, part distortions. The cooling was assisted by a liquid that needed to be at a very low temperature, causing a raise in energy costs.

Rapid tooling was the solution: customised moulds with conformal channels were manufactured under a PBF technology in order to homogenise the cooling process and impart unique properties to parts [25] (see Figure 2.2). In addition, energy needed for cooling assistance was reduced and the maintenance interval was extended from two to six weeks.

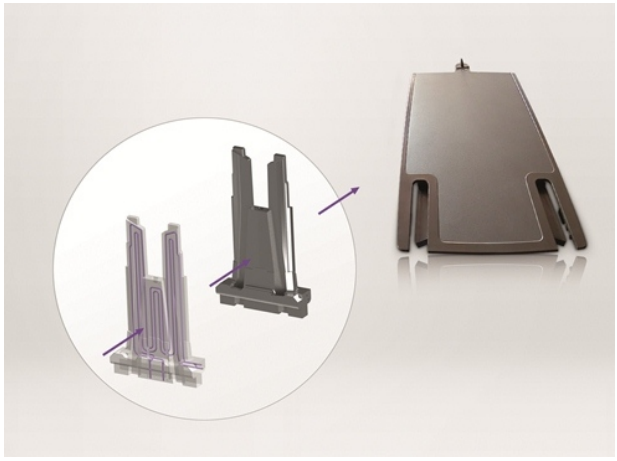

Figure 2.2: Optimised mould with cooling channels for plastic armrests [53].

The creation of rapid tooling emphasises the opportunities given by additive methods in assisting, directly or indirectly, the rapid and improved production of aircraft parts.

2.3.3 Automotive

Recently, Sauber Engineering AG decided to employ its expertise and the technology used to produce high-performance Formula 1 components to manufacture antique car parts, which are difficult to find or no longer exist [54]. One of their latest projects consisted in the manufacturing of a gearbox housing in AlSi10Mg for a classic 1950s Ferrari 340 America Barchetta. Reverse engineering was used to scan the damaged component - shown in Figure 2.3a - into a CAD file, due to lack of engineering drawings. By applying additive manufacturing in this context, the damaged component was not only replaced but also optimised, becoming more reliable and lighter.

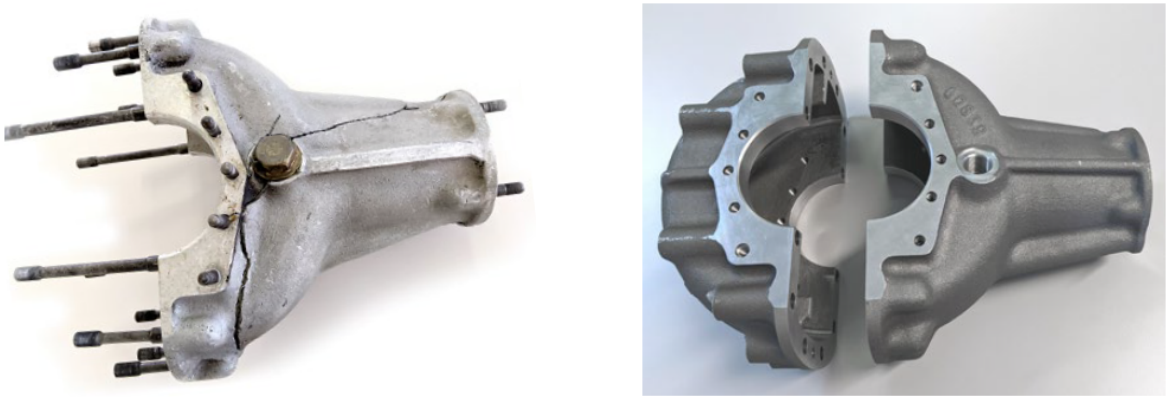

(a) The original and damaged gearbox casing. (b) The redesigned gearbox casing.

Figure 2.3: Gearbox housing for a 1950s Ferrari 340 America Barchetta [54].

An excellent example of the interest of the strength-to-weight ratio of titanium in contrast to aluminium is the Bugatti brake caliper. The titanium alloy Ti-6Al-4V was used to replace aluminium and, as a result, the new caliper weighs about 2.9 kg and has a tensile strength of 1250 MPa [55], in contrast to the aluminium brake caliper that weighted 4.9 kg. Thus, Bugatti was able to save about 40 % of weight while ensuring even higher strength.

Figure 2.4: Titanium eight-piston monobloc brake caliper produced by additive manufacturing technologies [55].

2.3.4 Aerospace

The topologically optimised seat buckle and the single-piece anti-ice component exposed in Section 2.1 are not isolated cases exhibiting the contribution of additive manufacturing to the sector. These technologies have numerous advantages; material saving itself can cause a remarkable reduction of pollutant emissions and material waste, and a significant component improvement, which causes a minimisation of the overall costs of the mission. Particularly, mass reduction in rotational components and launch vehicle rocket engines not only minimises the total weight but also benefits rotational inertia [46].

General Electric (GE) is perhaps a pioneer of engine additive manufacturing. The GE9X engine is composed by 267 printed components that represent more than one-third of the components on the GE9X series engines [46]. The turboprop engine boasts 28 of the LEAP engine fuel nozzles, 228 low-pressure turbine blades, a T25 sensor housing, a combustion mixer, 8 cyclonic inducers and a heat exchanger, all produced by the innovative technology. With the goal of minimising fuel emissions and costs [56], the fuel nozzle tips were manufactured from a cobalt-chrome alloy increasing durability by 5 times and replacing 20 parts with one; the low-pressure turbine blades were built in titanium aluminide (TiAl) resulting in a 50 % weight reduction; the housing of T25 sensor, whose manufacturing resulted in a 30 % more precise part and the replacement of 10 parts with a single one made from cobalt-chrome, was the first FAA certified additive part to fly inside GE commercial jet engines; the combustion mixer was printed in the same material as the sensor housing and its manufacturing resulted in a component 3 times more durable and 6 % lighter; the cyclonic inducer - another cobalt-chrome-made part -, in which 13 parts were combined into one, resulted in a durability two times higher than that obtained by traditional methods; and at last, aluminium F357 was used to produce the heat exchanger as a single part in contrast to 163 traditionally manufactured parts resulting in a product that is 40 % lighter and 25 % cheaper.

In 2017, Norsk Titanium, a Norwegian company, also had the avail of the FAA to manufacture AM components [57]. This time, the components, manufactured from Ti-6Al-4V, integrated the Boeing 787 Dreamliner and were its first structural AM components.

Topological optimisation of the Airbus A320 nacelle hinge bracket (in Figure 2.5) enables the reduction of 40 % of CO_2 emissions during operational time and 64 % of the component mass [46]. The weight savings (from 918 g to 326 g) was a result of the combination of TO and the replacement of the original HC101 steel by the predominant titanium alloy, Ti-6Al-4V.

Figure 2.5: Topologically optimised A320 nacelle hinge bracket [46].

NASA's most recent mission to Mars, Mars 2020, aims at seeking signs of ancient life in addition to collecting samples of rock and regolith for possible return to Earth [58]. This mission relies on the Perseverance rover, which has traces of AM technologies: the rover features 11 components additively manufactured from which six are heat exchangers used in the Mars Oxygen In-Situ Resource Utilization Experiment (MOXIE) and the remaining five are in the Planetary Instrument for X-ray Lithochemistry (PIXL) [46]. The heat exchangers are made of nickel-based superalloys in order to withstand temperatures of over 800°C during the mission. PIXL, on the other hand, was manufactured in Ti-6Al-4V because of its improved mechanical properties [59].

GKN Aerospace together with Airbus Safran Launchers developed the first advanced Ariane 6 nozzle (SWAN) to make part of the Vulcan 2.1 engine [60]. The nozzle measures 2.5 m in diameter (see Figure 2.6) and the additive technology allowed it to enhance its performance, lower production times nearly 30 % and costs nearly 40 % and reduce the number of parts from approximately 1000 to 100. Because of its capabilities to produce larger parts, DED was the method used. The ESA's Ariane Research and Technology Accompaniment (ARTA) Program submitted successfully a demonstrator nozzle to tests. The Ariane 6 is scheduled to enter service in 2022 [61].

Figure 2.6: Advanced Ariane 6 nozzle (SWAN) to be incorporated in the Vulcan 2.1 engine [60].

These examples, a few from the existing ones, irrefutably corroborate the success of additive manufacturing not only in the aerospace industry, but also in numerous others.

2.4 Selective Laser Melting

Selective Laser Melting (SLM) is a Selective Laser Sintering (SLS) successor that was developed with the purpose of manufacturing fully dense parts. Both are Powder Bed Fusion methods, meaning that the process sequence is the one described in Section 2.1. Powder bed not only acts as natural support but also as heat dissipater [5]. A schematic of SLM setup is represented in Figure 2.7.

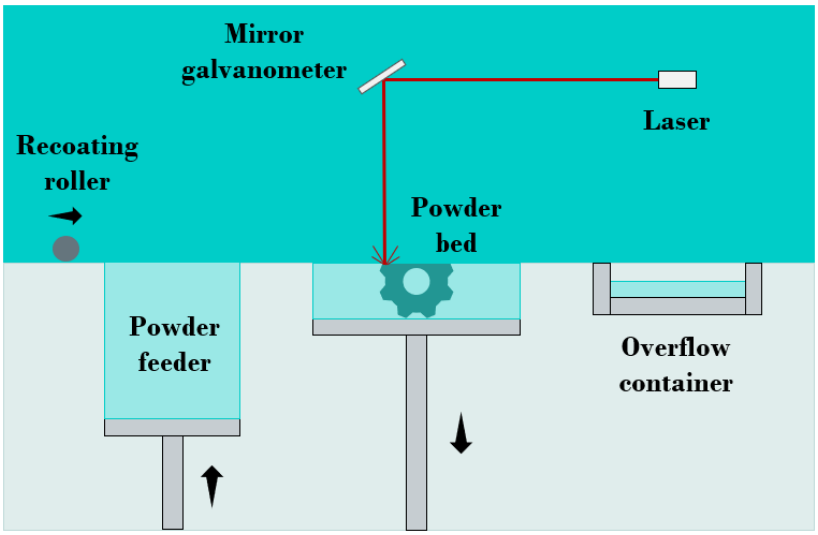

Figure 2.7: Setup of Selective Laser Melting.

SLM involves micro, meso and macroscale physical phenomena, namely laser energy absorption and reflection, heat transfer, phase changes, melt pool dynamics and chemical reactions [50]. As the laser beam draws its path over the powder bed, the temperature of the powder raises above its melting temperature and a melt pool is formed. It is responsible for the adhesion of the current layer to the underlying substrate [62] and its accomplishment depends on many factors, most of which are the focus of mesoscopic studies. Surface tension, capillary forces, the low viscosity of the molten metal and contamination can considerably decrease the adhesion behaviour to the substrate, which can result in Plateau-Rayleigh instability, commonly referred to as the balling effect, poor surface quality, porosity and delamination.

Heat transfer within the pool is governed by the Marangoni convection [21]. Depending on the absorbed energy, the temperature inside the melt pool can exceed the boiling temperature of the material resulting in evaporation, which influences the process due to mass losses. At the same time, heat is conducted in the powder bed and partially dissipated into the argon-filled chamber (by convection and radiation) and the platform (by conduction). During the cooling process, the melt pool solidifies and a solid layer is obtained [63].

The microstructure determines the macroscopic properties of the final part and is characterised by the grain size, morphology and orientation that depend on temperature gradients, cooling and solidification rates. Microscopic models are the tools used to assess grain properties and phase distributions.

Temperature gradients are the main cause of residual stresses and distortions and are observed in two situations: in the heat affected zone and when the previously deposited layers undergo repeated heating and cooling cycles that decrease with increasing layers. This leads to distinct microstructures from the ones observed in conventional processes [9].

Whereas geometry complexity is not a problem, Selective Laser Melting still has some constraints, namely a maximum manufacturable size due to chamber dimensions, low productivity, high machine costs, complex optimisation of process parameters and high surface roughness [16]. Furthermore, post-processing requirements are a vulnerability of this specific method. In fact, parts produced by SLM are seldom used as-built [63].

Electron Beam Melting is currently preferred for metals processing [25], but presents limitations when confronted to Selective Laser Melting. The versatility of SLM and its capabilities to create complex shapes with adequate mechanical properties has distinguished it as the most qualified method to manufacture metallic structures for several industrial applications [63]. Moreover, structural integrity can be improved by the integration of macro- and micro-optimised features such as internal support structures and reinforcement rings [12]. Besides, SLM is free of binders and fluxing agents [32].

The suitability of the method to aerospace metallic components has attracted industries to make an effort to obtain a deep comprehension of the process parameters that are yet experimentally uncertain.

2.4.1 Residual Stresses and Distortions

Residual stresses are stresses that prevail inside a material when it has reached an equilibrium. Not all stresses are detrimental, but are generally undesirable as they result in shape deformations. The amount of residual stresses generated varies with manufacturing process. During Selective Laser Melting and other laser-based methods, steep temperature gradients are introduced to the heat affected zone where a laser beam causes a rapid heating of the surface. The material expands, but is restricted by the base plate or the underlying layers. This originates elastic compressive strains and, as the yield strength of the material is reached, the top layer is plastically compressed [64]. The consequent cooling process induces the thermal contraction of the material. Once more, this deformation is limited by the underlying layers resulting in a distribution of tensile stresses on the top of the layer and compressive stresses below (see Figure 2.8).

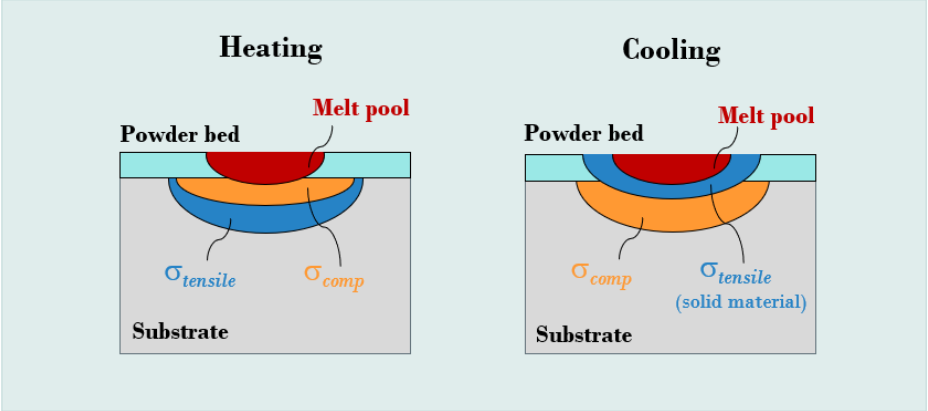

Figure 2.8: Stress distribution during heating and cooling phases, where $\sigma_{tensile}$ and σ_{comp} represent the tensile and compressive stresses, respectively.

After the manufacturing process, the product is removed from the platform, which causes alterations to the stress state due to a relaxation. If post-heat treatments are required to improve part quality, these must be applied before removing the support structures to minimise warping. Distortions are a consequence of the stresses that result in volume changes. In extreme cases, distortions may cause delamination [36].

In order to mitigate residual stresses and distortions, a set of process parameters must be carefully selected.

2.4.2 Part Defects

Porosity. The existence of pores is not always a defect; controlled porosity is used for weight reduction and for tailoring mechanical properties [10]. However, irregular porosity deteriorates the material properties and is caused by the incomplete melting of powder layers, trapped gas in the powder bed, Marangoni turbulences in the melt pool [16] and material evaporation. Porosity results in crack propagation and low ductility [36], and lowers the stress at which fast fracture occurs. In particular, vertically built samples experience a reduction on the effective load bearing area as a consequence of porosity due to lack of fusion, as loading in that direction may open up the pores [12]. Post-processing is commonly used to mitigate uncontrolled pores [6]. However, heat treatments do not close the pores entirely. On the other hand, Hot Isostatic Pressing (HIP) was found to be effective on the reduction of porosity.

CAD Imperfections. Inaccuracies in the final geometry have many explanations. One of them is the poor tessellation when converting a CAD drawing into an STL file. Refining tessellation may solve defects commonly found in curved surfaces [10], but processing of the part will take longer. Alternatively, post-processing may be useful in the correction of some imperfections.

Staircase Effect. The staircase effect is a consequence of the combination of non-vertical surfaces and a high layer thickness [32]. When pronounced, it raises concerns in respect to surface roughness that can compromise fatigue resistance. Moreover, severe inclination angles cannot be processed without support structures. It is recommended that support structures are minimised as it is wasted material that does not contribute to as-used component and adds costs to the manufacturing task [12].

Balling Effect. This defect is caused by the Plateau-Rayleigh instability that causes a long fluid jet to break up into multiple droplets [14] [21]. As the liquid fails to wet the underlying substrate, it spherodises due to the low surface tension [5]. The wetting degree can be reduced by contaminations [36] and inadequate laser energy input along with little liquid content [62]. The formation of balls is responsible for porosity and poor surface finish.

Cracks. Cracks are caused by some of the factors above-mentioned, namely thermal stresses [36] and porosity. The restrictions inhibiting the material to expand and, later, to contract result in permanent tensile residual stresses [65]. While a ductile material can plastically com-

pensate the thermal strain variations, a brittle material cannot withstand the large amount of stress concentrations, which can result in cracks at these locations [21]. Therefore, by minimising thermal stresses, cracks can be avoided.

Surface roughness. The staircase and balling effects, unmelted/semi-melted powders, powders contamination and excessive powder are responsible for increasing poor surface finish which, consequently, promotes stress concentrations and a shorter fatigue life - that represents one of the dominant failure modes for aerospace components [12]. Surface roughness depends on the orientation of the part, the scan strategy, the scan velocity and the hatch space, i.e., the overlap region [14]. By increasing the scanning speed while maintaining the space between two scanning paths, a smaller melt pool is formed and, thus, the overlap region is reduced. Increasing the overlap area could mitigate surface roughness as well as reducing layer thickness [5]. Post-processing treatments are another solution; however, while the first option reduces the production rate, the latter increases production costs [36]. Therefore, a compromise between the two strategies must be evaluated.

Chemical degradation and oxidation. The physical nature of metal manufacturing forces the atmospheric conditions inside the build chamber to be strictly controlled. Improper or insufficient precaution would cause the degradation of the physical and mechanical properties of the materials and to the wetting behaviour [36].

Lack of fusion. Lack of fusion designates the poor and irregular melting of the powder particles causing a deficient adhesion between the new layer and the previous one, mainly caused by insufficient laser power. This disability may incur lower fatigue behaviour and porosity [5]. Additionally, accounting that some particles are insufficiently melted, unmelted powder may possibly be found in the final part as well, which would result in a minimisation of mechanical strength due to the presence of pores.

Anisotropy. The layer-wise building method affects the structural homogeneity of Selective Laser Melting [5]. Anisotropy itself is not exactly a defect, but may be undesirable. Usually, AM metal components exhibit finer microstructures when compared to traditionally manufactured parts due to the manufacturing sequence, which results in enhanced yield and ultimate strengths. However, anisotropy results in the tendency to react differently to stresses applied in the printing direction; a greater resistance in the building direction is commonly found in AM final components [10]. This behaviour can be eliminated by post-heat treatments such as HIP, where the pores caused by insufficient melting are successfully closed

and healed [7] [12].

2.4.3 Process Parameters Influence

Selective Laser Melting concerns a set of parameters that affect the final result. However, their influence is somehow ambiguous and may vary from part to part. The parameters include heat source properties (quantity, power and spot size), scan-related properties (velocity, hatch space and pattern) and powder properties (material, particle shape and size, preheating temperature, powder bed density and layer thickness) [66]. Not all of these parameters are relevant for this study and, therefore, only some of them are reviewed.

Equation 2.1 assists the quantification of the effect that laser power, P, scan velocity, v, hatch spacing, h, and layer thickness, t_k, have on each other and on the volumetric energy density, ED_v.

$$ED_v = \frac{P}{v\, h\, t_k} \quad (2.1)$$

Laser power and scan velocity. The energy deposited on the material layer increases proportionally by increasing laser power, which requires longer or optimised cooling times such that the temperature drops below the solidification point. This effect facilitates full melting, which allows for a higher achievable material density [67], but induces higher temperature gradients and high thermal stresses since the maximum temperature increases, but the minimum remains approximately the same.

At constant velocity, the total absorbed energy density decreases when reducing laser power. Similarly, the total absorbed energy density decreases when the scan velocity increases, considering that the laser power remains constant. The latter scenario is responsible for promoting melt pool instabilities while a reduced laser power may cause lack of powder fusion. A commitment between the two should be established such that the integrity of the part is not compromised.

It becomes clear why these two parameters are grouped together whilst belonging to different categories; they are mutually influenced and, for modelling purposes, can even be considered a single parameter.

Scanning pattern and spacing. A recurrent strategy used to reduce thermal stresses is

the subdivision of the surface into separate “islands” forming a chequerboard pattern [68]. Each “island” is selectively melted in a random order and on each of them, the laser scans different patterns or simply different scan vectors. The space between scan vectors is defined as hatch spacing. A higher building rate is obtained by increasing the scan spacing, but insufficient melting and porosity may be a consequence of this approach.

The effects of scanning patterns on part quality are, in general, uncertain as published literature reports contradicted results for the same parameter variation [69]. However, authors agree that by choosing a proper scanning pattern, final properties can be improved. A review on scanning patterns and their effects can be found in [70].

Layer thickness. High layer thicknesses have a positive effect on the minimisation of residual stresses, which is attributed to a lower absorbed energy density and a prolonged cooling rate. Furthermore, less layers are required to produce the part, hence the processing time is reduced. However, it fosters the staircase effect and decreases the relative density [71].

Preheating. Preheating is found to be one of the simplest approaches to mitigate sharp thermal gradients associated with AM samples. Preheating the powder bed allows for a minimisation of the laser power [14], thereby reducing the magnitude of the maximum temperatures. Furthermore, the base plate can also be heated either before the process or constantly heated during processing. Both approaches enable the attenuation of residual stresses [43] and a higher relative density [71].

2.5 State of the Art: Numerical Models

Additive manufacturing is a powerful tool as long as the manufacturing and design community is educated about its problems [20]. In order to use additive manufacturing in aerospace components, it is strictly necessary to investigate the process parameters contribution into the component quality. Experimental investigation is, however, unsuitable due to high costs and try-out-times related to the vast number of variables. While post-thermal treatments are easily applied, these are costly. Thus, accurate numerical solutions to predict final part properties are of considerable importance.

A thorough search of the relevant literature, attempting to discovering the first PBF-related numerical model, yielded in the publication by Sun [72], whose work dates back to 1991. The

numerical model aimed at understanding SLS phenomena and predict the system behaviour both qualitatively and quantitatively. In the following years, numerical models of PBF were only limited to one or two dimensions. Literature reports only a few 3D models restricted by complexity of PBF until 2004, when the thermal numerical analysis of SLS developed by Kolossov et al. [73] was published. From this point on, a myriad of thermal and thermoelastic precise models on several additive manufacturing methods have been published until today, with a substantial focus on SLM.

For each AM method, there are alternative modelling options regarding the simulation purpose (and therefore, type of analysis and study scale), heat source, layer addition mechanism, material properties dependence, heat transfer mechanism, unconsidered phenomena and mesh distribution.

2.5.1 Modelling Purposes

Numerical analysis is a versatile tool that allows the replication of a realistic situation in a clean and affordable manner. Retaining only to the topic, the complexity of the physical phenomena present in SLM creates a wide range of simulation purposes. These include the analysis of temperature distribution [74], the evolution of thermal stresses [75], the most desirable post-processing treatments [76], post-processing performance [77], the most suitable processing parameters [78], topology optimisation [79], melt pool dimensions [75] and the evolution of metallurgical microstructure [80]. Some of these objectives are incompatible with each other when it comes to the dimensional scale of the analysis, which leads the discussion to the comprehension of the study scales.

Microscale approaches are responsible for the prediction of the metallurgical microstructure variations during the solidification process, while mesoscale approaches aim at analysing the thermo-fluid dynamics of individual powder grains while a heat source acts on a domain smaller than a powder layer or evaluating the powder flow during recoating [81]. Microscale models remain scarce due to high computational costs and complexity and experimental procedures are preferred [16]. Neither of these are the focus of this thesis, as spatial distributions of thermal and structural variables on the scale of the final workpiece are assessed by macroscale approaches.

Applicable software and methods may be used for each study; Finite Element Method (FEM)

is undoubtedly the most common method for macroscale approaches, and can be found in software such as ANSYS, SIMUFACT and COMSOL Multiphysics, to name a few.

Selective Laser Melting is a complex process that involves multiple physical phenomena whose simulation would take longer than what would be a feasible amount of time. Because some physical meso- and microscale aspects are neglected and other simplifications are undertaken, phase changes, adequate laser distribution, heat transfer mechanisms and layers activation must not be ignored.

2.5.2 Heat Source Modelling Strategies

Several heat source models have been developed and implemented according to the type of accuracy required. The simplest strategy is to use a **constant temperature input** instead of a proper heat source. A constant temperature can be applied as a constraint or as an initial condition to a newly activated layer. It is useful for the sake of simplicity [16]; however, it neglects some important parameters.

Another trivial model is the **constant heat source**. A general example of this category is the top-hat disk, in two dimensions, and the volumetric version is the cylindrical model. Uniform heat sources can be found in [82] and [83].

The trend points to Gaussian surface distribution as the most suitable to replicate laser beams. The symmetrical aspect of the **Gaussian heat source** accurately represents a laser beam. Nevertheless, a Gaussian-shaped laser beam has some flaws: the axial symmetry neglects absorptivity variations in the heated affected zone (HAZ), i.e., where the melt pool is formed, and energy penetration is underestimated. In fact, energy penetration is an issue that affects every surface beam distribution due to the negligence of the z-component when modelling the beam. In order to respond to such problems, **modified Gaussian heat sources** were introduced, namely truncated cone heat source, double surface and volumetric heat source, Gaussian ellipsoid heat source, semi-spherical Gaussian heat [16]. On the one hand, the increased complexity of these modified models requires the characterisation of a set of adjusting parameters. On the other hand, it provides a more correct assessment of the medium penetration and enhanced accuracy.

In a more sophisticated approach, Goldak and Akhlaghi [84] introduced two models based on welding simulations in order to overcome the low accuracy of symmetrical strategies when

it comes to the variation of laser absorption: **single Goldak heat source** and **double ellipsoidal Goldak heat source**. These models, especially the latter, have been highly implemented in AM simulations because of its versatility. However, it shares the issues of the modified Gaussian heat sources: a series of unknown parameters, e.g., optical penetration depth and powder fractions, lead to a dependency on experimental calibration and validation, limiting the applicability of the method [85].

Gusarov and Kruthet [86] established a refined heat source model that accounts for multiple reflections inside the powder bed. **Gusarov heat source** is, however, less common and involves powder particles properties not easily obtained [16].

Moreover, it is common to simulate the motion of the laser beam through a path. The moving point heat source model was originally developed by Carslaw and Jaeger [87] in 1959, but other analytical models have been developed, some of which can be compared in [88] [89].

2.5.3 Simplification Strategies

For computational purposes, simplifications have to be performed sometimes. Model assumptions such as two-dimensions, symmetry, single-layer processing, single heat transfer mechanism and constant material properties as well as the material's plastic regime and evaporation neglecting are some of the most common simplification methods.

In order to carry out a thermal analysis in reasonable computational times, Chiumenti et al. [74] replaced the powder bed domain by an equivalent boundary condition to simulate convective heat dissipation and used an approximated scanning pattern in a first trial. In a new trial, the powder bed was added to the analysis and sequentially, alternative scanning paths were investigated. The authors concluded that the model designed in the first trial was capable of accurately capturing the global thermal responses, reducing computational times and the uncertainties associated with the powder thermophysical properties and avoiding characterisation of the material powder. However, lower accuracy was reported when compared to a more representative model and it was suggested that this modelling strategy is to be avoided whenever precise results are required.

Each simplification procedure have advantages and disadvantages similarly to the given example, thus, requiring a careful evaluation before implementation.

2.5.4 Layer Addition Modelling Strategies

Single layer studies have been performed by some authors [90] in order to rapidly assess the impact of process parameters. Nevertheless, this simplification may not reveal the same patterns as those identified for an entire manufactured component. The addition of layers is, therefore, required towards obtaining reliable data.

The element birth and death method is undoubtedly the most popular to capture the addition of layers [62] [91] [92] by manipulating the properties of the inactive elements. Deactivation occurs when the properties are set to zero [93]; when activated, their original values are restored in a stress-free state, i.e., with no record of strain history. By avoiding the sudden generation of artificial stresses when the material is activated, the solidification of the feedstock is correctly emulated.

2.5.5 Phase Change Modelling Strategies

Modelling phase changes is a complex process that requires the contribution of latent heat effects. The most attractive and versatile approach is the formulation of phase fraction variables that can be obtained either by temperature-based [94] or enthalpy-based interpolation [95]. Material properties are temperature- and phase-dependent and are evaluated by the interpolation of the single phase parameters [81]. Latent heat effects can be modelled through the apparent capacity method [11] or the heat integration method [96].

Proell et al. [81] proposed a novel variant of the heat integration method that enables the user to control efficiency and accuracy by defining a tolerance parameter, depending on the model specifications. The authors revealed that the proposed heat integration has an efficiency similar to the apparent capacity method while being more accurate.

A different perspective on modelling phase changes is the one adopted in the work of Hodge et al. [97]. Their model accounts for a single phase change using the Stefan-Neumann equations. Instead of considering melting or solidification processes, the transformation occurs between the powder and the consolidated phase, which encompasses both solid and liquid material. This approach successfully simulates an irreversible phase change, but may neglect some important events.

Conti et al. [98] simulated the interference of the latent heat by simply assuming a sudden

rise of the specific heat at the melting temperature. However, the authors concluded that the latent heat must be properly assessed in order to accurately replicate the nature of the process.

2.5.6 Material Properties Dependence

Density. Despite varying with different factors, density is not equally affected by these. For instance, temperature-dependent density has a greater impact on the structural problem than on the thermal one. For this reason and aiming to reduce computational costs, a constant density value can be adopted for the thermal simulation. In addition to variations with temperature, density can be considered a phase-dependent property for the solid and liquid states and porosity-dependent for the powder bed.

Thermal conductivity. Considering that this property assists the cooling mechanisms of the process [98], it becomes clear that it is one of the most crucial parameters of the problem. An inaccurate formulation of the thermal conductivity is likely to affect the simulation results. However, the lack of reliable data has motivated some authors to consider a constant value for the thermal conductivity.

For each phase, similarly to density, thermal conductivity varies, which becomes evident especially for the powder phase. Powder beds have a low thermal conductivity, almost as low as that of the gas, when compared to the conductivity of bulk material. These variations reduce the sensitivity of the simulation, such that the thermal conductivity of loose powders can be considered constant and, as long as experimental data is not available, theoretical models are the most reliable manner to compute it, taking into account the porosity and the thermal conductivity of the gas phase. Models for the prediction of the thermal conductivities of powders can be found in [11] and [99].

Alternatively, Foroozmehr et al. [100] considered the thermal conductivity of the powder to be constant below the solidification temperature, representing 1 % of the thermal conductivity of the solid material.

Specific heat capacity. Several studies use pre-defined values from experimental data for the specific heat capacity that are assumed constant for the liquid, solid and powder phases. In fact, the relation between the specific heat of the powders and the bulk solid material can be given by the Kopp-Neumann law [101]. As long as the powder bed properties are studied

as homogeneous, the mass fraction of the filling gas, f_a, can be neglected:

$$C_{p_s} = C_{p_p} f_p + C_{p_a} f_a = C_{p_p}(1 - f_a) + C_{p_a} f_a \approx C_{p_p} \ , \quad (2.2)$$

where the indices s, p and a denote the solid phase, the powder phase and the gas, respectively. Therefore, the specific heat of the powders can be assumed equal to that of the solid material.

Emissivity and heat transfer coefficient. Emissivity translates the efficiency of the body as a radiation emitter [74]. This parameter is only required when the radiation mechanism is assumed in the model and is usually adopted from experimental measurements. Regarding emissivity of the powder bed, it is greater than the emissivity of the solid phase and can be assessed through analytical and experimental porosity-dependent models, namely the ones addressed in [85] and [102].

Convection is frequently considered negligible on thermal simulations of SLM in the interest of reducing computational costs. On the other hand, a detailed analysis benefits from convective contributions. Bertini et al. [16] reports that convection was implemented in more than a half of the papers reviewed. The convective mechanism presupposes the calculation of the heat transfer coefficient, which is difficult to evaluate. Thus, several authors adopt different coefficients for the same material, which may be caused by different problem assumptions [85].

Both of these parameters are considered the most difficult to accurately evaluate. However, they are also reported to be the least significant, mainly when compared to conduction contributions.

2.5.7 Mesh Distribution

Long computation times justify opting for simplifications, as the ones above-mentioned; additionally, many authors have opted for low resolution meshes, coarser than the heat source radius, which particularly reduces accuracy. On the other hand, in order to refine the mesh distribution, some models only compute a small part of the geometry, e.g., single-layer approach, once again affecting the final results. Thus, in order to ensure accuracy and efficacy, two mesh techniques are suggested: refining the mesh where the analysis is critical and progressively coarsening as the distance increases [78] or implementing a moving dynamic mesh

refined on the HAZ that moves along with the laser beam through the scanning pattern [103].

This project covers the development of a thermoelastic model of Selective Laser Melting, by means of the coupling between COMSOL Multiphysics and MATLAB, capable of evaluating residual stresses for a complete sample according to a list of process parameters. As reviewed in this chapter, there are still some gaps in the literature regarding the effects of process parameters. Each part has a specific set of parameters that may optimise final part properties. Therefore, literature review has helped to identify some general patterns, but each sample requires a type of validation.

Chapter 3

Problem Formulation

Several assumptions have been made with the intent of formulating the problem at hand, some of which are:

- evaporation heat losses are neglected;
- melt pool physics such as the Marangoni effect is not included in the model;
- microstructure transformations are not taken into account;
- only single-layer processing is addressed in the problem formulation; the concept of layer addition is introduced in Chapter 4 along with the necessary modifications.

This chapter defines the governing equations and conditions used to perform a complete numerical analysis of the manufacturing of a Ti-6Al-4V specimen. Both fields in study, thermal and structural field, are assessed by means of a transient 2D-axisymmetric modelling approach.

3.1 Heat Transfer Model

The thermal problem to be solved involves a laser beam that moves at constant velocity on the powder bed progressively melting the metal powder particles. As long as the laser scanning completes one layer, a period of cooling begins allowing for the material to consolidate. The thermal physics described in the model can be divided in two related phenomena: the balance of thermal energy and phase changes.

The balance of energy equation can be stated as

$$\rho C_p \frac{\partial T}{\partial t} = -\nabla \mathbf{q} + Q \,, \quad (3.1)$$

where ρ is the density of the material, C_p is the specific heat capacity, T is the temperature, t is the time, Q is the heat source and $\mathbf{q}$ is the heat flux vector in a continuous medium calculated according to Fourier's law of heat conduction

$$\mathbf{q} = k\nabla T \ , \quad (3.2)$$

The coefficient of proportionality between the conductive heat flux and the temperature gradient is the thermal conductivity of the material, k.

3.1.1 Initial and Boundary Conditions

According to the nature of the problem, an appropriate set of boundary conditions must be added to the heat transfer equation.

Some authors [62] consider convection and radiation losses negligible when modelling SLM. This can be explained by the inherently high thermal conductivity of metals, which makes conduction a predominant mechanism. Comparatively, the contribution of convection and radiation to thermal losses is often considered minimal. In addition, the inert atmosphere inside the build chamber diminishes convection [14]. However, different authors recognise that either both thermal mechanisms [96] [104] or one of them - radiation [94] [97] and convection [11] [103] - have an important impact in the process. Because of the controversy regarding this issue, conduction, convection and radiation are included in the model.

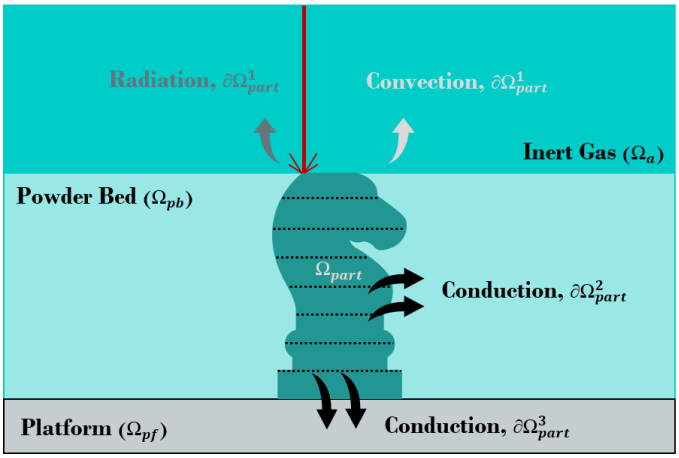

Figure 3.1: Heat transfer phenomena considered in the problem (for illustration purpose only).

Figure 3.1 shows a schematic illustration of the phenomena considered in the final model,

where Ω_a, Ω_{pb}, Ω_{pf} and Ω_{part} represent the domain of the gas, the powder bed, the platform and the part (during processing), respectively. $\partial\Omega^1$, $\partial\Omega^2$ and $\partial\Omega^3$ correspond to the upper, lateral and lower boundaries of the correspondent domain.

Moreover, initial conditions must be defined in terms of the temperature field at $t = 0$:

$$\text{Temperature of the gas: } T(t=0) = T_a \quad \text{in} \quad \Omega_a \tag{3.3}$$

$$\text{Temperature of the platform: } T(t=0) = T_{pf} \quad \text{in} \quad \Omega_{pf} \tag{3.4}$$

$$\text{Temperature of the powder bed: } T(t=0) = T_{pb} \quad \text{in} \quad \Omega_{pb} \tag{3.5}$$

3.1.1.1 Heat transfer by conduction

Theoretically, heat conduction, also known as diffusion, occurs as a consequence of different mechanisms in different media. In metals, for example, heat conduction takes place by electrons carrying heat and, in a gas, through collisions of molecules [105]. On the specific problem, heat is transferred by conduction to the base plate and to the powder bed, as described in Figure 3.1. The base plate is typically made of steel, so its high thermal conductivity favours heat exchange with the part.

As mentioned in Subsection 2.5.3, the integration of the powder bed as a computational domain to replicate heat losses can be replaced by an equivalent boundary condition

$$q_{cond} = h_{cond}(T - T_{pb}) \quad \text{on} \quad \partial\Omega^2_{part}\,, \tag{3.6}$$

where h_{cond} denotes the heat transfer coefficient. While this strategy reduces computational time and simplifies the physics of the problem, it would have a negative influence in the predictions. Alternatively, when the powder bed is included, the physical properties are prescribed in terms of porosity, ϕ[1].

Some authors [21] defend, however, that the overall conductivity contributions from particle-to-particle contact points in loose powder are negligible, as heat transfer in the powder bed pores is typically governed by the inert gas (in the convective form). Thus, the thermal conductivity of the powder is substantially smaller than the conductivity of the compacted solid phase.

[1] porosity-dependent properties are discussed in Chapter 4.

3.1.1.2 Heat transfer by convection

Convection is caused by the transportation of heat content by the net displacement of a fluid at a certain velocity [105]. Consequently, the velocity vector, $\mathbf{u}_a$, must be added to the balance of energy equation

$$\rho C_p \left(\frac{\partial T}{\partial t} + \mathbf{u}_a \nabla T \right) = -\nabla \mathbf{q} + Q \,. \quad (3.7)$$

Additionally, convection refers to the heat dissipation from a solid surface to a fluid - in this case, from the part being processed to the surrounding atmosphere -, typically described by the Newton's law

$$q_{conv} = h_{conv}(T - T_a) \quad \text{on} \quad \partial\Omega^1_{part} \,, \quad (3.8)$$

where h_{conv} is the convective heat transfer coefficient.

3.1.1.3 Heat transfer by radiation

In theoretical means, heat transfer by radiation takes place through the transport of photons [105]. In SLM, radiation flows from the heat source to the powder bed and from the part to the environment. The laser beam is modelled by a Gaussian with a symmetrical shape of laser irradiance across the beam where the maximum irradiance, I_0, is at the centre of the beam pattern. Q at any point for the fundamental mode (TEM_{00}) is given by

$$Q = I_0 \, e^{\left(\frac{-2R^2}{R_g^2} \right)} \,, \quad (3.9)$$

where R_g is the radius of the laser beam at which the heat flux is reduced by a factor of $1/e^2$ with respect to the heat flux at the centre of the beam - also referred as standard deviation. R is the distance of a point, r, from the laser focal point, r_f. I_0 is characterised by the laser power, P, and by R_g according to

$$Q = \frac{2\eta P}{\pi R_g^2} \, e^{\left[\frac{-2(r-r_f)^2}{R_g^2} \right]} \quad \text{on} \quad \partial\Omega^1_{part} \,. \quad (3.10)$$

When a laser acts upon a layer, powder particles may absorb or reflect it due to the presence

of voids [63]. Therefore, a laser energy absorption coefficient of the material, η, is often introduced to the laser equation. This coefficient depends on a number of factors, namely the wavelength of the laser beam [62], the porosity of the powder [103] and the level of oxidation [91]. Throughout the simulations, due to the sophistication of the parameter, η is assumed to be one, except when performing experimental validation, where an empirical value is given, and parametric studies. Models to estimate the absorption coefficient are presented in [85].

Finally, the radiation heat flux can be calculated by using the Stefan-Boltzmann law

$$q_{rad}(T) = \sigma_{sb}\varepsilon(T^4 - T_a^4) \quad \text{on} \quad \partial\Omega^1_{part} \,, \quad (3.11)$$

where ε is the emissivity of the radiating surface and σ_{sb} is the Stefan-Boltzmann constant, equal to 5.67×10^{-8} W m^{-2} K^{-4}.

3.1.1.4 Heat transfer to the exterior

Exterior boundaries in SLM are not thermally insulated. This means that heat flows to the exterior of the build chamber. For that reason, a boundary condition is applied to the external edges in order to simulate heat losses to the exterior

$$T = T_{amb} = 293 \text{ K} \quad \text{on} \quad \partial\Omega^{1,2}_{bc} \,, \quad (3.12)$$

where $\partial\Omega^{1,2}_{bc}$ represents the upper and lateral boundaries of the build chamber.

3.2 Structural Mechanics Model

The quasi-static mechanical analysis is performed in order to obtain the mechanical response derived from the thermal history. The governing stress equilibrium equation is

$$\nabla\sigma_{ij} + F_{ij} = 0 \,, \quad (3.13)$$

where σ is the stress and F are the body forces neglected in the problem.

The linear elastic constitutive law defines the stress-strain relationship [106], governed by

isotropic Hooke's law as [65] [107]

$$\sigma_{ij} = C_{ijkl}\epsilon^{\text{el}}_{kl} \ , \quad (3.14)$$

where C is the fourth order elastic stiffness tensor calculated from Young's modulus E and Poisson's ratio ν [82] as

$$C_{ijkl} = \frac{E}{1+\nu}\left[\frac{1}{2}(\delta_{ik}\delta_{jl} + \delta_{ij}\delta_{kl}) + \frac{\nu}{1-2\nu}\delta_{ij}\delta_{kl}\right] \ . \quad (3.15)$$

The Kronecker delta function, δ_{ij}, is zero if $i \neq j$ and one if $i = j$.

The total strain is given by

$$\epsilon_{ij} = \epsilon^{\text{mec}}_{ij} + \epsilon^{\text{th}}_{ij} = \epsilon^{\text{el}}_{ij} + \epsilon^{\text{pl}}_{ij} + \epsilon^{\text{th}}_{ij} \ , \quad (3.16)$$

where ϵ^{mec} and ϵ^{th} are the strains associated to the mechanical and thermal loads and ϵ^{el} and ϵ^{pl} represent the elastic and plastic strains, respectively. The strain-displacement relation, being the displacement represented by $\mathbf{w}$, is given by

$$\epsilon_{ij} = \frac{1}{2}\left[\nabla\mathbf{w} + (\nabla\mathbf{w})^{\text{T}}\right] \ . \quad (3.17)$$

3.2.1 Initial and Boundary Conditions

In the structural module, initial conditions are defined in terms of the displacement as:

$$\text{Displacement field of the layer: } \mathbf{w} = 0 \quad \text{in} \quad \Omega_{part} \quad (3.18)$$

$$\text{Displacement field of the platform: } \mathbf{w} = 0 \quad \text{in} \quad \Omega_{pf} \quad (3.19)$$

The substrate bottom of the part being processed is fixed to the base plate during processing; this constraint can be modelled by adding a displacement restriction:

$$\mathbf{w} = 0 \quad \text{on} \quad \partial\Omega^{3}_{part} \ . \quad (3.20)$$

Most materials react to temperature gradients by a change of volume. Thermal expansion or contraction can occur without the generation of stresses as long as materials are uncon-

strained. However, if a material is fixed to a rigid body at multiple locations [105], thermal stresses are likely to evolve on that region.

3.3 Thermoelastic Coupling: Thermal Expansion

For isotropic materials, thermal history is used to assess the displacements and stresses of the solidified part. The volume change can be represented by the thermal strain, ϵ^{th} (secant formulation):

$$\epsilon_{ij}^{\text{th}} = \alpha_T (T - T_{ref}) \delta_{ij} \,, \quad (3.21)$$

where T_{ref} is the strain reference temperature at which the thermal strain is zero; usually, T_{ref} is set at the solidification temperature for the material being processed [16]. In this case, both the part and the platform are evaluated in terms of the thermal expansion. When T is greater than T_{ref}, the constraints exert a compressive force on the material. The opposite happens while cooling: when T is less than T_{ref}, the stresses are tensile. α_T is the linear coefficient of thermal expansion.

Throughout the development of the model it may be necessary to modify some terms in the governing equations; these are further documented in Chapters 4 and 5.

Chapter 4

Modelling of the Cylindrical Specimen

In order to achieve a model capable of analysing the thermoelastic properties obtained during the manufacturing process of a part, the following strategy is adopted: it consists in developing an accurate model by incrementally adding complexity. The advantage of this approach is its computational viability: firstly, adding complexity step-by-step helps to easily identify the causes of some errors and the contribution from each parameter or phenomenon and, secondly, it reduces computational costs and time, which is helpful for try-out approaches.

The first model replicates the printing of a cylindrical specimen with a radius of 1 cm and a height of 10 cm inside a cylindrical build chamber. The simplicity of these shapes allows for a 2D-axisymmetric representation of the setup, as shown in Figure 4.1. Geometrically, assuming that the revolving axis is at the centre of the cylinder, the build chamber is represented by a rectangle with dimensions 40 cm $\times$ 80 cm.

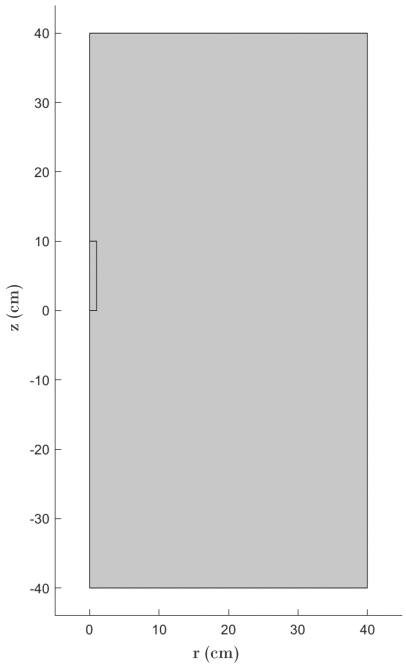

Figure 4.1: 2D-axisymmetric representation of the setup.

Because of a lack of experimental data for validation purposes, this model serves mainly as a

learning tool towards achieving a more robust model. Initially, the simulation is performed only for the first added layer. While single-layer modelling is performed in COMSOL Multiphysics, LiveLink for MATLAB, the interface between MATLAB and the FEM software, is used to perform the layer addition.

4.1 Single-layer Modelling

Model revision I. *Thermal modelling of a solid single layer in steady state.*

The preliminary simulation encompasses the simple laser heating of a single-layer placed at the centre of the chamber in a steady state study. Assuming a layer thickness of 0.25 cm, the first one is represented by a rectangle with dimensions 0.25 cm $\times$ 1 cm. The origin of the reference frame from which the geometries are defined is the point where the revolution axis meets the lower boundary of the layer.

As shown in Figure 4.1, the powder bed and the base plate are provisionally neglected; therefore, the only initial condition is the temperature of the system where the layer and the gas are assumed to be at the same temperature. Because of the high reactivity of Ti-6Al-4V with oxygen, the chamber is filled with argon. While the properties of the gas are adopted from the COMSOL Library, titanium properties are not temperature- or phase-dependent, and instead, average values are used for ρ, k and C_p.

As described in Chapter 3, the final model allows heat transfer by the three principal mechanisms. Convection is partially responsible for heat dissipation from the part to the inert atmosphere. Numerically, with the absence of the powder bed, this could be simulated by adding an internal heat flux to the boundaries of the component. However, COMSOL limits the addition of convective heat fluxes to internal boundaries, because convective losses are computed automatically by the interaction of a solid surface and a fluid with non-null velocity. Conductive heat fluxes in solid domains are computed automatically as well. In order to ensure that conduction is the only heat transfer mechanism affecting the initial conditions, argon is assumed to be motionless, i.e., $\mathbf{u}_a = 0$.

Aiming to replicate the action of a laser beam, a heat source is applied as a boundary condition in the top surface of the layer; it is assumed to be steady and centred with the revolution axis to ensure axial symmetry. The laser is modelled with an uniform profile, i.e., top-hat disk

distribution.

$$Q = \frac{P}{A}, \quad (4.1)$$

where A represents the area of the surface where the laser beam is deposited upon, assuming the 3-dimensional form of the layer, i.e, after the revolving. COMSOL has a built-in *Deposited Beam Power* node in the *Heat Transfer* module that includes the top-hat disk profile, where only the laser characteristics have to be defined.

The modelling approach adopted aims at the behavioural analysis of the application of particular boundary conditions. Hence, thermal insulation is prescribed to the external boundaries of the built chamber such that the physics behind the model are more easily perceptible

$$\mathbf{q}_{ext} = 0 \quad \text{on} \quad \partial\Omega_{bc}^{1,2,3} . \quad (4.2)$$

Model revision II. *Thermal modelling of a single layer in steady state with one phase change.*

Phase changes play a fundamental role in Selective Laser Melting. Each transformation affects the quality of the finalised component: melting contributes to the agglutination process and solidification is responsible for the generation of stresses and distortions. Although the introduction of the phase changes adds significant complexity to the model, it would be incomprehensible to move forward without it.

Phase Change Material is a subnode in COMSOL used to solve the heat equation according to the apparent heat capacity formulation [105]. Figure 4.2 illustrates a single phase transformation defined by the phase change temperature, T_{pc}.

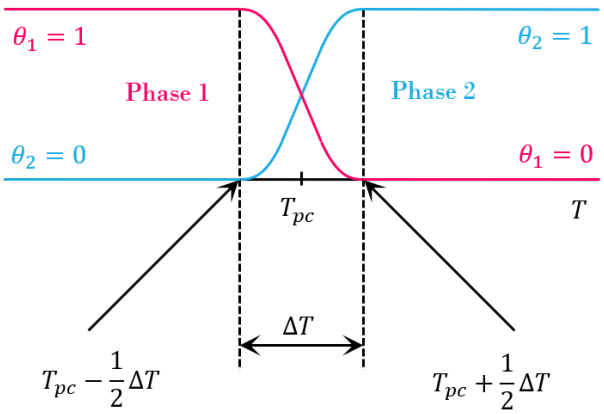

Figure 4.2: Diagram of a single phase change.

For computational modelling purposes, instead of considering an immediate transformation when T_{pc} is reached, a small transition zone over a finite temperature range, ΔT, is introduced to represent the interval where the phase change occurs. Before $T_{pc} - \frac{1}{2}\Delta T$ and after $T_{pc} + \frac{1}{2}\Delta T$, the material is completely in phase one and phase two, respectively, defined by phase indicators, θ_1 and θ_2, which must satisfy

$$\theta_1 + \theta_2 = 1 \ . \quad (4.3)$$

The enthalpy, H, is a phase-dependent property given by Equation 4.4 that can be transformed in order to obtain the specific heat capacity. After differentiating with respect to temperature and proceeding some formal transformations, the formula for the specific heat capacity is given by Equation 4.5.

$$H = \theta_1 H_1 + \theta_2 H_2 \ , \quad (4.4)$$

$$C_p = \frac{\partial H}{\partial T} = \theta_1 C_{p_1} + \theta_2 C_{p_2} + (H_2 - H_1)\frac{d\alpha_m}{dT} \ , \quad (4.5)$$

and finally, the apparent heat capacity becomes

$$C_p = \theta_1 \, C_{p_1} + \theta_2 \, C_{p_2} + L\frac{d\alpha_m}{dT} \ , \quad (4.6)$$

where L is the latent heat absorbed (melting) or released (solidification) and α_m represents the mass fraction

$$\alpha_m = \frac{\theta_2 - \theta_1}{2} \ . \quad (4.7)$$

Although the subnode allows for up to five phase changes, when two or more are considered, the temperature at which each transition occurs must be increasing through the changes, i.e., $T_{pc_{j\to j+1}} < T_{pc_{j+1\to j+2}} < \ldots$. In the problem at hand, melting happens before solidification and the melting temperature is higher than the solidification temperature, so the condition is not satisfied: $T_{pc_{1\to 2}} > T_{pc_{2\to 3}}$. Consequently, at this stage only one phase change - from solid to liquid - is considered through the subnode.

Qualitative analysis shows that the liquid phase indicator, θ_l, is zero (and $\theta_s = 1$) until reaching $T_m - \frac{1}{2}\Delta T$ where it starts to gradually increase. After reaching $T_m + \frac{1}{2}\Delta T$ - and if temperature is kept over or equal to that temperature - the phase indicator is set to one (and $\theta_s = 0$).

Inevitably, a distinction between solid and liquid properties needs to be made at this point. Thermal conductivity and specific heat capacity assume different values for each phase, while a single density is defined for both of them in order to ensure mass conservation on the material frame as imposed by the *Phase Change Material* subnode.

Model revision III. *Thermal modelling of a single layer in a time-dependent study with two phase changes.*

The replication of the printing process requires a new modelling strategy capable of simulating two phase changes with no sequence constraints. In reality, phase changes in SLM occur in cycles where powder and solidified material can always be melted, and melted material can always be solidified, but the change from powder to molten material is irreversible. At this point, however, only two phases are considered, as powder is replaced by solid material, which allows for a simplification in material properties, as shown in Figure 4.3:

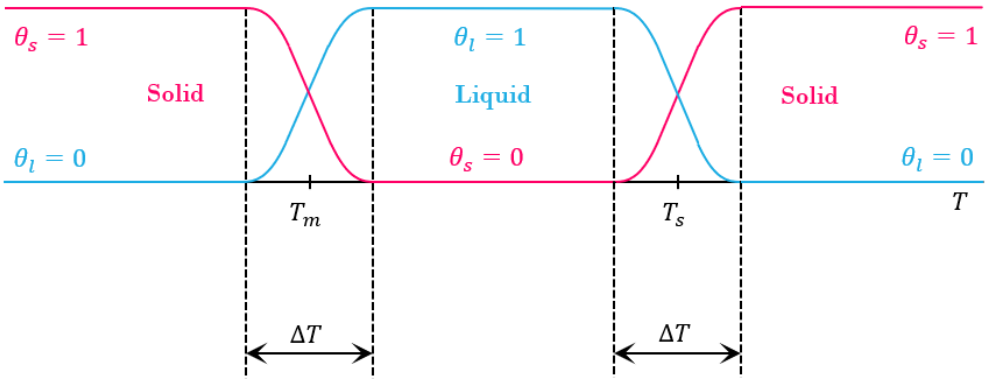

Figure 4.3: Diagram of two phase changes.

A similar procedure to the one described above is used to model a two-phase change material with thermal hysteresis. A material with thermal hysteresis such as titanium exhibits a melting temperature that is different from the solidification temperature. The implementation of these phenomena with subsequent heating and cooling stages implies updating the study to evaluate transient effects.

While the heating process, as explained above, is modelled with an uniform distribution, the cooling process has not been established. The most streamlined and flexible method to replicate the heating and cooling time-frames is the implementation of a time-dependent rectangle function that enables the activation and deactivation of the laser beam. According to the representation of the rectangle function in Figure 4.4, the laser beam is turned off at

zero and reaches its maximum power at one.

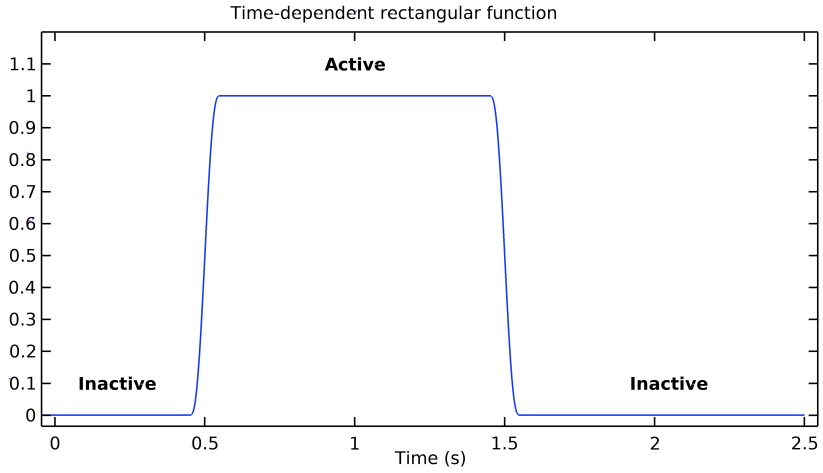

Figure 4.4: Rectangular temporal distribution for the laser action.

A triangular temporal distribution is investigated as well. The activation and deactivation follow an identical principle to that of the rectangle function. The essential difference between both functions is that while the triangular profile increases, reaches the maximum power and declines, the rectangular increases until reaching the maximum power where it is maintained, adding further energy to the boundary. Due to the similarities and adequacy of both profiles, the rectangular function is selected simply because it is more intuitive.

After establishing the thermal cycles, phase transformations can be formulated by means of the material enthalpy. Figure 4.5 represents the temperature-dependent enthalpy of Ti-6Al-4V.

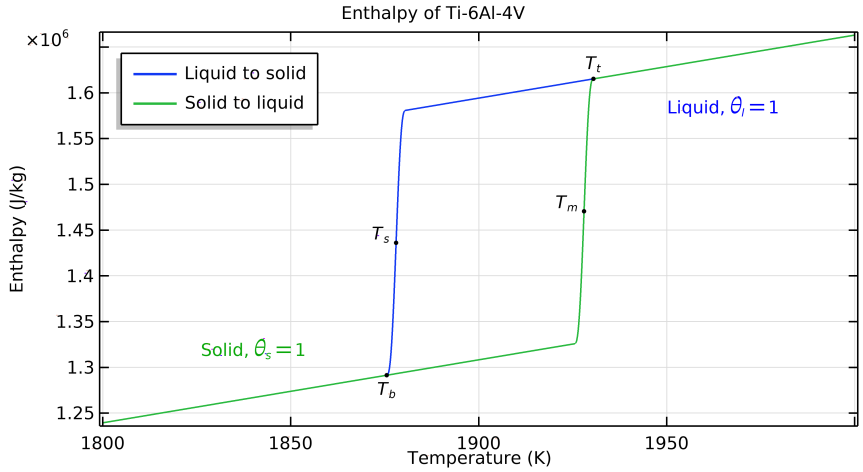

Figure 4.5: Temperature-dependent enthalpy for Ti-6Al-4V.

The smoothed enthalpy functions plotted in Figure 4.5 are given by

$$H_{s\to l} = C_{p_0} T + \frac{L_m}{1+e^{-\Delta T(T-T_m)}}\ , \quad (4.8)$$

$$H_{l\to s} = C_{p_0} T + \frac{L_s}{1+e^{-\Delta T(T-T_s)}}\ , \quad (4.9)$$

where C_{p_0} is the average specific heat capacity representing the functions slope. The latent heat absorbed or released within the temperature interval is represented by the jump in both curves. The indices s and l denote *solid* and *liquid*, respectively.

Each curve represents the path followed during computation. Accordingly, the green and blue curves describe the heating, $H_{s\to l}$, and cooling, $H_{l\to s}$, processes, respectively. When temperature is rising due to laser action and the melting temperature is reached, $T_m = 1928$ K, a phase change from solid to liquid occurs. During the cooling process, when the solidification temperature is reached, $T_s = 1878$ K, there is a new phase change from liquid to solid.

Similarly to the approach adopted by the subnode, a temperature range in which a phase change occurs gradually, and therefore, where a mushy region is observed, ΔT, is implemented. Notwithstanding the computational interest of this approach, ΔT is introduced for a different reason: according to literature, alloys, due to its combination of metallic elements, have a phase change range [16] rather than a phase change point where its elements redistribute between solid and liquid phases. The range in which the transition occurs for Ti-6Al-4V is reported to be less than 10 K [36]. On that account, ΔT assumes a value of 5 in the model.

The points where $T_t = T_m + \Delta T/2$ and $T_b = T_s - \Delta T/2$ are used as reference points to (i) define the phase indicator value and (ii) switch paths - as the blue and green curves overlap when $T < T_b$ and $T > T_t$.

The two phase indicators in Figure 4.3, θ_s and θ_l, can be replaced by one phase indicator, θ_{sl}, such that

$$\theta_s + \theta_l = 1 \Leftrightarrow \begin{cases} \theta_s = \theta_{sl} \\ \\ \theta_l = 1 - \theta_{sl} \end{cases}\ , \quad (4.10)$$

meaning that $\theta_{sl} = 0$ represents the liquid state and $\theta_{sl} = 1$ the solid state. Similarly to the variables in the *Phase Change Material* node, θ_{sl} varies between zero and one, and can assume different values for each element [108].

The phase indicator variable is defined in the *Domain ODEs and DAEs*[1] interface and respects the following logic: if the current temperature is greater that T_t, titanium is completely liquid (θ_{sl} is zero); if the current temperature is less that T_b, titanium is completely solid (θ_{sl} is one); otherwise, when the current temperature is greater than T_b and less than T_t, θ_{sl} is left at its previous value and there is no change of path. The variable evaluation at the previous time step is guaranteed by the *Previous Solution* operator in the solver settings of the time-dependent study.

The phase indicator variable is used to define the specific heat of the material and its initial value, $\theta_{sl_{init}}$, must be properly defined. As a temperature-dependent variable, if the initial temperature of the system is below the lower phase-change temperature, titanium is in the solid phase and the variable is set to one.

As a result of thermal cycling in SLM, phase changes may cyclically occur to already processed material. Hence, the manufacturing process modelled is not constrained to a number of repeated phase changes.

Solid and liquid properties have already been distinguished for the subnode. At this point, these properties are being adapted to the model. While density remains unchanged, thermal conductivity and specific heat are given by

$$k = \theta_{sl} k_s + (1 - \theta_{sl}) k_l \ , \tag{4.11}$$

$$C_p = \theta_{sl} \frac{dH_{s\to l}(T)}{dT} + (1 - \theta_{sl}) \frac{dH_{l\to s}(T)}{dT} \ . \tag{4.12}$$

The equations take into consideration that θ_{sl} can assume values of zero, one or any number in between, meaning that not only can it assume two different values for the same property of the material, but several depending on the phase variable.

The specific heat capacity is represented in Figure 4.6. In the non-linear function of temperature, the steep gradients observed around the melting and solidification ranges are a consequence of the effects of the latent heat [21].

[1] the acronyms ODE and DAE stand for ordinary differential equation and differential-algebraic equation, respectively.

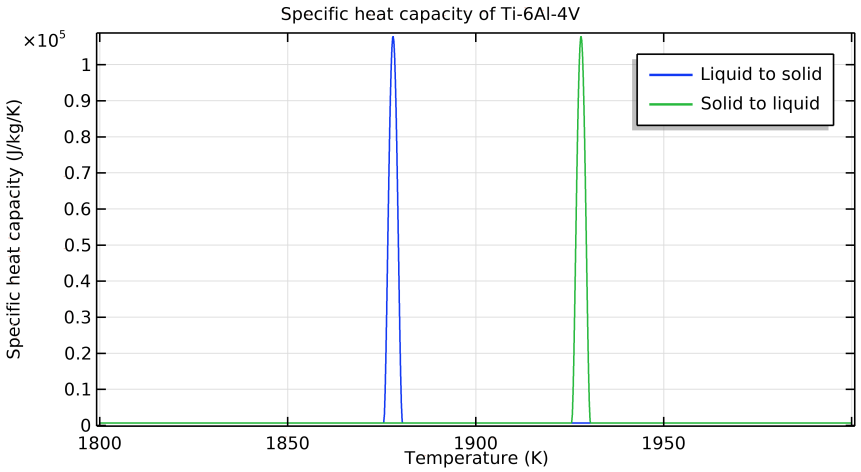

Figure 4.6: Specific heat capacity as a function of temperature.

During the development of the model, thermophysical properties are not considered as relevant as the performance of the simulations. For that reason, a deep research on phase- (and temperature-) dependent properties is not carried out until the model is completed. Instead, approximate, i.e., in the same order of magnitude, and realistic values are assumed. Table 4.1 includes the properties of titanium adopted hitherto. It is worth noting that the powder phase is not yet included. The full list of Ti-6Al-4V properties and respective references can be found in Appendix A, Table A.1.

Property	Solid	Liquid	Unit
ρ	4430	4430	kg m^{-3}
k	6	33.4	W m^{-1} K^{-1}
C_{p_0}	688.5	688.5	J kg^{-1} K^{-1}
L	286	286	J g^{-1}

Table 4.1: Material properties of Ti-6Al-4V in *Model revision III*.

The lack of predictions for C_{p_0} has resulted in a more methodical investigation: according to Fan and Liou [109], the specific heat of the alloy in study varies from 546 J kg^{-1} K^{-1} at room temperature to 831 J kg^{-1} K^{-1} at liquidus temperature; thus, an average value is computed, compared to the experiments of Boivineau et al. [110] and, as it fits in the same range of the estimated values, 688.5 J kg^{-1} K^{-1} is adopted.

Model revision IV. *Thermal modelling of a single layer in a time-dependent study with two phase changes and heat loss mechanisms.*

Structural calculations can only be executed when the material is in the compacted solid

phase, i.e., when the mechanical properties are activated. Thus, two requirements must be satisfied: not only the heat input must be sufficient to melt the entire layer, but also the cooling must be optimised such that it solidifies.

The most streamlined - but often undesired - technique to mechanically distinguish liquid and solid phases is reducing the liquid material elastic properties to a point where they are negligible. However, the posterior activation by simply restoring properties to its nominal level could suddenly produce stresses as long as there are any strains present in the material [111]. Additionally, quiet properties require a higher computational effort because a complex system of equations has to be solved for each time step [21]. A more convenient approach consists in activating the material in a zero stress state through the *Activation* functionality of COMSOL Multiphysics, which makes use of an activation expression that, if logically true, activates the material domain.

The purpose of *Model revision IV* is to ensure that the solidification phase change occurs in the full domain. Admitting a simulation time of 5 seconds, where a 100 W laser is activated at $t = 0.5$ s on a 50 μm layer and deactivated at $t = 1$ s, this is not verified: the entire layer is not completely melted, thereby preserving the material at its initial state. Thus far, the structural model has not been impaired by this deficit because the initial state is solid. In any case, complete phase changes must be guaranteed for when the powder is defined as the initial state. Assuming that the laser power is increased to 300 W, an issue would prevail: while the layer would have been entirely melted, the dissipation rate would not be sufficient for the solidification process to occur. A second option would be enlarging the laser activation period; however, the cooling time-frame would be reduced if the simulation time was kept at 5 seconds. Analysing the drawback of both options, i.e., the inadequacy of the dissipation process, one can conclude that the answer lies in the enhancement of the cooling performance.

Convection aids heat dissipation from the part to the argon-filled chamber in the real manufacturing process. Accordingly, this mechanism can be included by simply assigning a non-null value to the velocity vector of the gas, i.e., $\mathbf{u}_a > 0$. The value, albeit different from zero, must be kept at low orders of magnitude in order to replicate the real chamber conditions: the recirculating gas must not be capable of redistributing or removing particles from the powder bed. Figure 4.7 evaluates the contribution of convection to the solidification process on the centre point of the layer, point A, defined by $r = 0$ and $z = 25\ \mu m$.

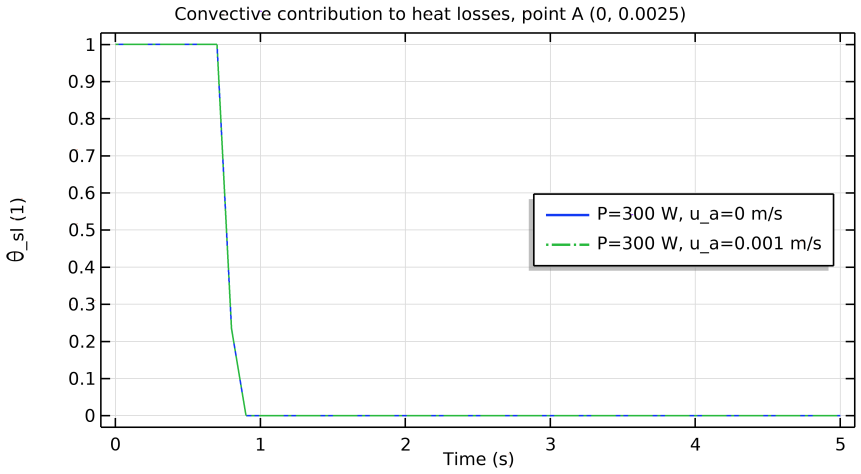

Figure 4.7: The influence of convection in phase changes.

Notably, a laser power of 300 W melts the entire layer, but the convective mechanism does not improve the dissipation to a point where a second phase change occurs. In fact, the convective contribution is barely noticed.

Along with convection, surface-to-ambient radiative fluxes are regarded to promote the dissipation rate. Giving the Stefan-Boltzmann law, Equation 3.11, heat losses through radiation depend on the energy radiated by the surface. The emissivity of Ti-6Al-4V varies in the literature: while some authors adopt the value of an almost perfect blackbody [96], others prefer to use a more realistic value [75]. In their experiments, Hagqvist et al. [112] found that the emissivity of Ti-6Al-4V varies between 0.3 and 0.4; for a preliminary simulation, an average value of 0.35 is used. The graph plotted in Figure 4.8 evaluates the importance of radiation during cooling in the same conditions of the convective study.

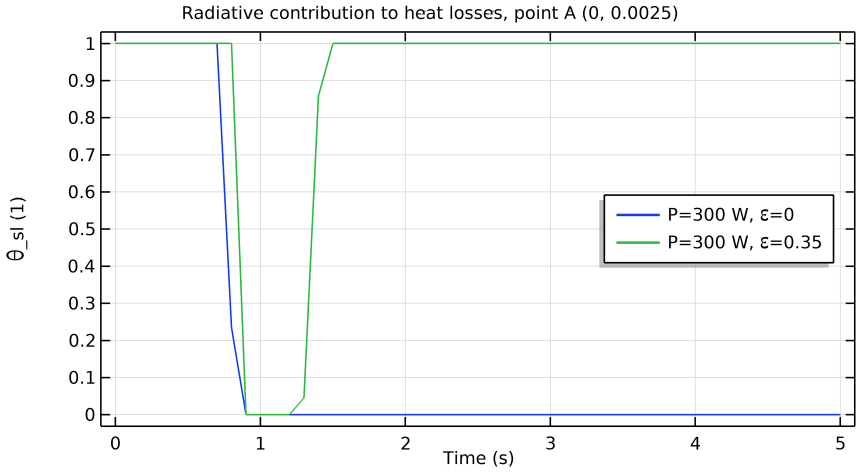

Figure 4.8: The influence of radiation in phase changes.

Effectively, radiative heat losses assist energy dissipation and, therefore, the solidification process, in contrast to the convective heat losses. Therefore, only the contribution of radiation to the heat dissipation process is implemented in the model.

Model revision V. *Thermoelastic modelling of a single layer in a time-dependent study with two phase changes, heat loss mechanisms and a refined laser distribution.*

The modifications described in *Model revision IV* effectively resulted in an operating model. Nevertheless, it is a volatile approach to undercover a problem that, depending on the characteristics of the model, e.g., material, conductivity and emissivity, may reemerge. Besides, it should be noted that a high laser power has consequences on the final part properties, some of which are not assessed by the model but must not be forgotten, namely chemical degradation and porosity. Therefore, a new approach must be adopted in order to eradicate the problem.

The heating mechanism determines the effectiveness of the melting and, albeit less prominently, the cooling stage. In SLM, the layer is not melted by a single scan with a large beam focus; instead, a moving laser with a small beam focus is applied on the surface where it follows a path that covers the entire area, causing uneven heating and cooling.

The refinement of the laser properties can be accompanied by the selection of the most appropriate laser distribution. From the heat source modelling strategies reviewed in Chapter 2, Subsection 2.5.2, constant temperature input, Goldak ellipsoidal models and Gusarov heat source are immediately discarded: while a constant temperature input would have the opposite effect to that intended, the other two would be too complex as experimental calibration and validation would be required. The remaining options are the uniform input that has been used, top-hat disk, and the bell-shaped Gaussian distribution. The decision is supported on a theoretical framework: while the uniform profile offers low computational costs, the Gaussian distribution combines accuracy with simplicity. The major weakness of the Gaussian shape is the negligence of energy penetration, which is common to the top-hat disk distribution. Hence, a simple Gaussian beam is preferred over a constant input. Schematically, both heat source shapes are characterised in Figure 4.9.

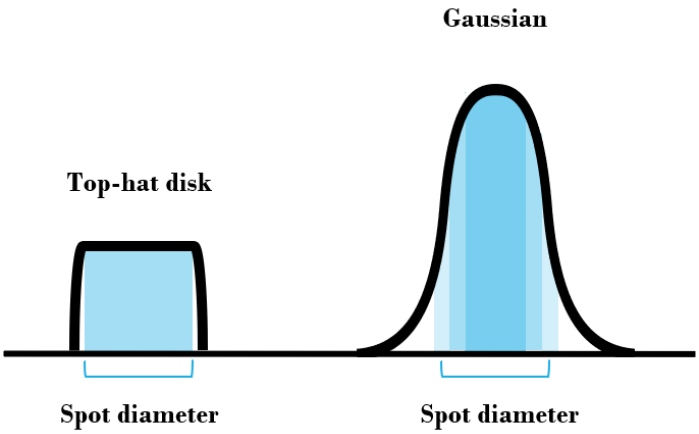

Figure 4.9: Comparison of laser shapes.

One of the few possible scanning strategies in a 2D-axisymmetric geometry is the path from the centre of the layer to the border, i.e., from r_0 to r_b, as illustrated in Figure 4.10a, which would resemble an approximated spiral shape on the top surface after revolution, as shown in Figure 4.10b. If an accurate 3D spiral path were to be implemented in a 2D perspective, interruptions of the radial displacement would have to be included.

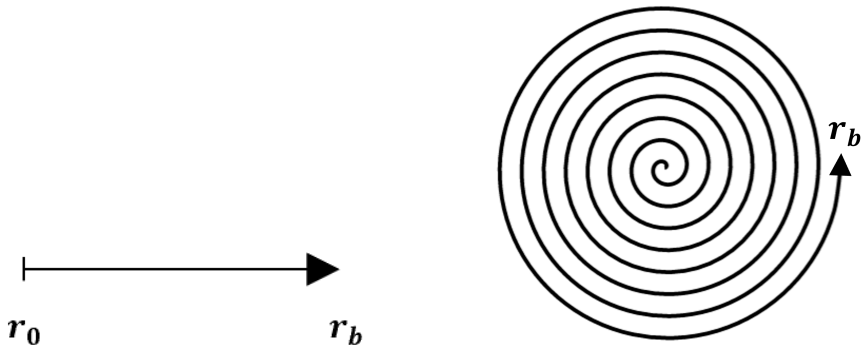

(a) 2D-axisymmetric perspective.

(b) Cross-section of the 3D projection.

Figure 4.10: Laser paths before and after revolution.

In order to model a moving Gaussian beam, the built-in profile in the *Deposited Beam Power* node is replaced by a user-defined deposited beam power density, Q. Equation 3.10 is defined in the *Variables* node along with the location of the laser focus. The point where the laser focus is at varies with time and can be defined as

$$r_f = v\,t \quad (4.13)$$

where the laser moves at a constant velocity, v. When r_f reaches the end of the selected boundary, r_b, the laser automatically deactivates. Therefore, a temporal distribution is no longer required.

Figure 4.11 compares the phase changes at three distinct points, centre of the layer (point A), at one forth of the layer (point B) and at the border (point C), for different velocities, 200 mm s^{-1} and 20 mm s^{-1} and for the same laser power of 300 W and radius focus of 0.01 cm, aiming to analyse the performance of the method developed.

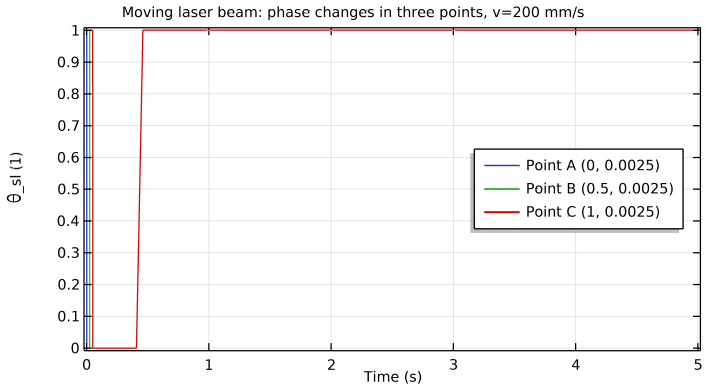

(a) $v = 200$ mm s^{-1}.

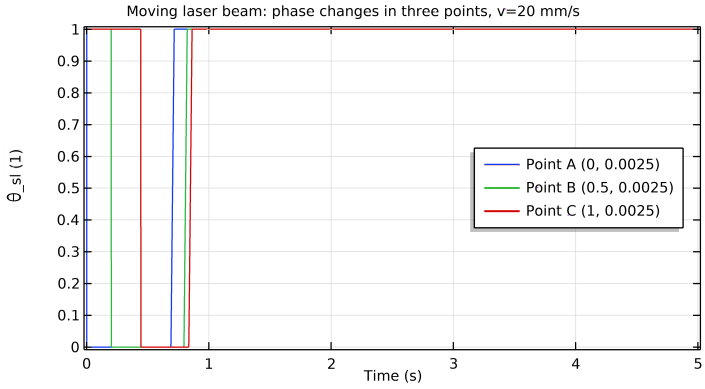

(b) $v = 20$ mm s^{-1}.

Figure 4.11: Phase changes analysed in three points for two scanning velocities.

For the graph in Figure 4.11a, melting occurs at different instants for each points, but solidification occurs almost simultaneously. On the other hand, considering the graph in Figure 4.11b, both melting and solidification occur at distinct instants. In addition to being qualitatively in agreement with the literature, both plots corroborate the relevance of the careful selection of processing parameters.

Implementing a moving laser beam reveals an additional benefit: as long as a path has been defined, the activation condition of the mechanical properties can be more correctly defined.

Activation must occur when the material is in the solid state. Because this is verified in the initial instant, the activation condition must be a conjunction of two conditions: (i) the material is in the solid state and (ii) the laser focus has passed over the coordinate being evaluated. The conjunction of these is always verified even in the case a material undergoes multiple activation/deactivation events. Mathematically, these are represented as

$$\theta_{sl} = 1 \quad \wedge \quad r < r_f \,. \quad (4.14)$$

The *Activation* subnode removes the elastic strains at every instant of activation, i.e., the material is always activated in a zero-stress state, regardless of its history of past activations or deactivations. Figure 4.12 demonstrates the zero-stress state of point B when the material is activated.

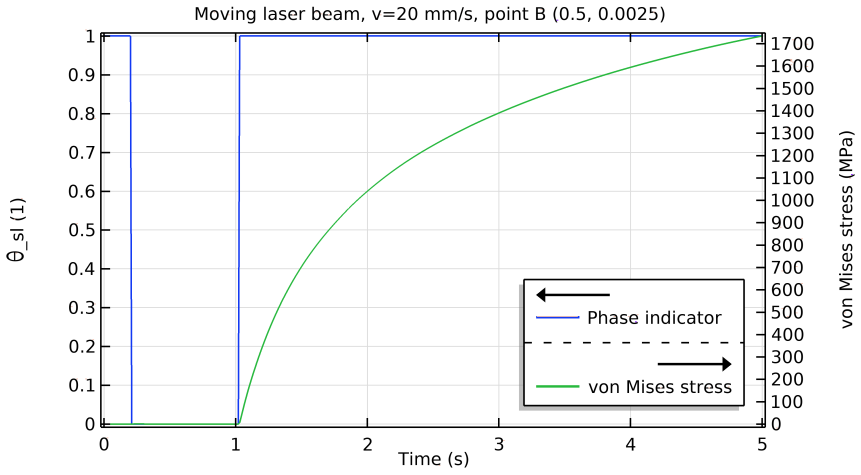

Figure 4.12: Activation condition in point B and for $v = 20$ mm s^{-1}.

After ensuring both phase changes and defining an accurate activation condition, the *Structural Mechanics* module can be implemented with the necessary initial and boundary conditions. The initial displacement field is zero when the material is activated; additionally, a *Fixed* boundary condition is implemented in order to replicate the agglutination of the first layer to the platform.

Finally, the powder phase replaces the solid initial phase by simply changing the mechanical properties of the powder. For modelling effects, the effective thermal conductivity and density of the powder are considered with respect to its porosity. Assuming a porosity of 30 %,

i.e., $\phi = 0.3$, the properties of the powder bed are given by

$$\rho_p = (1-\phi)\,\rho_s + \phi\rho_a\,, \quad (4.15)$$

$$k_p = (1-\phi)\,k_s + \phi k_a\,, \quad (4.16)$$

resulting in an effective density of $3100\ \mathrm{kg\ m^{-3}}$ and thermal conductivity of $4.22\ \mathrm{W\ m^{-1}\ K^{-1}}$. The material phase is essentially distinguished by the variables used in the *Activation* node: the powder properties are adopted whether (i) the material is in the solid state and (ii) the laser focus has not passed over the coordinate being evaluated, i.e.,

$$\theta_{sl} = 1 \quad \wedge \quad r > r_f\,; \quad (4.17)$$

otherwise, the bulk material properties are selected[2]. Recalling Equation 2.2 in Chapter 2, the specific heat capacity is assumed constant in the solid and powder phases.

Lastly, a single mesh is designed for the thermal, structural and phase change modules. A mesh is responsible for the quality of the model: if not sufficiently refined, results may be inaccurate. On the other hand, an extremely fine mesh would not be computationally efficient. The most convenient approach is to refine the areas where the laser is applied on and keep the mesh coarser in farther regions.

As the structural simulation requires three degrees of freedom for each node, in contrast to the thermal simulation, that requires only one, usually a different, coarser mesh is used intending to reduce the computational cost. In this case, a single physics-controlled meshing sequence evaluates the type of simulations to automatically determine the most suitable size and sequence operations required to create a problem-adapted mesh [113], which resulted in the mesh in Figure 4.13. Some publications [91] refer that the mesh must be sufficiently small such that the distance between two nodes is equivalent to one quarter of the laser spot radius. As that strategy would be unfeasible, the only meshing requirement imposed is that, in a 2D perspective, at least one node must be contained in the laser spot. Convergence tests have been conducted to determine the suitability of the chosen mesh.

[2] in contrast to thermal conductivity, density still assumes a constant value for the solid compacted and liquid phases.

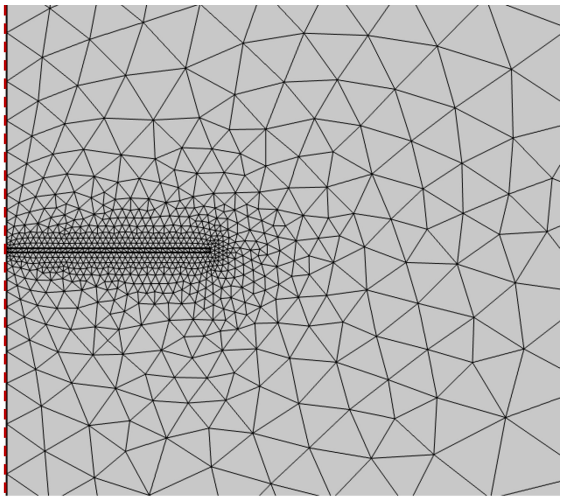

Figure 4.13: Mesh redesign for the cylindrical model, first layer.

4.2 Multi-layer Modelling

Regardless of the number of layers, which depends on the layer thickness, a code in MATLAB is developed in order to reproduce the physical phenomena modelled for a single layer for n layers. Algorithm 1 represents a pseudo-code of the model of the cylinder. The detailed code can be found in Appendix B, Section B.1.

Algorithm 1 Pseudo-code: Cylinder

```
Define parameters: material and laser properties
Define functions and variables
Define materials
Define the layer and build chamber geometries
Define boundary, initial and activation conditions
Define mesh and study settings
for each iteration do
    Add a layer
    Attribute materials, modules and boundary conditions to the new domains
    if first iteration then
        Attribute initial and activation conditions
    else
        Import the final conditions of the last iteration as initial conditions for the previous
        layers and attribute initial conditions for the added layer
    end if
    Build new mesh for the whole domain
    Export temperature and displacement data of the whole domain in the final instant
    Plot the geometry, temperature, displacement and von Mises stress graphs
end for
```

Parameters, i.e., material and laser properties, dimensions, functions, variables, geometries, boundary, initial and activation conditions, mesh and study settings are initially defined such that these can be sequentially assigned to the correspondent elements. The outline of the program is essentially identical to that of the FEM, except for the layer addition and what it entails.

The code is designed to repeat the process for as many iterations as necessary, with the number of iterations equivalent to the number of layers. For each iteration, a new layer is added by simply adding a rectangle as a new domain and the materials, modules and boundary conditions are assigned to the correspondent elements. It should be mentioned that not all domains perform the simulations of the three modules; for instance, the build chamber only performs thermal simulations while the processed part is affected by thermal and structural contributions and enables phase changes. The selection of elements is attained by means of a rectangular selection box whose dimensions are defined by entering the maximum and minimum values in r- and z-directions. The entities that are completely inside the box are selected. The selection of more than one entity is accomplished by means of a conjunction of selection boxes. Some box coordinates are iteration-dependent in order to be adapted to the layer addition.

The key point of the construction of the program is the discrepancy between the modelling of one layer and multiple layers: the first iteration follows a slightly different modelling pattern from the one adopted by the remaining iterations. This distinction is firstly verified whilst attributing the initial conditions: in the first iteration, the layer and the build chamber have the same initial temperature and the layer is in the non-consolidated solid state; however, for n layers, the top layer is added to the previous consolidated layers and, therefore, must assume an initial temperature and powder state, while the previous layers must adopt the final conditions of the last iteration as initial conditions. Thus, at the last time of each iteration, these conditions have to be exported in order to be imported as initial conditions for the next iteration. It is important to note that the initial conditions of the structural module are not defined for $t = 0$ s, but for the instant when the activation condition is verified.

The activation condition depends on the position of the layers as well. In the first iteration, the layer is in the non-consolidated solid state and is subject to an irreversible phase transformation; otherwise, the top layer is in the powder form and is added to the bulk solid layers where only reversible changes can occur. Hence, the activation condition for the initially powder layer is the one described above whereas a new condition is introduced for the

remaining iterations according to

$$\begin{cases} \theta_{sl} = 1 \quad \wedge \quad r < r_f, \quad n = 1 \\ \theta_{sl} = 1 \quad \wedge \quad z < t_k\,(n-1), \quad n > 1 \end{cases} . \tag{4.18}$$

Finally, a new mesh has to be constructed for all the entities. The contribution of MATLAB resulted in a superior meshing approach: the physics-controlled mesh is redesigned at each iteration, creating a refined mesh suitable for each "new" setup. Figure 4.14 shows the mesh redesigned for the second iteration (about 3959 plus 16472 internal degrees of freedom).

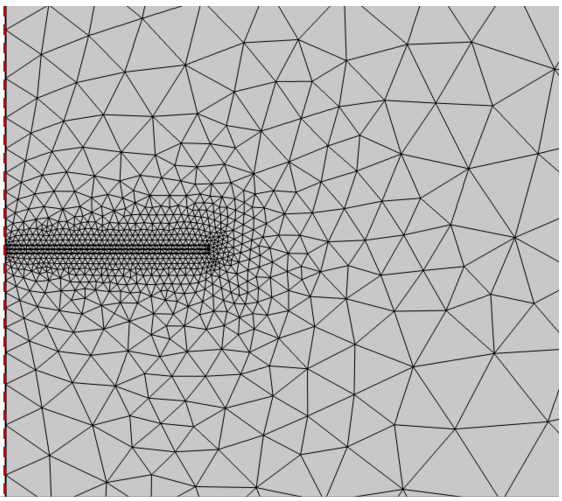

Figure 4.14: Mesh redesign for the cylindrical model, second iteration.

After the processing of each layer, a new one is geometrically added and the necessary conditions are attributed to the corresponding entities until the last iteration.

Chapter 5

Modelling of the Dog-bone Cylindrical Specimen

Before addressing the manufacturing of the LLM, a set of specimens were tested with the purpose of broadening expertise on the additive processing; likewise, the model described in this chapter is intended to stimulate the development of a similar model that would optimise the fabrication process of the Large Lens Mounting. Although a dog-bone cylinder is a fairly simple geometry when compared to LLM, the modelling of its manufacturing is more elaborate than the cylinder described in Chapter 4. The general modelling approach can be adopted, but some modifications and improvements must be accounted for. The dog-bone shape cannot be obtained by the simple superposition of rectangles in a 2D-axisymmetric perspective and, in a validation context, must be as identical as possible to the ones experimentally tested. Therefore, the 3D geometry, whose external and internal diameters are of 0.6 cm and 0.25 cm, respectively, needs to be imported from a CAD file to COMSOL. Figure 5.1 shows a 2D-axisymmetric representation of the imported 3D dog-bone with a height of 10 cm.

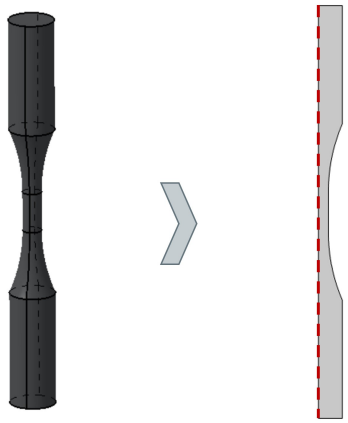

Figure 5.1: Conversion of the 3D dog-bone cylinder into a 2D-axisymmetric geometry.

5.1 Single-layer Modelling

The single-layer modelling of the dog-bone cylinder and the regular cylinder is only distinguishable in the dimensions of the first layer. Because this model will serve as a tool to perform parametric studies, the priority henceforth is to improve its reliability. On that account, some modifications could add further robustness to the thermoelastic model.

Model revision I. *Thermoelastic modelling of a single layer with the corrected material properties.*

Despite not being important to the thermal problem, the liquid Ti-6Al-4V density is discriminated from the bulk solid density. Analysing the work of Schmon et al. [114], the density of the liquid phase varies linearly from 4086.5 kg m^{-3} at T_m to 3600 kg m^{-3} at 3000 K. As implementing a temperature-dependent density would be costly - and probably an insignificant improvement of the predictions -, an average approximated value of 3800 kg m^{-3} is adopted instead. Moreover, the temperature-dependent properties of argon previously adopted from the COMSOL Library are replaced with carefully assessed constants (cf., Appendix A, Table A.2).

During the revision of the powder-dependent properties computed in Chapter 4, a disagreement with the literature is found for the thermal conductivity of the powder: k_p is expected to be at least one order of magnitude lower than k_s. Hence, a model proposed by Yagi and Kunii [99] for porous metallic beds, and more recently revised by Xue and Barlow [115], is used to compute the thermal conductivity of the powder bed:

$$k_p = 6.3 + 22\sqrt{0.09k_s - 0.016}\left[\frac{k_s(1-\phi)}{(k_s/k_a)(10^{0.523-0.594\phi})-1}\right] . \quad (5.1)$$

From Equation 5.1, the effective thermal conductivity of the powder is 0.33 W m^{-1} K^{-1}, which corresponds to the same order of magnitude of the values used by Chiumenti et al. [74] and Proell et al. [81].

Mechanical properties suffered simplifications regarding thermal variations; this is specially imprecise in the case of the Young's modulus. As temperature raises, the Young's modulus tends to decrease. By adopting a constant value measured at the ambient temperature, the computed stresses are significantly overestimated. Nonetheless, this is a necessary simplifi-

cation in order to obtain acceptable computation times.

Density, thermal conductivity and specific heat capacity are ultimately defined for the three material phases. After revising each property adopted heretofore and successfully approving its suitability according to the literature, the importance of the implementation of the powder bed and the platform is investigated.

Model revision II. *Thermoelastic modelling of a single layer with the additional powder bed and platform domains and the corrected material properties.*

Temporarily, while the iteration methodology is not assessed, the characterisation of a single layer is performed by a line segment whereby the cylinder is divided in two domains. The powder bed and the base plate domains have been neglected in the model described in Chapter 4 due to the further computational weight these might carry. However, neglecting the contribution of their disparate thermal conductivities have a negative impact on the predictions: while the platform is typically made of a highly thermally conductive material and sufficiently large to function as a heat sink aiding the solidification process [23], powder heat conduction is less efficient because only powder regions in physical contact promote conductive transfer. Adding new entities to the model requires the implementation of new geometries, materials, initial conditions and properties. The powder bed properties can be adopted from the powder previously characterised; however, their attribution to the entity follows a different strategy since the powder surrounding the part is permanently in the powder form, in contrast to the powder to be processed. Therefore, the powder bed properties are simply assigned to it while the powder to be processed requires the Boolean expression in Equation 4.17. Moreover, the definition of the powder bed domain is somewhat unsophisticated: dividing the surrounding atmosphere in two domains can be achieved by simply extending the line segment that splits the cylinder in two. The base plate is introduced as a rectangle with a 2-cm thickness. As a steel-made bulk structure, it is affected by the generation of distortions as a result of the thermal cycling of the procedure that, in turn, may induce distortions in the part being manufactured. Thus, the base plate is introduced to the *Structural Mechanics* node as a permanently activated domain. The properties of the platform are adopted from Steel AISI 4340 that can be found in the COMSOL Library and in Appendix A, Table A.3. The implementation of both entities can be found in Figure 5.2 along with the updated dimensions of the build chamber to more representative values.

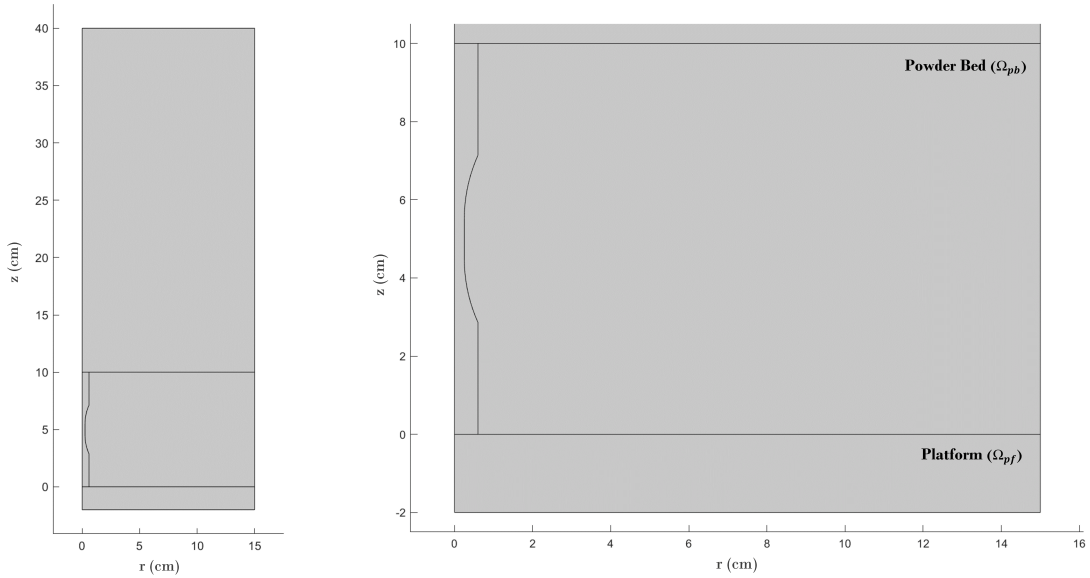

(a) Complete view. (b) Close-up view.

Figure 5.2: 2D-axisymmetric representation of the setup with the platform and the powder bed.

Aiming at perceiving the effect of the new entities, the thermal field is assessed for the same conditions for two setups: the one where the platform and the powder bed are absent and the one described in Figure 5.2. Figures 5.3a and 5.3b are plotted for $t = 0.5$ s and Figures 5.3c and 5.3d for $t = 5$ s.

A circular pattern of colours representing the thermal gradients around the upper boundary stands out in Figures 5.3a and 5.3c, but in Figures 5.3b and 5.3d only a malformed oval - with a tendency to the base plate distinctly identified in Figure 5.3d - can be recognised. This asymmetrical shape underlines the heat exchange from the boundary to the surroundings unevenly. Additionally, at the last instant of the computation, $t = 5$ s, the maximum temperature verified in Figure 5.3c is about 57 % higher than that in Figure 5.3d. Thus, the impact of these entities on the simulations, in particular the role played by the platform as a heat sink, is indisputable and must not be neglected.

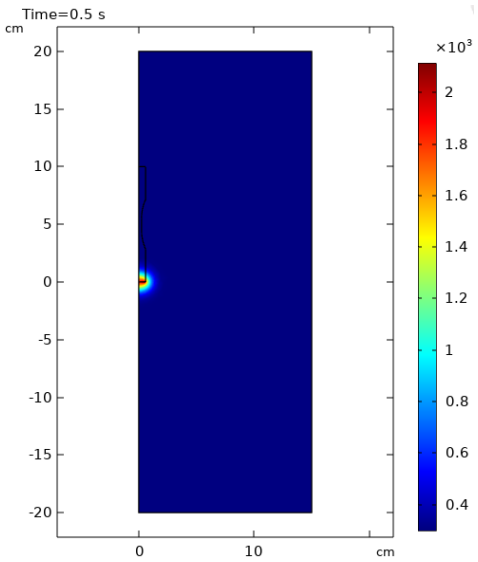

(a) Setup without the platform and the powder bed for $t = 0.5$ s.

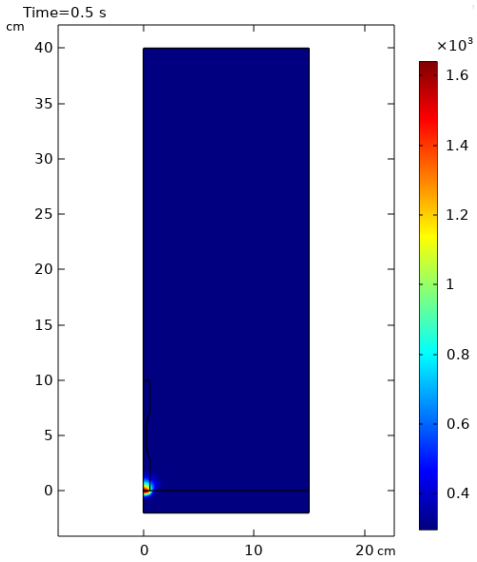

(b) Setup with the platform and the powder bed for $t = 0.5$ s.

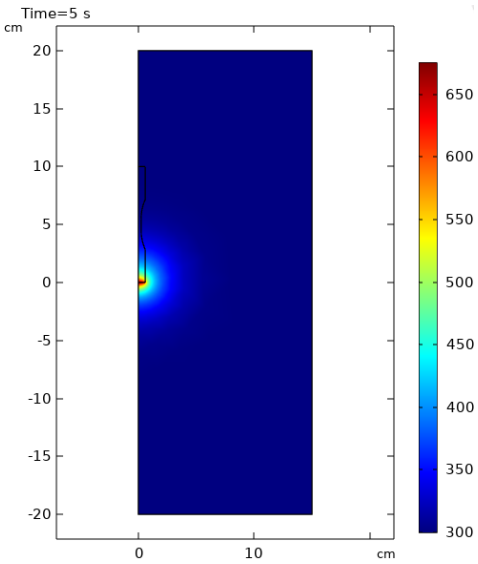

(c) Setup without the platform and the powder bed for $t = 5$ s.

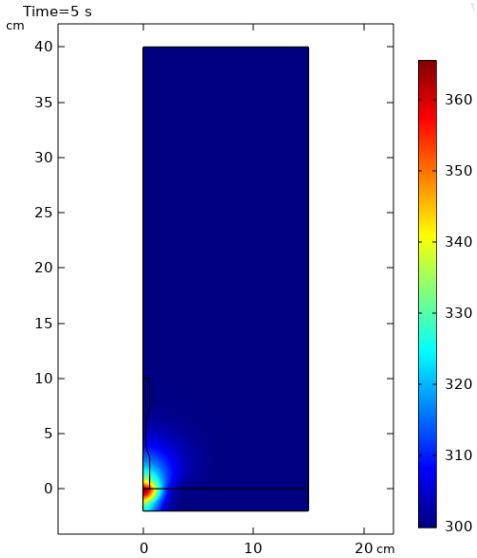

(d) Setup with the platform and the powder bed for $t = 5$ s.

Figure 5.3: The influence of the powder bed and the platform in the thermal field for $t = 0.5$ s and $t = 5$ s.

As the purpose of the platform becomes clear, it is interesting to further analyse the influence of the powder bed, which is somehow ambiguous. Its thermal conductivity is one order of magnitude higher than that of argon (considering that the gas is motionless). Figure 5.4 compares the temperature fields assuming the overestimated and the realistic thermal conductivity of the powder for the same problem conditions. Assuming that a single-layer thickness of 50 µm would be insufficient to reveal a thermal pattern, the thickness of the layer - and the height of the powder bed - is set to 0.25 cm.

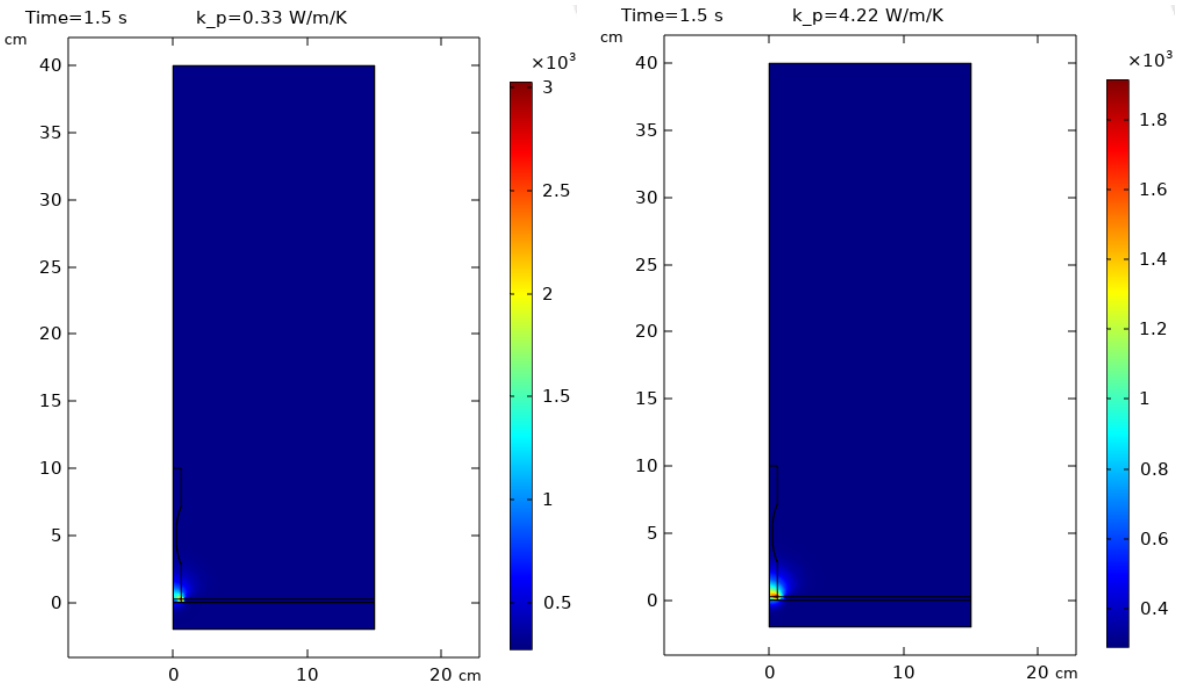

(a) $k_p = 0.33$ W m^{-1} K^{-1}. (b) $k_p = 4.22$ W m^{-1} K^{-1}.

Figure 5.4: The influence of the thermal conductivity of the powder bed in the thermal field for $t = 1.5$ s.

Unsurprisingly, an overestimated thermal conductivity of the powder aids heat dissipation through the powder bed, thereby implying that the layer being processed reaches a lower maximum temperature value when compared to a reduced thermal conductivity. The disparity of the temperature values noted in Figure 5.4 consents the correction of this parameter.

Having discussed the importance of the thermal conductivity of the powder bed, a theoretical model proposed by Sih and Barlow [102] is investigated in order to assess the emissivity of the powder, ε_p, in the conditions of the problem:

$$\varepsilon_p = A_c \varepsilon_c + (1 - A_c)\, \varepsilon \,, \quad (5.2)$$

where ε_c is the emissivity of cavities of the powder bed and A_c is the area fraction of the surface that is occupied by the emitting cavities given by

$$\varepsilon_c = \frac{\varepsilon\, [2 + 3.082(\frac{1-\phi}{\phi})^2]}{\varepsilon\, [1 + 3.082(\frac{1-\phi}{\phi})^2] + 1} \,, \quad (5.3)$$

$$A_c = \frac{0.908\phi^2}{1.908\phi^2 - 2\phi + 1} \,. \quad (5.4)$$

Analytically, this property is implemented as the previous powder processing properties, i.e.,

if $\theta_{sl} = 1 \wedge r > r_f$, then ε_p, else ε. The emissivity of the powder given by Equation 5.2 is 0.43, which is insignificantly higher than that of the solid phase. In fact, distinguishing the emissivity of both phases has no significant impact as observed in Figure 5.5 by the overlapping of the thermal fields evaluated at point $B = (0.3, 0.0025)$. Thus, $\varepsilon = 0.35$ remains constant regardless of the material phase.

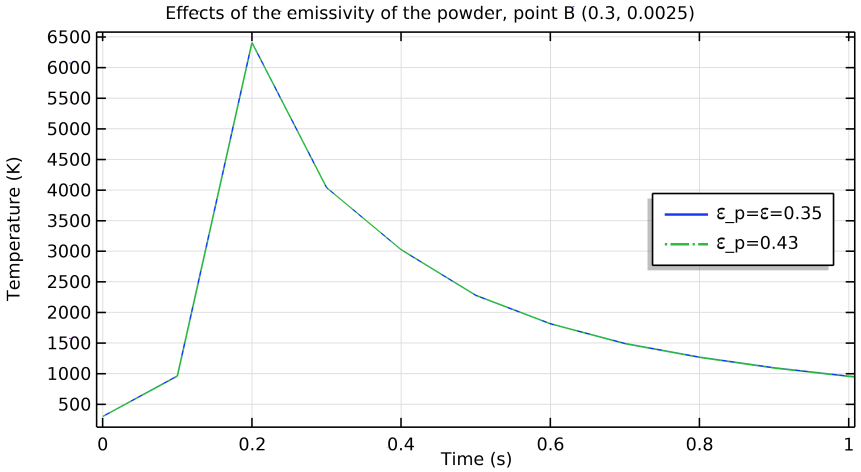

Figure 5.5: The influence of the emissivity of the powder in the thermal field.

After achieving what indicates to be a more realistic model, the contribution of convection can be evaluated once again by assigning a non-null value to the velocity vector in order to obtain a more deep understanding of its impact (Figure 5.6).

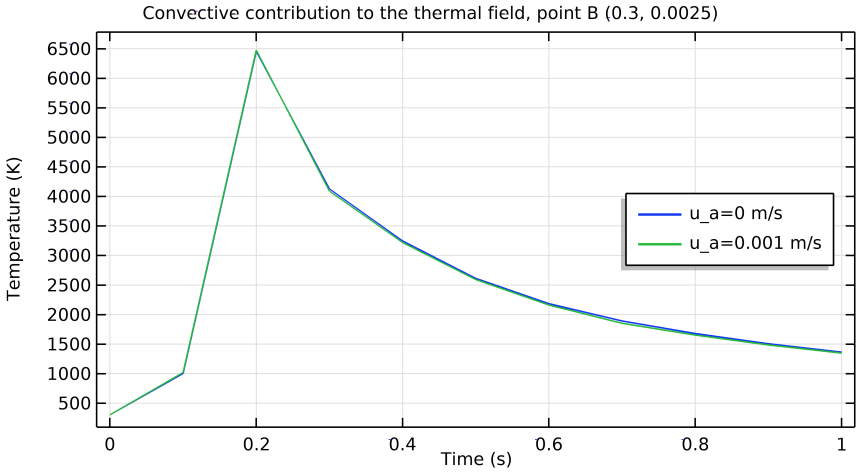

Figure 5.6: The influence of convection in the thermal field.

Throughout the heating phase, both curves, i.e., for $\mathbf{u}_a = 0$ and $\mathbf{u}_a = 0.001$ m s^{-1}, overlap; however, during cooling a slight distinction can be observed. According to the plot in Figure 5.6, the convective mechanism enables a more rapid cooling, albeit barely noticed, when

compared to the absence of convection. The fact that the velocity vector adopts an unrealistic small value that still has a perceivable impact on the temperature field suggests that the convective mechanism must not be discarded.

As long as the heat mechanisms are assessed, the insulation condition set at the external boundaries of the build chamber can be updated in order to reproduce the dissipation of the energy to the exterior of the chamber; hence, Equation 3.12 replaces Equation 4.2.

The thermal conductivity is recognised to be one of the most decisive parameters of the problem and its dependency on the temperature is well formulated. Accordingly, a temperature-dependent thermal conductivity function of Ti-6Al-4V is adopted from Mills [116] and compared to the phase-dependent functions previously used (Equation 4.11). On the one hand, utilising a function that assumes only a local temperature-dependency, i.e., around T_m and T_s, seems to be a bizarre representation of the thermal conductivity of this titanium alloy. On the other hand, the function proposed by Mills would be computationally demanding. In Figure 5.7, the functions adverted thus far are graphically compared, along with a variation from the function recommended by Mills and denoted by "Alternative".

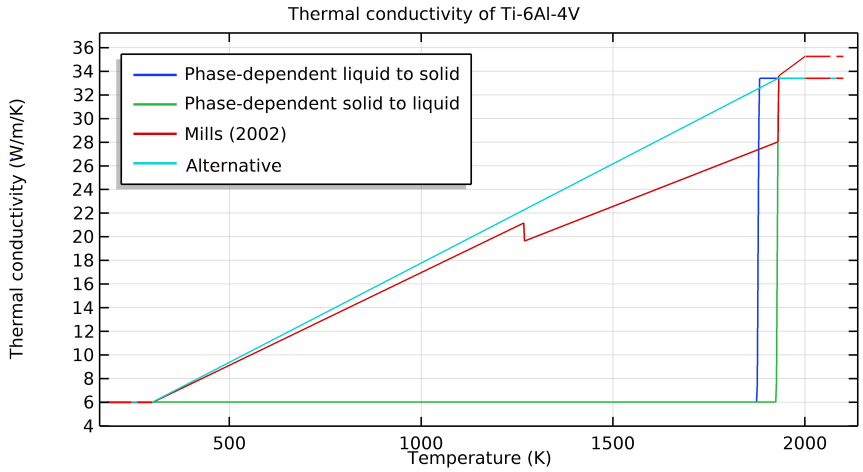

Figure 5.7: Thermal conductivity of the titanium alloy, Ti-6Al-4V, represented by different functions.

The novel, simplistic function is defined at certain temperature points and calculated through linear interpolation for intermediate points as

$$k_{Alt}(T) = \begin{cases} 6, & T < 300 \\ 0.0168T + 0.9586, & 300 < T < T_t \\ 33.4, & T > T_t \end{cases} . \quad (5.5)$$

As far as the mesh for the single-layer modelling is concerned, no modifications have been carried out: a physics-controlled meshing sequence is designed for the three modules with a refinement in the HAZ and a coarser distribution in farther regions.

5.2 Multi-layer Modelling

Because of the narrowing and the strict dimensions of the dog-bone cylinder, the geometry must be imported from a CAD file, which implies that the entire part is explicitly present in the geometric frame throughout the simulations. Thus, two options are studied in order to replace the representation of layers as rectangles: (i) using of coordinates to define the layer boundaries and (ii) using of line segments for the same purpose. The definition of the layer as suggested in option (i) would be quite simple; however, the application of boundary conditions, namely the laser deposition, would be complex since it would have to be modelled as an activation function, e.g., a coordinate-dependent (as opposed to time-dependent) triangular function thought the z-axis. Despite not being tested, this approach is anticipated to involve convergence problems, inaccurate predictions and time consuming simulations. Option (ii) seems to be a more feasible strategy: line segments are implemented in the geometric frame splitting the geometry and, on the other hand, being split, enabling the assignment of boundary conditions. For the first iteration, the dog-bone cylinder is divided in two and, in any other case, in three different domains that can be selected separately by means of selection boxes such that materials, properties and conditions can be assigned to them. The processed material and the powder bed are selected by two distinct height-varying boxes (with different horizontal dimensions) that expand upwards while remaining fixed at the bottom as described in Figure 5.8. On the other hand, the layer being processed is defined by a position-varying box that preserves its size. The entities positioned above the layer and powder bed are defined as gas. Each domain requires particular properties and initial conditions; whereas the added powder, either the part being processed or the powder bed, has the same initial temperature at each iteration, the remaining domains, i.e., argon, the platform, the processed material and the remaining part of the powder bed, are assigned the conditions of the final instant of the previous iteration. Furthermore, some entities, albeit adopting the same properties, require that these are assigned differently as it has been explained in this chapter. Thus, for three materials there must be five property attributions: (1) argon, (2) the platform, (3) the material processed (that cannot be reversed to powder),

(4) the powder bed (that does not suffer any state transformation) and (5) the powder to be processed.

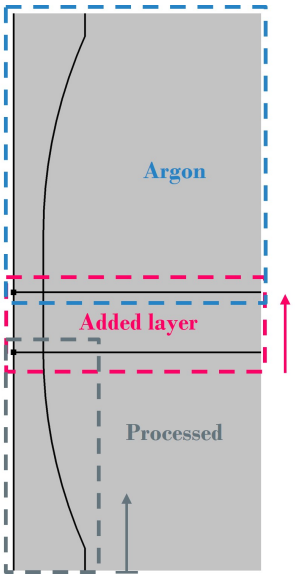

Figure 5.8: Option (ii): selection of boundaries and domains by means of selection boxes.

A complementary goal of this project is the assessment of the residual stresses, which is computed when the part has reached an equilibrium. Accordingly, a stop condition defined in the *Time-dependent Solver* node is imposed aiming at stopping the solver when specified conditions are fulfilled. The expression to be verified in this case is $T_{max} \leqslant T_{amb}$, i.e., whenever the maximum temperature registered in the part is less than or equal to T_{amb}, the computation is stopped and the stresses are evaluated at that instant. While the cooling period of each layer is as long as the necessary recoating time, i.e., only a few seconds, the last iteration must be extended for a few hours such that the temperature of the material can be as low as required.

The versatility of the *Stop Condition* subnode adds value to the model. Other parameters, namely the cooling period and the maximum, average or minimum temperature reached, can be included in the stop expression. Particularly, when evaluating a part in which a certain maximum stress value must not be exceeded, the subnode can be implemented in order to cancel the computation if the undesired condition is verified, thereby saving computation time.

Algorithm 2 outlines the model for the dog-bone cylinder that has been described in this chapter. The detailed code can be found in Appendix B, Section B.2.

Algorithm 2 Pseudo-code: Dog-bone Cylinder

```
Define parameters: material and laser properties
Define functions and variables
Define materials
Import dog-bone cylinder 2D-geometry and create two line segments for the layer boundaries and the build chamber and platform geometries
Define boundary, initial and activation conditions
Define mesh and study settings
for each iteration do
    Define the position of the upper line segment
    Attribute materials, modules and boundary conditions to the new domains
    if first iteration then
        Attribute initial and activation conditions
        Deactivate the lower line segment
    else
        Define the position of the lower line segment
        Import the final conditions of the last iteration as initial conditions for the previous layers and attribute initial conditions for the added layer
        Attribute one activation condition for the previous layers and a different one to the added layer
    end if
    Build new mesh for the whole domain
    if iteration is not the last then
        Attribute a small study time to simulate the addition of layer/dissipation time
    else
        Attribute a long study time whose last time is defined by a stop condition
    end if
    Export temperature and displacement data of the whole domain in the final instant
    Plot the geometry, temperature, displacement and von Mises stress graphs
    Display the instant at which the last iteration stopped
end for
```

Once again, a problem-adapted mesh is created at each iteration as shown in Figure 5.9 for the last iteration (about 25473 plus 15939 internal degrees of freedom).

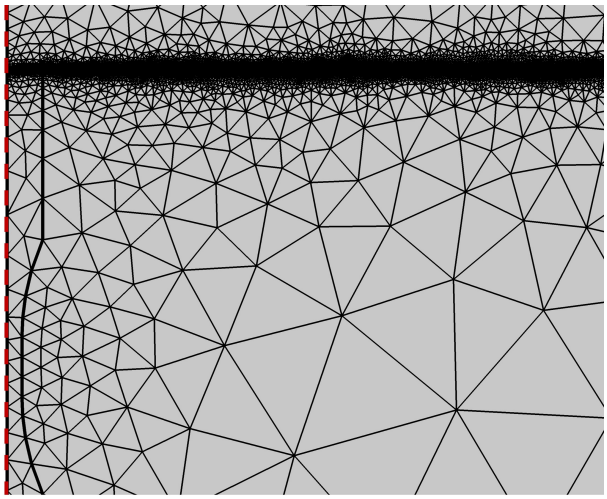

Figure 5.9: Mesh redesign for the dog-bone cylindrical model, last iteration.

The current mesh approach is undoubtedly advantageous; however, the upper part of the powder bed, which is not being thermally affected, is excessively refined. This raises the computational costs of the simulation, but does not negatively affect the predictions. On that account, the mesh does not suffer modifications since it would require a more sophisticated coding in order to manually create an iteration-dependent mesh, which would presumably have a negative effect on the simulation time.

COMSOL automatically detects the most suitable solver for solving the systems of linear equations of each simulation; for both cylindrical models, MUMPS is the solver adopted.

5.3 Model Validation

The validation of finite element models is the verification that modelling premises and, subsequently, analysis conclusions are valid. Thus, numerical fatigue tests are carried out and compared to the fatigue results obtained experimentally. The parameters must be identical to the ones used in the manufacturing of the cylindrical specimens, accounting with uncertainties in some modelling parameters. Table 5.1 discriminates the experimental parameters in contrast to those adopted in the numerical model.

Inevitably, differences can be identified between column two and three. The numerical processing parameters that do not match the experimental ones are represented in **bold**. Because the manufactured specimens are longer than the cylinder whose design has been exported from the CAD file, the layer thickness is changed from 60 μm to 100 μm, which allows

Parameters	Experimental	Numerical
Build chamber dimensions	⌀ 300 mm × 400 mm	⌀ 300 mm × 400 mm
Laser power (P)	500 W (Max 450 W)	$500 \times 0.9 = 450$ W
Layer thickness (t_k)	**60 µm**	**100 µm**
Number of layers (n)	**1438**	**1000**
Laser focus radius (R_g)	50-250 µm	100 µm
Scan velocity (v)	**Max 3000 mm s^{-1}**	**32 mm s^{-1}**
Inert gas	Argon	Argon
Temperature of the gas (T_a)	**293 K**	**473 K**
Platform temperature (T_{pf})	473 K	473 K

Table 5.1: Experimental and numerical processing parameters.

for the processing of a part with a constant layer thickness. Consequently, the number of layers decreases to 1000.

The data-sheet provided by the manufacturer indicates a range of laser focus radius, from 50 to 250 µm, that can be adopted. Thus, a typical value of 100 µm is used.

The FEM was designed such that the fabrication occurs in the z-direction and the specimens were manufactured with different build orientations; thus, the results should be compared to those of the horizontally-built specimens. On the account that the scanning pattern was unspecified, the scheme previously defined is adopted assuming a constant laser velocity. It should be noted that the laser velocity used in the manufacturing follows a 2D path, while the one modelled follows a line path; therefore, in order to assess the correspondent 1D velocity, the length of the approximated spiral needs to be assessed. The perimeter of the spiral can be calculated by the general equation of the Archimedean spiral in polar coordinates; in order to simplify the calculations, an approximation based on concentric circles can be used, rather than considering a true spiral (specially because a spiral is already an approximation of the scanning pattern), which is given by

$$l = \bar{l}\, n_t = \frac{2\pi\, \bar{R}\, r_b}{h}\,, \quad (5.6)$$

where $\bar{l}$ is the average length obtained through the average radius of the spiral, $\bar{R}$, n_t is the number of turns of the spiral which depends on the inner and outer radius, 0 and r_b, respectively and on the hatch spacing, h.

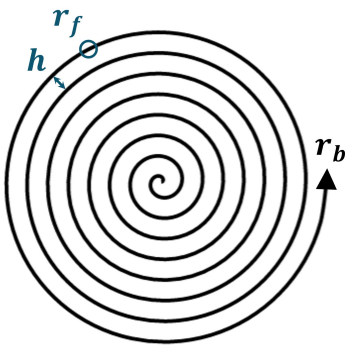

Figure 5.10: Schematic of an Archimedean spiral.

Assuming that $h = 0.02$ cm, the length of the spiral is 56.5 cm, which corresponds to a velocity of 3000 mm s^{-1}. As the length covered by the laser in the 2D model is 0.6 cm, the correspondent velocity is 32 mm s^{-1}. This value has been verified by applying the equation of the Archimedean spiral.

It would be expected that the laser power would require a similar conversion, but the units required by COMSOL for the power input are W m^{-2}. It has been noted that, although the power provided by the laser is 500 W, the maximum power on the workpiece is 450 W. Therefore, a laser energy absorption coefficient, η, of 0.9 is adopted.

Experimentally, a large set of dog-bone specimens, distinguished according to their building direction, were subjected to fatigue tests [117]. The tests were performed for 2×10^6 cycles with a repetition rate of 20 Hz and concluded that the specimens never yield for stresses under 500 MPa. It is known that the maximum stress, σ_{max}, applied was 630 MPa, causing the vertically-built specimens to yield at different numbers of cycles in the order of 10^4 (2.8×10^4, 5.8×10^4 and 7.5×10^4); however, the amplitude of the stress is uncertain. Therefore, the numerical fatigue tests are performed uniquely for $\sigma_{max} = 630$ MPa, but with different stress amplitudes, σ_a, represented in Figure 5.11. There are three available methods in COMSOL from which one can choose that allow for the computation of the *Fatigue limit*; the selected method, *S-N curve*, requires the definition of the curve of applied stress against number of cycles to failure obtained by the experimental tests. In order to account for a mean stress correction, out of three methods, the Soderberg method was selected for consisting in a more conservative approach that predicts failure assuming the yield stress, instead of the ultimate tensile strength.

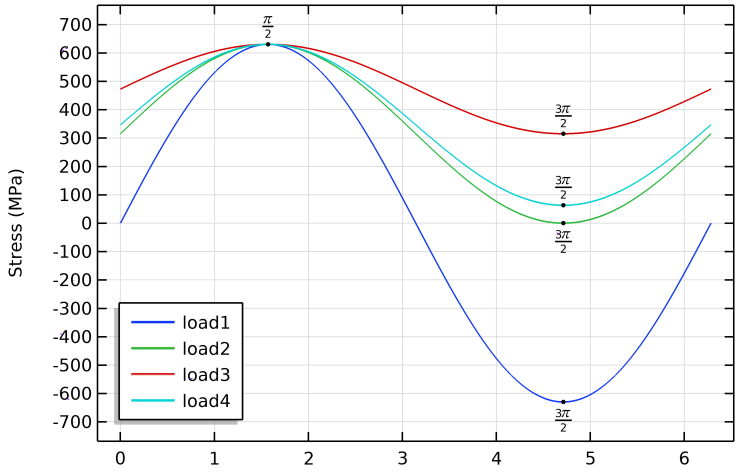

Figure 5.11: Comparison of four loading cases for one cycle, whose stress ratios are $R_{load1} = 1$, $R_{load2} = 0$, $R_{load3} = 0.5$, $R_{load4} = 0.1$.

The results were very similar for the four cyclic loadings; in fact, the number of cycles at which the specimen yielded for all of the cases is in the order of magnitude of 10^3 - one order of magnitude lower that the one obtained experimentally. A more explicit insight on the results is available in Figure C.1 in Appendix C.

It is not unexpected that the results differ between the numerical and experimental tests; the uncertainties faced when defining the process parameters and fatigue test conditions may have triggered the dispersion of results, as well as the conservative mean stress correction method. Moreover, it should be noted that the lack of consistency of the results is usually a characteristic of the fatigue tests, which indicates that these are ineffective as a validation strategy. Although the fatigue parameters, including the S-N curve required by the *Fatigue* node in COMSOL, are in line with the experimental tests, the fidelity of these cannot be ascertained.

Chapter 6

Parametric Studies

6.1 Methodology

Parametric studies require a conscientious selection of the process parameters to be evaluated. The effects of the **laser power**, P, and the **scan velocity**, v, are easily predicted without the aid of FEA, and the variation of the scan speed has, to a certain extent, already been tested in Chapter 4. Additionally, the **hatch spacing**, h, cannot be individually evaluated; the 2D-axisymmetric approach adopted has converted hatch spacing into a scan velocity property, according to Equation 5.6. The analysis of the **pattern of the laser scanning** would be an interesting topic of study; however, because the 2D perspective only allows two possible paths - the one previously adopted, $r_0 \rightarrow r_b$, and the reversed path, $r_b \rightarrow r_0$ -, it would be more valuable to assess parameters that enable higher flexibility. The remaining parameters are the **layer thickness**, t_k, and the **preheating of the platform**, T_{pf}. The effect of these parameters has been discussed separately in Chapter 2, so it would be beneficial to perform a joint evaluation not only of these two, but also of the **preheating of the powder bed**, T_{pb}. Lastly, it has been decided to study the interference of these parameters in the processing of steel, aluminium and, evidently, titanium powder alloys. A reference model is used in order to aid comparisons.

6.1.1 Layer Thickness and Preheating Temperatures

The parameters quantification method is in line with the range of AM experimental values. The range of possible layer thicknesses varies from the powder particle size to a height where a full layer melting is still attainable. Generally, the thickness of each layer can be as small as 50 μm, but not higher than 200 μm. It is anticipated that stresses are inversely proportional to the layer dimensions; thus, only the extreme values of the range are numerically tested. An analogous methodology is imposed for the preheating temperatures: the initial temperature of the powder bed only assumes the temperature of the gas, 300 K, thereby assuming that

there is no preheating, or a temperature of 700 K.

During the formulation of the parametric studies, the doubt between whether the platform is initially, as the name suggests, or constantly heated motivated the comparison between both approaches. For that reason and to clarify the impact of a higher temperature of the platform, the temperatures considered are 500 K and 700 K.

According to the values used in the intermediate tests mentioned in Chapters 4 and 5, the reference model is defined by a gas temperature, T_a, of 300 K, no preheating conditions, i.e., $T_{pb} = T_{pf} = 300$ K and a small layer thickness of 50 µm.

6.1.2 Materials

The materials and alloys to be studied have been selected according to their applicability and literature availability in the AM field. Along with the titanium alloy for which the model has been prepared, other two, steel and aluminium, alloys have to be specified. The nomenclature used to describe the properties of the new alloys is consistent with that of the Ti-6Al-4V, being distinguished by the name of the alloy in index.

In order to perform a reliable comparison between the processing of different materials, the absorption coefficient, η, has been updated for each alloy; due to the high absorptivity of Ti-6Al-4V, η adopts a value of 0.73.

Stainless steel. The steel alloy 316L has been receiving much attention in the AM industry; thereby, it is used to perform comparative tests regarding the processing parameters. The properties of the new alloy are detailed in Appendix A, Table A.4. Particularly, its solidification and melting temperatures are 1648 K and 1673 K, respectively, and its thermal conductivity is defined as a temperature-dependent property given by

$$k_{316L}(T) = \begin{cases} 7.96 + 0.02T - 4.71 \times 10^{-6}T^2 + 6.27 - 10T^3 - 1.24 \times 10^{-12}T^4, & 300 < T < 1220 \\ 24.8, & T > 1220 \end{cases}. \quad (6.1)$$

The function represented by Equation 6.1 has been adopted from the COMSOL Material Library and is graphically represented in Figure 6.1.

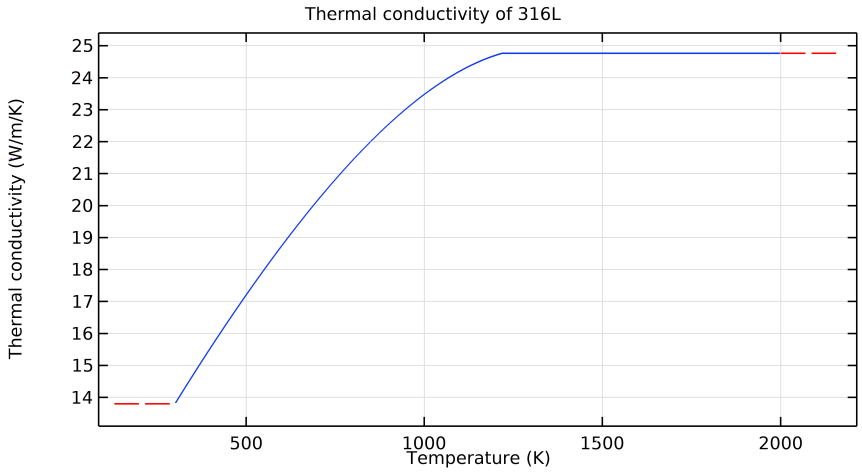

Figure 6.1: Thermal conductivity of the steel alloy, 316L.

Admitting the calculation methods described in Chapters 4 and 5, C_{p_0}, k_p and ρ_p of the stainless steel alloy are detailed in Appendix A, Table A.4. The absorptivity of 316L corresponds to a coefficient of 0.64.

Aluminium. Among the AM processable aluminium alloys, AlSi10Mg is selected to compare with 316L and Ti-6Al-4V. Its solidification and melting temperatures are, respectively, 831 K and 867 K and its thermal conductivity is defined as a phase-dependent property described in Appendix A, Table A.5, along with the remaining properties obtained by the same methodologies as the titanium alloy. The absorption coefficient of AlSi10Mg is 0.32.

6.2 Single-layer Results and Discussion

Figure 6.2 exhibits the temperature and stress fields for the reference model of each material evaluated at point C' where a higher stress concentration is identified, i.e., in the interface of the processed layer, powder bed and platform, defined by $r = 0.6$ cm and $z = 0$. The acknowledgement of this region as a stress accumulator is in agreement with the work of Song et al. [104].

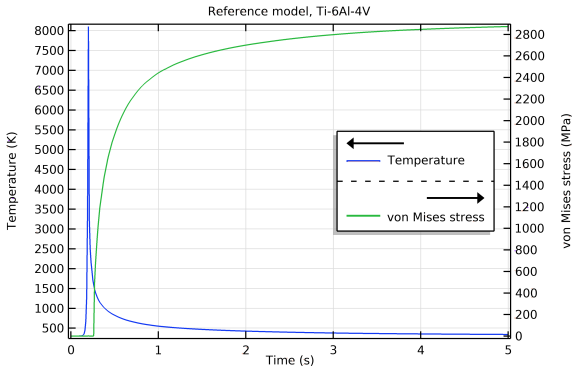

(a) Ti-6Al-4V.

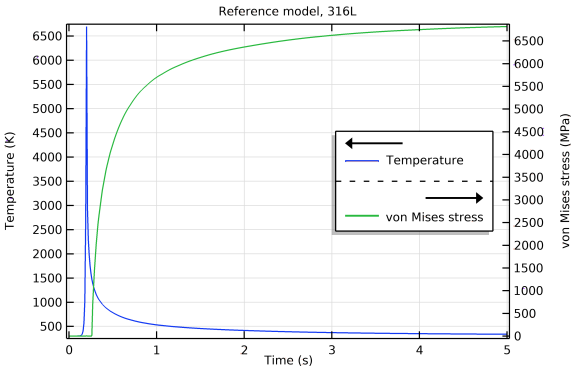

(b) 316L.

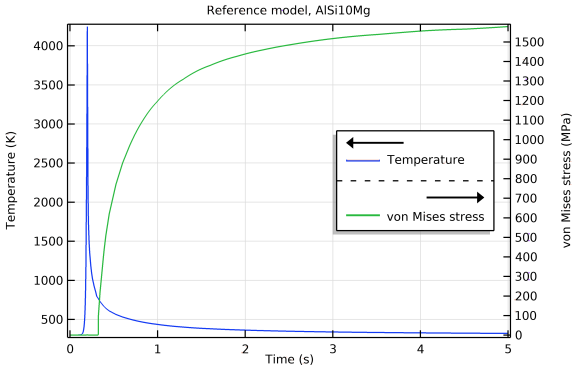

(c) AlSi10Mg.

Figure 6.2: Thermal and von Mises stress fields for the conditions of reference for the three alloys at point C'.

The reference model of the aluminium alloy exhibits both lower stress field and maximum temperature when compared to titanium and steel alloys. In fact, the maximum reached temperature progressively decreases from Figure 6.2a, regarding Ti-6Al-4V, to Figure 6.2c, with respect to AlSi10Mg, which is defined by the absorption coefficient of each material. It is notable that stainless steel sustains a higher stress field. In the following Subsections, the sequel of parameters variation is addressed.

6.2.1 Material Comparison

Results. Figure 6.3 reports the stresses parametrically evaluated at point C' for Ti-6Al-4V at the same instant, $t = 5$ s.

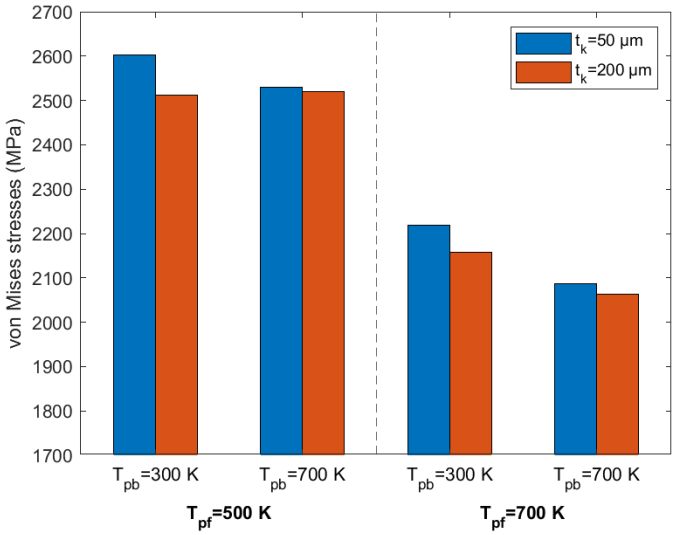

Figure 6.3: Parametric studies of von Mises stress for the Ti-6Al-4V alloy, point C' (0.6, 0), $t = 5$ s.

The most conspicuous observation to emerge from the comparison between the initial temperatures of the platform is a considerable attenuation of the stress values from $T_{pf} = 500$ K to $T_{pf} = 700$ K, implying that higher heating temperatures are more stress-efficient.

According to Figure 6.3, it is apparent that a higher powder bed preheating tends to induce lower thermal stress to the part for both platform preheating cases. Interestingly, the effects stemmed from the powder preheating are well-defined when the platform is heated at 700 K; on the other hand, the first half of the bar chart, defined by $T_{pf} = 500$ K, exhibits a more heterogeneous effect. While a 50-µm layer at 300 K exceeds the stresses provoked by its counterpart for a higher powder bed temperature, an unheated 200-µm layer exhibits slightly reduced stresses when compared to its preheated counterpart. This behaviour appears to be unexpected since the purpose of the preheating, as confirmed by the platform heating, is to decrease the thermal gradients in the part and, consequently, reduce the induced stresses. Furthermore, either combination suggests that smaller thicknesses are more vulnerable to thermal stresses than larger ones.

Figure 6.4 plots the stresses according to the parametrisation previously prescribed for the 316L alloy.

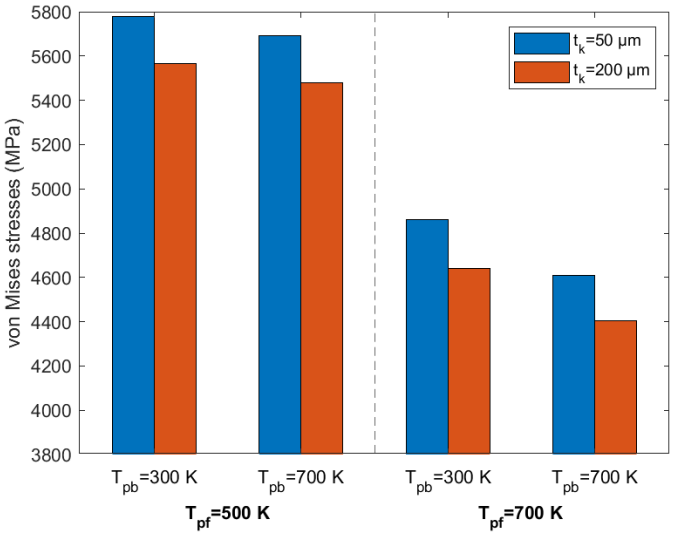

Figure 6.4: Parametric studies of von Mises stress for the 316L alloy, point C' (0.6, 0), $t = 5$ s.

The declining bias along the x-axis of the bar chart offers indisputable evidence for the contribution of preheating and layer thickness variation; consistently to the Ti-6Al-4V graphs, lower powder bed temperatures induce higher stresses in the steel-made single-layer specimens. Correlating the impact of the platform temperatures, a similar deduction can be made: a higher preheating temperature eminently aids stress minimisation. Moreover, the layer thickness exhibits a well-defined and consistent configuration where a higher thickness is responsible for lower stresses. Thus, the combination of a high powder and platform preheating and a low layer thickness allows for a more stress-optimised specimen.

The parametric results for the aluminium alloy, AlSi10Mg, are plotted in Figure 6.5 for the last instant of simulation.

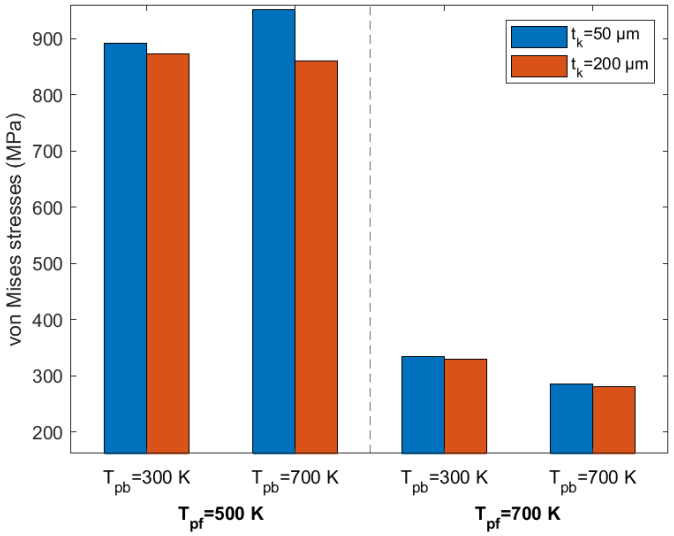

Figure 6.5: Parametric studies of von Mises stress for the AlSi10Mg alloy, point C' (0.6, 0), $t = 5$ s.

Whilst the overall trend originated by different layer dimensions is identical to the ones observed in the titanium and stainless steel alloys, the results are ambiguous as far as the powder heating is concerned. The plots previously analysed, albeit mildly, revealed a pattern; however, in the case of AlSi10Mg, the plots do not discriminate a single tendency. The first half of the bar charts marginally suggests that inferior stresses are obtained by the absence of a prior powder heating for $t_k = 50$ μm whereas the second half indicates that a powder bed preheating acts as a stress promoter for the same thickness; these patterns are contradictory when $t_k = 200$ μm. This apparent lack of correlation can be justified by the exceptionally high thermal conductivity of the aluminium alloy. The small thermal conductivities of Ti-6Al-4V and 316L in the powder phase and at low temperatures are responsible for the attenuation of thermal gradients when a platform temperature of 500 K is combined with a powder temperature of 700 K, because these alloys could not efficiently absorb the platform temperature before the laser activation; however, AlSi10Mg does not have such constraint when the layer thickness is 50 μm, which causes a cooling prior to the laser heating, thereby raising thermal stresses. In opposition, this behaviour is not sustained for a 200-μm layer, which maintains the stresses lower when compared to its counterpart with an initial powder temperature of 300 K.

It is unambiguous that a high platform heating reduces the generation of stresses. In essence, Figure 6.5 illustrates that the set of process parameters that would optimise the AlSi10Mg-made dog-bone specimen would be $T_{pf} = 700$ K, $T_{pb} = 700$ K and $t_k = 200$ μm.

Discussion. Process parameters have been studied in Chapter 2, Section 2.4, where Equation 2.1 has enabled the comprehension of their variation, albeit neglecting the interaction with the processing material and the preheating. It has already been discussed the reason why it is theoretically expected that smaller thicknesses instigate larger thermal stresses when the same amount of energy is being deposited. On the other hand, the fact that the material is only mechanically activated when the temperature drops below the solidification range has not been mentioned in a stress-inducing matter. As it has been noticed, aluminium exhibits inferior stress values despite of the simulation conditions, which is attributed to the combination of a low solidification temperature (almost 1000 K below the solidification point of Ti-6Al-4V) and a high thermal conductivity.

Apart from having an intermediate solidification temperature between the other two alloys, 316L reaches higher stresses than Ti-6Al-4V, discarding the previous hypothesis as a major cause. A satisfactory explanation may be the impact of the Young's modulus of 316L, the

highest of the three alloys. The Young's modulus is a mechanical property that quantifies the resistance of a material to deformation when a load is applied: the larger it is, the stiffer the material. Figure 6.6 plots the behaviour of 316L for its original Young's modulus and for the value used in the titanium calculations for the same conditions of Figure 6.4. It should be clarified that, as the arrows in the legends indicate, the solid lines represent the thermal fields while the dashed lines represent the von Mises stress fields.

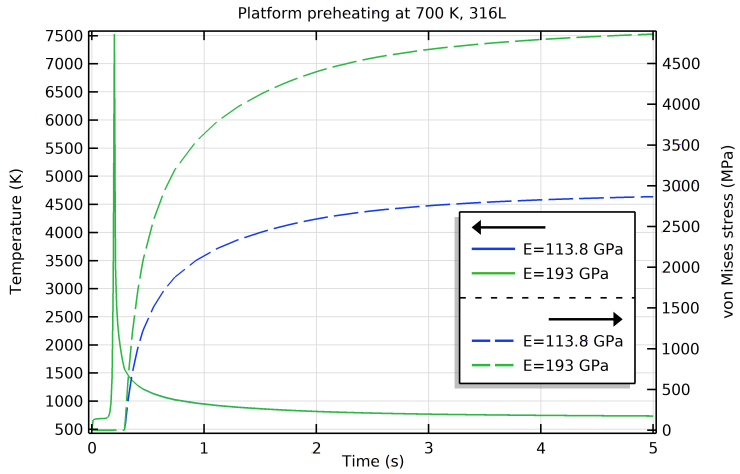

Figure 6.6: The influence of the Young's modulus in the thermal and stress fields of 316L, point C' (0.6, 0).

Effectively, there is a substantial leap between the stress curves represented by the Young's moduli of Ti-6Al-4V, $E = 113.8$ GPa, and 316L, $E = 193$ GPa. This result has further strengthened the conviction that high stresses observed in steel are stemmed by its resistance to be deformed. The same conclusion has been admitted by Vrancken [118]. Furthermore, both temperature curves overlap.

A note of caution must be sounded concerning the selection of the optimised processing conditions. The results obtained hitherto, albeit being in accordance with the literature, should not be adopted carelessly for three main reasons:

- the model concerns a particular specimen with specified dimensions and characteristics that may not be reproducible by other products;
- the model neglects some primarily unimportant aspects regarding the stress field such as fluid dynamics and, consequently, balling and staircase effect, surface roughness and other defects; this is particularly relevant when selecting the dimensions of the layer since it has been studied that a large layer thickness increases the productivity and lower stresses, but, simultaneously, results in a decreased geometrical resolution;

- the response of the model for the three alloys reveals that knowledge obtained for one material cannot be easily transferred to another, because of the tremendous impact of material properties.

Furthermore, in some circumstances, the variation of stress from a higher to a lower powder temperature is barely significant for different layer dimensions; for instance, in Figure 6.4, when $T_{pf} = 700$ K, the stress generated for $t_k = 50$ µm, $T_{pb} = 700$ K are very similar to those generated for $t_k = 200$ µm, $T_{pb} = 300$ K. Thus, opting for a higher layer thickness could be a strategy to reduce the amount of energy required to preheat the powder. In fact, in this case the best option would be to select a lower thickness and a higher powder temperature; however, supposing that would not be feasible, a balance between the benefits (in terms of stress) and drawbacks (in terms of heating energy) must be assessed. Perhaps, it would be more cost-effective to perform a more vigorous post-heat treatment, instead of preheating the powder to a certain degree.

6.2.2 Boundary Patterns

Results. With the purpose of investigating two methods of platform heating, the evolution of properties in the stress concentration point needs to be replaced. Probing the stress in the interface with the platform would benefit the constant heating method in a single-layer simulation due to the reduction of temperature gradients. Therefore, the thermoelastic fields have been computed in the three boundaries of the axisymmetric layer. Interesting patterns have been distinguished for each line, and because these are analogous for the three metallic alloys, the plotted graphs only concern Ti-6Al-4V.

Lower boundary. The lower layer boundary serves as an important heat exchanger as it separates the layer from the base plate. Figure 6.7 compares the disposition of the stress throughout the radius of the layer for initial and constant heating conditions.

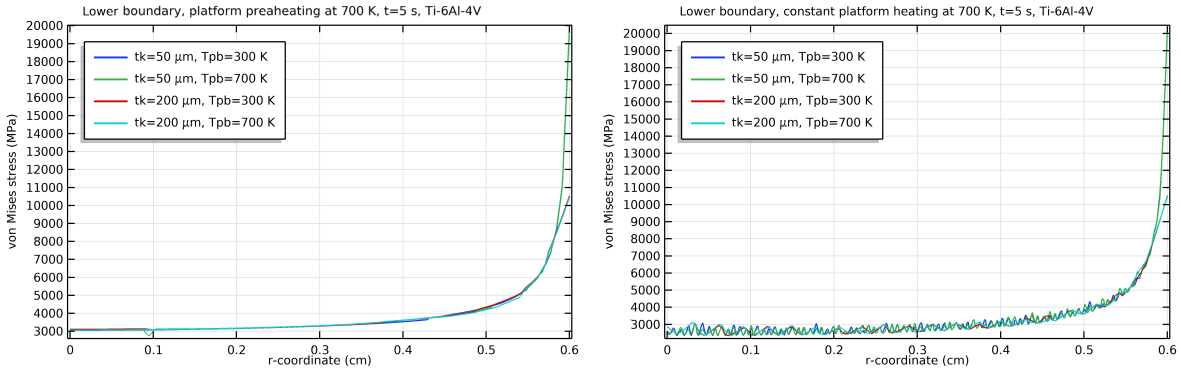

(a) Platform preheating at 700 K. (b) Constant platform heating at 700 K.

Figure 6.7: von Mises stress of the lower boundary of the Ti-6Al-4V alloy.

The most striking result to emerge from the plots is the small noise level detected during constant heating; this is perhaps associated with the endeavour of maintaining the platform at the predefined temperature. Curiously, it is observed that stress tends to increase almost exponentially near the border, which partially corroborates the presence of stress concentration in the point where the first plots have been obtained. Moreover, the stress magnitude is similar for both heating mechanisms.

Lateral boundary. Figure 6.8 compares both heating mechanisms in the lateral boundary along layer thickness.

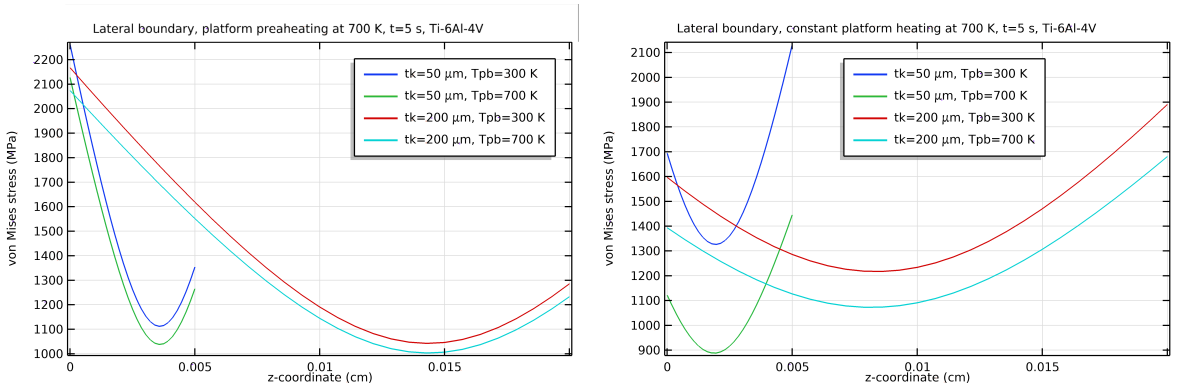

(a) Platform preheating at 700 K. (b) Constant platform heating at 700 K.

Figure 6.8: von Mises stress of the lateral boundary of the Ti-6Al-4V alloy.

Despite of the heating mechanism, Figure 6.8 exhibits parabolic stress patterns along the z-axis, which is also suggested in the work of Mercelis and Kruth [64]; Figure 6.8a corroborates the stress concentration at point C' while, in Figure 6.8b, the maximum values are localised in the upper layer section. A possible explanation for this difference is that the constant heating alleviates the stress induced by the displacement constraint imposed in the bottom

of the part, resulting in higher stresses at the top.

Upper Boundary. The upper boundary is responsible for convective and radiative thermal exchange. The results of the stress field in the mentioned boundary are plotted in Figure 6.9.

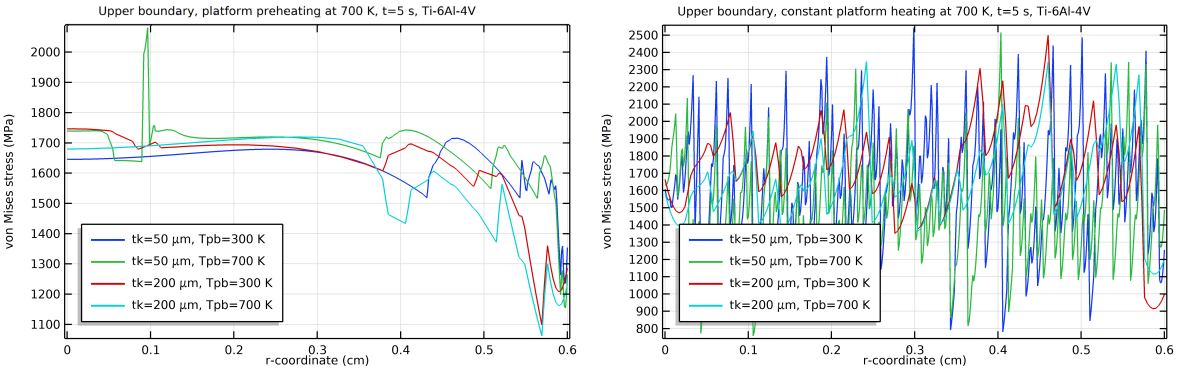

(a) Platform preheating at 700 K. (b) Constant platform heating at 700 K.

Figure 6.9: von Mises stress of the upper boundary of the Ti-6Al-4V alloy.

Noise associated with maintaining the platform temperature can be observed in the upper boundary as well, but not in the vertical boundary, which corroborates the hypothesis relating it to constant heating. In the upper boundary, stress is more pronounced with constant heating method than with preheating conditions.

Peaks observed in Figure 6.9a capture the response of the uneven material solidification caused by the laser scanning.

Discussion. Assuming that the lateral boundary is connected to the upper and lower boundaries at the corners of the rectangle, it may seem unexpected that, for instance, the last values in Figures 6.7a and 6.7b do not coincide with the first values in Figures 6.9a and 6.9b, respectively. However, the lateral boundary is not probed exactly at the border of the layer, because the *Structural Mechanics* node only encompasses both the material to be processed and the platform. If the external border were selected instead of a virtual vertical line completely contained in the layer or platform domains, the program would not be able to compute the stresses; the same applies to the upper boundary.

The large stress identified in Figure 6.7 seemed to be unexpected; however, a closer research based on the experiments of Mercelis and Kruth [64] revealed that the different stress levels in the interface between the platform and the part are partially related to the different stiffnesses of both domains. Another contribution to the increasing of stress is that the dis-

placement constraint imposed between the layer and the platform prevents the layer from shrinking after the solidification.

While it seems clear that different heating methods have an important impact in stress, their repercussions have not yet been established for a complete manufacturing process. Therefore, Section 6.3 assesses the "manufacturing" of a multi-layer specimen for both constant and initial heating conditions for the titanium alloy.

6.3 Multi-layer Results and Discussion

6.3.1 4-layer Processing

Results. Heating methods evidently exert influence on the thermal stress, but their role is not well understood. The manufacturing of a set of four layers has been replicated for both heating approaches. Graphs in Figure 6.10 are plotted in point A, localised in the centre of the first layer, defined by $r = 0$ and $z = 25$ µm.

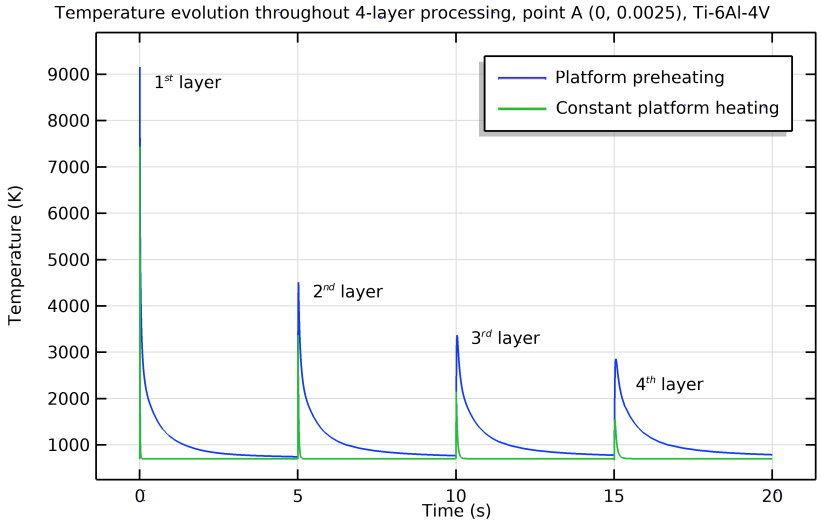

(a) Temperature evolution.

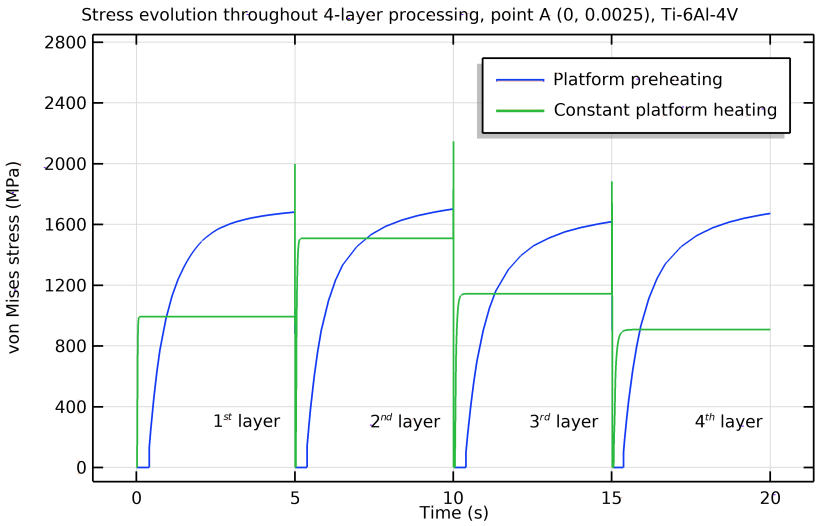

(b) Stress evolution.

Figure 6.10: 4-layer processing for both heating methods.

In Figure 6.10a, it is observed that the preheating of the platform causes the temperature peaks to decrease in the same point over the processing of the four layers, each being processed in 5 seconds (including laser scanning and cooling). The explanation is analogous to the effect of the processing of larger layers, i.e., when a specific amount of energy is deposited in a part with a higher volume, the maximum reached temperature decreases. The preceding layers undergo multiple temperature cycles that alter the temperature distribution, suggesting that layer addition and subsequent scanning are significant to the process. This is in line with the research of Roberts et al. [91]. A constant platform heating has the same declining outcome on the thermal field; however, in this case, heat dissipation occurs in a steeper manner such that the constant temperature that has been imposed on the platform can be restored.

In Figure 6.10b, while preheating reveals a more continuous evolution of stress, constant heating exhibits a constant stress value shortly after the material activation. This can be easily explained by the fact that thermal gradients are predominant before the activation and diminished thereafter. Furthermore, both green and blue curves display a peak with a periodicity of 5 seconds that coincides with the time at which a new layer is added and the laser begins scanning. These peaks correspond to a material reaction to the deposition of energy, which only lasts until the melting temperature is reached. At that point, the stresses are set to zero and only assume non-null values when the material is reactivated.

No significant differences in the stress field can be found at the final instant of each layer (at

5, 10, 15 and 20 s) when the platform is preheated. This repeating behaviour recalls to the material reactivation from a zero-stress state. On the other hand, a constant heating exhibits dubious evolution of stress over time. It can be conceivably hypothesised that the final stress at point A increases from the first to the second layer because they are greatly affected by the laser action; from the third layer, the nearly unchangeable temperature of the platform play a more crucial role on the stresses.

Discussion. While an initial heating would cause the stresses to accumulate during the cooling phase, constant heating maintains the stresses at a constant value until the addition of a new layer. Therefore, preheating is responsible for larger stresses at the final instant of each cycle.

Which one of both platform heating conditions is capable of a more optimised product is not yet wholly understood. In any case, it should be noted that a constant platform heating requires a large energy consumption that, relying on the initial four layers, is probably not worth expending considering the similar results of both approaches. Due to lack of time to carry out further simulations, multi-layer analysis for each condition were not possible. As a commitment, it was decided to study the sets of processing parameters that revealed, in Figure 6.3, a more and less optimised process for Ti-6Al-4V.

6.3.2 Complete Manufacturing

For the sake of simplicity, the sets of parameters that allow for more and less favourable stress profiles are divided in *Group I* and *Group II*, respectively, whose properties are sorted in Table 6.11.

Parameters	**Group I**	**Group II**
Layer thickness (t_k)	200 µm	50 µm
Number of layers (n)	500	2000
Gas temperature (T_a)	300 K	300 K
Powder bed temperature (T_{pb})	700 K	300 K
Platform temperature (T_{pf})	700 K	500 K

Table 6.1: Process parameters of Group I and II.

Results. The multi-layer simulations for both groups were performed accounting for a stop condition for the last iteration. The simulation of Group I was stopped at 9 h and 33.4 min and Group II at 7 h and 55 min. The plots of both are shown in Figure 6.11 with the exaggerated displacement fields.

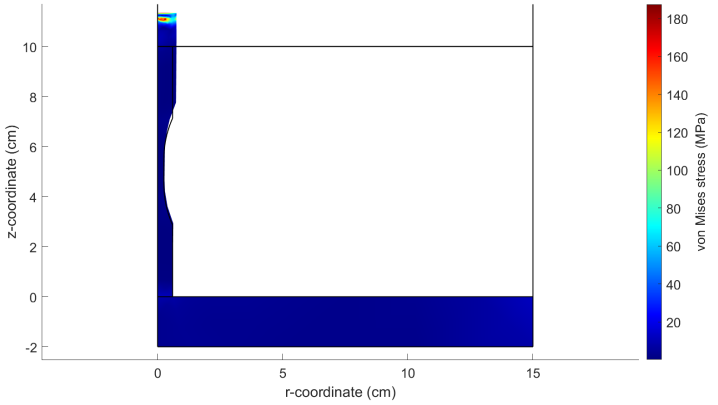

(a) Group I, complete view.

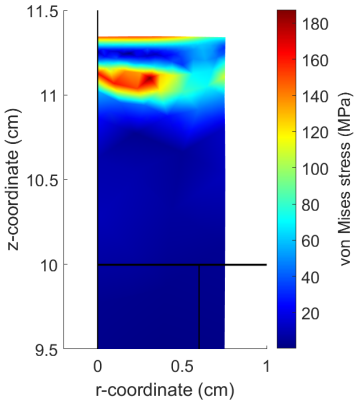

(b) Group I, close-up view.

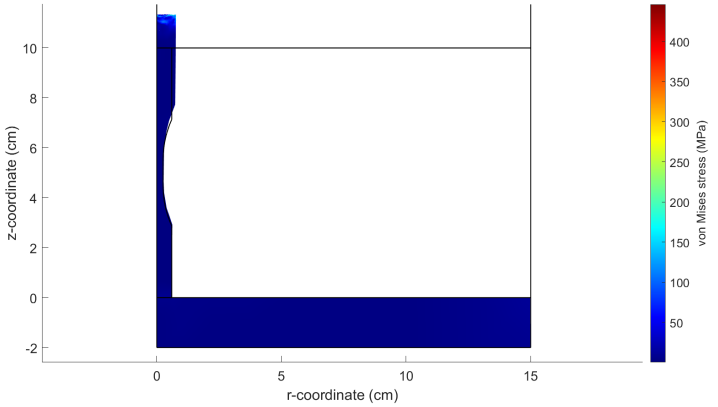

(c) Group II, complete view.

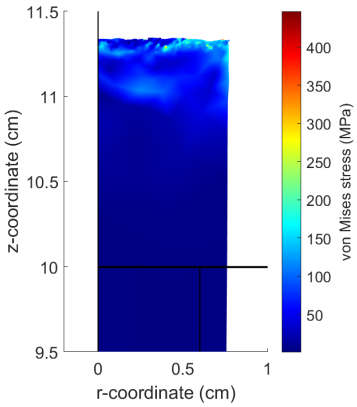

(d) Group II, close-up view.

Figure 6.11: von Mises stress distribution for the manufactured specimen.

Discussion. Both final parts exhibit stress accumulations in the top layer, where the highest peak, 450 MPa, is identified for Group II (Figures 6.11c and 6.11d), which corroborates the single layer analysis. Figures 6.11a and 6.11b, regarding Group I, indicates a region in the top of the dog-bone cylinder where there is a higher stress accumulation of 180 MPa. While these regions are larger (albeit lower in magnitude), there is no indication of apparent surface roughness as opposed to Group II. It can therefore be concluded that both cases have exhibited stress accumulations on the top, which has also been highlighted by some researchers [64] [119]. Additionally, it must be noted that the stress magnitude after n layers is smaller than the stress in a single layer due to the successive in-situ "heat treatments" the part is subject to.

On a negative note, each complete simulation took almost a month to run; this may be associated with the unnecessary fine mesh designed at non-thermally affected zones.

6.4 Hierarchy and Guidelines

The results of this study support the distinct importance of the platform heating; a high platform temperature in all of the three cases has revealed to effectively reduce the thermal stresses. A correct selection of the dimensions of the layer is also crucial, but has revealed a more significant preference in the stainless steel alloy. High thicknesses are worthy of attention, because of its aforementioned negative effects combined with its stress attenuation abilities. Furthermore, a correlation between the role of the powder heating suggests an inconsistent relation for AlSi10Mg, particularly for the combination of $T_{pf} = 500$ K and $T_{pb} = 700$ K. Nevertheless, the Ti-6Al-4V and 316L alloys evidence the expected bias, where the preheating has a mitigation effect in stress.

Chapter 7

Conclusions and Future Work

Accounting for aerospace requirements, additive manufacturing is one of the most attractive solutions for the manufacturing of complex components with lightweight characteristics and outstanding mechanical properties while contributing to a significant mission cost reduction and sustainability. However, the lack of predictability and consistency is a major obstacle for its proliferation either as a main manufacturing or complementary technology. A correct set of process parameters must be identified for each fabricated product under penalty of exacerbating thermal stresses and distortions. Thus, numerical models are fundamental tools to predict the most suitable set of parameters for a specific part, as well as the extent of the defects associated with them.

Thermoelastic single- and multi-layer versions of a Selective Laser Melting model have been developed by means of the coupling between COMSOL Multiphysics and MATLAB with the final aim of determining the manufacturing conditions that would result in the minimisation of stresses for a primary specimen tested under the ADVANSS project, a dog-bone cylinder. Ti-6Al-4V was the focus of most of this research, later extended to stainless steel and aluminium alloys. The model relies on indispensable physical aspects and good flexibility in parameter variation, revealing the numerical capabilities of predicting a stress profile for the three alloys and a myriad of sets of parameters.

The early success of the novel numerical tool appears to be a good indication to the development of a similar, albeit 3-dimensional, model for the optimisation of the Large Lens Mounting.

7.1 Achievements

The potential of developing a two-version model from the outset by means of commercial software for qualitative investigation of the variation of external effects has been tested and verified. The fact that it was designed particularly for parametric evaluation enables users

to easily modify multiple process parameters, material properties and structural or thermal constraints. The introduction of a stop expression to terminate the computation at a specified condition is crucial for encountering a balance between each processing cycle or manufacturing times and the generated stresses, in this case, or any other desired quantity.

Considerable progress has been made with regard to the detailed explanation of the progressive model development, which represents a large portion of this thesis and is usually scarce in the available literature.

The application of the single- and multi-layer tool enabled the identification of a set of conditions that elevate the structural integrity of the dog-bone specimen. Platform preheating and layer thickness exhibited a more consistent influence on stresses, where higher parameter values resulted in more favourable scenarios. Powder bed preheating has a more tenuous or, at least, volatile influence on the results, but a general bias can be distinguished: higher powder temperatures attenuate stresses. The disregard of geometrical and melt-pool defects may be taken into account when selecting the process parameters; for instance, the 200-µm layer could be responsible for inaccuracies in the geometry, although the current results favour this thickness.

The response of material to parameter alteration, in the absence of metallurgical phenomena, can be translated into their properties. As far as the same conditions are assumed, Ti-6Al-4V reaches higher temperature peaks than AlSi10Mg and 316L, essentially due to its higher absorptivity; in addition, its low thermal conductivity implies that the heat transferred to the powder is not easily dissipated causing the temperature to rise. The difficulties of processing aluminium could be indirectly perceivable: a low absorptivity impairs the reception of energy, which creates unsatisfactory conditions for achieving the melting phase. Furthermore, it was confirmed that, owing to its solidification temperature, AlSi10Mg generates lower stresses than the other alloys. In fact, a discrepancy can be observed between the results of aluminium and those of steel and titanium, which react analogously to parametric variation. This is associated with the similar properties shared by Ti-6Al-4V and 316L, but not with AlSi10Mg. For instance, the high thermal conductivity of AlSi10Mg causes an unexpected, albeit understandable, pattern when the platform is preheated at a lower temperature than the powder.

The response of the model has dictated that the transfer of knowledge from one material to another is limited. Nevertheless, it can be stated that, despite weighing differently, high

thermal conductivity, low thermal expansion, low Young's modulus and low solidification temperature lead to the mitigation of thermal stresses. Mechanical properties oversimplification is responsible for artificially increasing the maximum stress, which means that results only deliver qualitative meaning.

The multi-layer studies carried out are insufficient to formulate an assumption regarding the heating methods. The random profiles observed in the curves of constant heating, probed near the 2D-axisymmetric layer boundaries, are associated with the effort of maintaining the prescribed temperature - a pattern not observed for the lateral border.

Most of the results have been confirmed by previous researchers, namely the temperature evolution throughout 4-layer cycles for the platform preheating. Both heating mechanisms show predictable profiles that result in compatible stress evolutions. Finally, the multi-layer simulation displays a higher stress accumulation for Group II.

7.2 Difficulties

The most relevant limitation lies in long simulation times for the multi-layer version, which prevented further studies on the platform heating mechanisms. Presumably, this factor could be reduced by coarsening the mesh away from the HAZ, e.g., in the unprocessed powder layer. Additionally, the modifications the model would require for the study of a new geometry would be substantial; in a positive note, approaches identical to the ones already implemented could be easily introduced to aid modifications.

7.3 Future Work

Having in mind the hurdles encountered during the studies of a 2D geometry, model optimisation could be focused on lowering the simulation time for a multi-layer approach such that a 3D analysis of the Large Lens Mounting can be performed in shorter times. As long as this problem is solved, comparative studies between constant and initial heating methods for a n-layers simulation can be carried out. The thermoelastic model to predict the parametrisation effects on the Large Lens Mounting may include a 120° symmetry and intercepting planes along the build direction to simulate a top layer where a laser beam would be applied.

In an opposite note, the model could be outspread to other scales, in order to capture crucial physics, namely metallurgical and melt-pool phenomena. Unfortunately, a model that offers such complexity is not likely to perform simulations within admissible time spans. Additionally, it would be interesting to perform the same studies considering that all the properties are temperature-dependent.

Lastly, a further investigation on the fatigue behaviour of the additively manufactured Ti-6Al-4V would be interesting, by adopting other mean correction models and different criteria that do not rely on experimental data.

Bibliography

[1] E. Torenbeek and H. Wittenberg, "History of Aviation," *Flight Physics: Essentials of Aeronautical Disciplines and Technology, with Historical Notes*, pp. 1–46, 2009. 1

[2] ICAO, "Future of Aviation," [Accessed on June 8, 2021]. [Online]. Available: www.icao.int/Meetings/FutureOfAviation/Pages/default.aspx 1

[3] L. Zhu, N. Li, and P. Childs, "Light-weighting in Aerospace Component and System Design," *Propulsion and Power Research*, vol. 7, no. 2, pp. 103–119, 2018. 1

[4] M. Potekhin, "Titanium in Spacecraft," *Космическое приборостроение: сборник научных трудов III Всероссийского форума школьников, студентов, аспирантов и молодых ученых с международным участием, г. Томск, 8-10 апреля 2015 г.*, pp. 357–360, 2015. 2, 19

[5] A. K. Singla, M. Banerjee, A. Sharma, J. Singh, A. Bansal, M. K. Gupta, N. Khanna, A. Shahi, and D. K. Goyal, "Selective Laser Melting of Ti-6Al-4V Alloy: Process Parameters, Defects and Post-treatments," *Journal of Manufacturing Processes*, vol. 64, pp. 161–187, 2021. 2, 20, 26, 29, 30

[6] S. Liu and Y. C. Shin, "Additive Manufacturing of Ti-6Al-4V Alloy: a Review," *Materials & Design*, vol. 164, p. 107552, 2019. 2, 20, 29

[7] A. Vafadar, F. Guzzomi, A. Rassau, and K. Hayward, "Advances in Metal Additive Manufacturing: A Review of Common Processes, Industrial Applications, and Current Challenges," *Applied Sciences*, vol. 11, no. 3, p. 1213, 2021. 3, 10, 15, 17, 19, 20, 31

[8] K. Wong and A. Hernandez, "A Review of Additive Manufacturing," *ISRN Mechanical Engineering*, 2012. 3, 14, 15, 20, 21

[9] A. Murat, O. Eroğul, N. Durlu, H. O. Unver, A. Kilic, and H. Kizilok, "Additive Manufacturing of Titanium Alloys," 01 2018. 3, 19, 27

[10] T. D. Ngo, A. Kashani, G. Imbalzano, K. T. Nguyen, and D. Hui, "Additive Manufacturing (3D Printing): A Review of Materials, Methods, Applications and Challenges," *Composites Part B: Engineering*, vol. 143, pp. 172–196, 2018. 3, 14, 15, 16, 17, 18, 19, 20, 29, 30

[11] P. Foteinopoulos, A. Papacharalampopoulos, and P. Stavropoulos, "On Thermal Modeling of Additive Manufacturing Processes," *CIRP Journal of Manufacturing Science and Technology*, vol. 20, pp. 66–83, 2018. 3, 14, 36, 37, 42

[12] M. Brandt, S. J. Sun, M. Leary, S. Feih, J. Elambasseril, and Q. C. Liu, "High-value SLM Aerospace Components: From Design to Manufacture," in *Advanced Materials Research*, vol. 633. Trans Tech Publ, 2013, pp. 135–147. 3, 14, 20, 27, 29, 30, 31

[13] A. Jiménez, P. Bidare, H. Hassanin, F. Tarlochan, S. Dimov, and K. Essa, "Powder-based Laser Hybrid Additive Manufacturing of Metals: A Review," *The International Journal of Advanced Manufacturing Technology*, pp. 1–34, 2021. 3, 9, 12, 13, 14, 15, 16, 19

[14] A. Uriondo, M. Esperon-Miguez, and S. Perinpanayagam, "The Present and Future of Additive Manufacturing in the Aerospace Sector: A Review of Important Aspects," *Proceedings of the Institution of Mechanical Engineers, Part G: Journal of Aerospace Engineering*, vol. 229, no. 11, pp. 2132–2147, 2015. 3, 10, 14, 15, 19, 29, 30, 32, 42

[15] R. Liu, Z. Wang, T. Sparks, F. Liou, and J. Newkirk, "Aerospace Applications of Laser Additive Manufacturing," in *Laser Additive Manufacturing*. Elsevier, 2017, pp. 351–371. 4, 11, 15

[16] L. Bertini, F. Bucchi, F. Frendo, M. Moda, and B. D. Monelli, "Residual Stress Prediction in Selective Laser Melting," *The International Journal of Advanced Manufacturing Technology*, vol. 105, no. 1, pp. 609–636, 2019. 4, 15, 27, 29, 33, 34, 35, 38, 47, 55

[17] B. Barroqueiro, I. Bola, A. Santos, A. Andrade-Campos, R. A. F. Valente, M. Thiel, S. Senese, T. Sedlmaier, and A. Widhammer, "Development of ALM Technology for Space Structures: an Opto-mechanical Case Study," in *16th European Conference on Spacecraft Structures, Materials and Environmental Testing*, 2020. 5

[18] D. L. Bourell, "Perspectives on Additive Manufacturing," *Annual Review of Materials Research*, vol. 46, pp. 1–18, 2016. 9

[19] ASTM, "Additive Manufacturing — General principles — Terminology," 2015, [Accessed on June 16, 2021]. 10

[20] B. Dutta and F. H. S. Froes, "The Additive Manufacturing (AM) of Titanium Alloys," *Metal Powder Report March/April 2017*, vol. 72, no. 2, pp. 97–106, 2017. 10, 13, 19, 32

[21] C. Meier, R. W. Penny, Y. Zou, J. S. Gibbs, and A. J. Hart, "Thermophysical Phenomena in Metal Additive Manufacturing by Selective Laser Melting: Fundamentals, Modeling, Simulation, and Experimentation," *Annual Review of Heat Transfer*, vol. 20, 2017. 10, 16, 27, 29, 30, 43, 56, 58

[22] S. Kumar, "Selective Laser Sintering/Melting," in *Comprehensive Materials Processing*, S. Hashmi, G. F. Batalha, C. J. Van Tyne, and B. Yilbas, Eds. Oxford: Elsevier, 2014, pp. 93–134. 10

[23] J. Romano, L. Ladani, and M. Sadowski, "Thermal Modeling of Laser Based Additive Manufacturing Processes within Common Materials," *Procedia Manufacturing*, vol. 1, pp. 238–250, 2015. 11, 71, 119, 120

[24] K. J. Buschow, R. W. Cahn, M. C. Flemings, B. Ilschner, E. J. Kramer, and S. Mahajan, "Encyclopedia of Materials," *Science and Technology*, vol. 1, no. 11, 2001. 11

[25] M. Yakout, M. Elbestawi, and S. C. Veldhuis, "A Review of Metal Additive Manufacturing Technologies," in *Solid State Phenomena*, vol. 278. Trans Tech Publ, 2018, pp. 1–14. 11, 14, 16, 21, 22, 27

[26] T. Saraçyakupoğlu, "Usage of Additive Manufacturing and Topology Optimization Process for Weight Reduction Studies in the Aviation Industry," *Advances in Science, Technology and Engineering Systems Journal*, vol. 6, no. 2, pp. 815–820, 2021. 12

[27] H. Helms and U. Lambrecht, "The Potential Contribution of Light-weighting to Reduce Transport Energy Consumption," *Int. J. Life Cycle Assess*, vol. 12, no. 1, pp. 58–64, 2007. 12, 13

[28] J. Peels, "Design Guidelines for Direct Metal Laser Sintering, Selective Laser Melting, Laser Powder Bed Fusion," 2019, [Accessed on September 11, 2021]. [Online]. Available: https://3dprint.com/237866/design-guidelines-for-direct-metal-laser-sintering-selective-laser-melting-laser-powder-bed-fusion/ 13

[29] S. Singamneni, L. Yifan, A. Hewitt, R. Chalk, W. Thomas, and D. Jordison, "Additive Manufacturing for the Aircraft Industry: A Review," *J. Aeronaut. Aerosp. Eng*, vol. 8, no. 214, p. 2, 2019. 13, 15, 16, 22

[30] C. G. Ferro, S. Varetti, F. Vitti, P. Maggiore, M. Lombardi, S. Biamino, D. Manfredi, and F. Calignano, "A Robust Multifunctional Sandwich Panel Design with Trabecular Structures by the Use of Additive Manufacturing Technology for a New De-Icing System," *Technologies*, vol. 5, no. 2, p. 35, 2017. 13

[31] N. T. Aboulkhair, M. Simonelli, L. Parry, I. Ashcroft, C. Tuck, and R. Hague, "3d Printing of Aluminium Alloys: Additive Manufacturing of Aluminium Alloys using Selective Laser Melting," *Progress in materials science*, vol. 106, p. 100578, 2019. 14, 18

[32] M. Mazur, M. Leary, M. McMillan, S. Sun, D. Shidid, and M. Brandt, "Mechanical Properties of Ti-6Al-4V and AlSi12Mg Lattice Structures Manufactured by Selective Laser Melting (SLM)," in *Laser Additive Manufacturing*. Elsevier, 2017, pp. 119–161. 14, 27, 29

[33] ISO. (2021) ISO/TC 261: Additive Manufacturing. [Accessed on August 10, 2021]. [Online]. Available: https://www.iso.org/committee/629086.html 15

[34] ASTM. (2021) Additive manufacturing overview. [Accessed on August 10, 2021]. [Online]. Available: https://www.astm.org/COMMITTEE/F42.htm 15

[35] V. V. Popov, M. L. Grilli, A. Koptyug, L. Jaworska, A. Katz-Demyanetz, D. Klobčar, S. Balos, B. O. Postolnyi, and S. Goel, "Powder Bed Fusion Additive Manufacturing Using Critical Raw Materials: A Review," *Materials*, vol. 14, no. 4, p. 909, 2021. 15, 16, 18, 20

[36] D. Bourell, J. P. Kruth, M. Leu, G. Levy, D. Rosen, A. M. Beese, and A. Clare, "Materials for Additive Manufacturing," *CIRP Annals*, vol. 66, no. 2, pp. 659–681, 2017. 16, 20, 28, 29, 30, 55

[37] B. Nie, L. Yang, H. Huang, S. Bai, P. Wan, and J. Liu, "Femtosecond Laser Additive Manufacturing of Iron and Tungsten Parts," *Applied Physics A*, vol. 119, no. 3, pp. 1075–1080, 2015. 17

[38] "Materials in Additive Manufacturing," 2021, [Accessed on September 12, 2021]. [Online]. Available: https://www.linkedin.com/feed/update/urn:li:activity:6842024041906348032/ 17

[39] "3D Metal Printing: Alloys and Powder Types and Specs," 2019, [Accessed on September 12, 2021]. [Online]. Available: https://www.belmontmetals.com/alloys-and-powder-specs-for-3d-printing/ 17

[40] "Available Materials for Metal Additive Manufacturing: Characteristics & Applications," 2015, [Accessed on September 12, 2021]. [Online]. Available: https://www.farinia.com/blog/available-materials-metal-additive-manufacturing-characteristics-applications 17

[41] "Manufatura Aditiva: Pó e Parâmetro," [Accessed on September 12, 2021]. [Online]. Available: https://www.trumpf.com/pt_PT/produtos/maquinas-sistemas/sistemas-de-manufatura-aditiva/po-truservices/ 17

[42] P. Bajaj, A. Hariharan, A. Kini, P. Kürnsteiner, D. Raabe, and E. A. Jägle, "Steels in Additive Manufacturing: a Review of their Microstructure and Properties," *Materials Science and Engineering: A*, vol. 772, p. 138633, 2020. 17, 18

[43] N. Haghdadi, M. Laleh, M. Moyle, and S. Primig, "Additive Manufacturing of Steels: a Review of Achievements and Challenges," *Journal of Materials Science*, pp. 1–44, 2020. 17, 32

[44] A. Gloria, R. Montanari, M. Richetta, and A. Varone, "Alloys for Aeronautic Applications: State of the Art and Perspectives," *Metals*, vol. 9, no. 6, p. 662, 2019. 17, 19

[45] P. Ponnusamy, R. A. Rahman Rashid, S. H. Masood, D. Ruan, and S. Palanisamy, "Mechanical properties of SLM-printed Aluminium alloys: A Review," *Materials*, vol. 13, no. 19, p. 4301, 2020. 18

[46] B. Blakey-Milner, P. Gradl, G. Snedden, M. Brooks, J. Pitot, E. Lopez, M. Leary, F. Berto, and A. du Plessis, "Metal Additive Manufacturing in Aerospace: a Review," *Materials & Design*, p. 110008, 2021. 19, 24, 25

[47] Q. Jia and D. Gu, "Selective Laser Melting Additive Manufacturing of Inconel 718 Superalloy Parts: Densification, Microstructure and Properties," *Journal of Alloys and Compounds*, vol. 585, pp. 713–721, 2014. 19

[48] B. Graybill, M. Li, D. Malawey, C. Ma, J.-M. Alvarado-Orozco, and E. Martinez-Franco, "Additive Manufacturing of Nickel-based Superalloys," in *International Manufacturing Science and Engineering Conference*, vol. 51357. American Society of Mechanical Engineers, 2018, p. V001T01A015. 19

[49] A. Kolomiets, Y. Grobman, V. Popov Jr, E. Strokin, G. Senchikhin, and E. Tarazi, "The Titanium 3D-printed Flute: New Prospects of Additive Manufacturing for Musical

Wind Instruments Design," *Journal of New Music Research*, vol. 50, no. 1, pp. 1–17, 2021. 20

[50] M. T. Mohammed, V. Semelov, and A. Sotov, "SLM-built Titanium Materials: Great Potential of Developing Microstructure and Properties for Biomedical Applications: A Review," *Materials Research Express*, vol. 6, no. 12, p. 122006, 2020. 21, 26

[51] N. Noor, A. Shapira, R. Edri, I. Gal, L. Wertheim, and T. Dvir, "3D Printing of Personalized Thick and Perfusable Cardiac Patches and Hearts," *Advanced Science*, vol. 6, no. 11, p. 1900344, 2019. 21

[52] S. Green, N. Holmstock, L. Vervecken, and G.-J. Paulus, "Optimised Thermal Management in Semiconductor Fabrication using Al-enabled Generative Design and Additive Manufacturing," *Metal Additive Manufacturing*, vol. 7, no. 2, pp. 123–135, 2021. 21

[53] EOS. (2021) Using Additive Manufacturing for Conformal Cooling. [Accessed on August 12, 2021]. [Online]. Available: https://www.eos.info/en/3d-printing-examples-applications/all-3d-printing-applications/innomia-automotive-3d-printed-cooling-channels 22

[54] I. C. Ltd, "Sauber's F1 Technology used in Production of Additively Manufactured Classic Car Parts," *Metal Additive Manufacturing*, vol. 7, no. 2, pp. 47–48, 2021. 23

[55] B. A. S.A.S., "World Premiere: Brake Caliper from 3-D Printer," 2018, [Accessed on September 14, 2021]. [Online]. Available: https://www.bugatti.com/media/news/2018/world-premiere-brake-caliper-from-3-d-printer/ 23

[56] G. E. Additive, "GE Additive: GE9X," 2020. [Online]. Available: https://www.ge.com/additive/sites/default/files/2020-08/GE9X%20Additive%20parts.pdf 24

[57] N. Titanium, "Norsk Titanium to Deliver the World's First FAA-Approved, 3D-Printed, Structural Titanium Components to Boeing," 2017, [Accessed on September 16, 2021]. [Online]. Available: https://www.norsktitanium.com/media/press/norsk-titanium-to-deliver-the-worlds-first-faa-approved-3d-printed-structural-titanium-components-to-boeing 24

[58] N. Aeronautics and S. Administration, "Mars 2020/Perseverance," 2020. 25

[59] C. Additive, "Case Study: PIXL Mars Rover," 2021. 25

[60] G. Aerospace, "GKN Aerospace Delivers Revolutionary Ariane 6 Nozzle to Airbus Safran Lauchers," 2017, [Accessed on September 16, 2021]. [Online]. Available: https://www.gknaerospace.com/en/newsroom/news-releases/2017/gkn-delivers-revolutionary-ariane-6-nozzle-to-airbus-safran-launchers/ 25

[61] ArianeGroup, "Ariane 6," 2019, [Accessed on September 16, 2021]. [Online]. Available: https://www.arianespace.com/vehicle/ariane-6/ 25

[62] E. Mirkoohi, D. E. Seivers, H. Garmestani, and S. Y. Liang, "Heat Source Modeling in Selective Laser Melting," *Materials*, vol. 12, no. 13, p. 2052, 2019. 26, 29, 36, 42, 45, 119

[63] A. Razavykia, E. Brusa, C. Delprete, and R. Yavari, "An Overview of Additive Manufacturing Technologies: A Review to Technical Synthesis in Numerical Study of Selective Laser Melting," *Materials*, vol. 13, no. 17, p. 3895, 2020. 27, 45

[64] P. Mercelis and J.-P. Kruth, "Residual Stresses in Selective Laser Sintering and Selective Laser Melting," *Rapid prototyping journal*, 2006. 28, 94, 95, 99

[65] K. Carpenter and A. Tabei, "On Residual Stress Development, Prevention, and Compensation in Metal Additive Manufacturing," *Materials*, vol. 13, no. 2, p. 255, 2020. 29, 46

[66] A. Wiberg, J. Persson, and J. Ölvander, "Design for Additive Manufacturing: A Review of Available Design Methods and Software," *Rapid Prototyping Journal*, 2019. 31

[67] L. Mugwagwa, D. Dimitrov, S. Matope, and I. Yadroitsev, "Influence of Process Parameters on Residual Stress Related Distortions in Selective Laser Melting," *Procedia Manufacturing*, vol. 21, pp. 92–99, 2018. 31

[68] L. N. Carter, C. Martin, P. J. Withers, and M. M. Attallah, "The Influence of the Laser Scan Strategy on Grain Structure and Cracking Behaviour in SLM Powder-bed Fabricated Nickel Superalloy," *Journal of Alloys and Compounds*, vol. 615, pp. 338–347, 2014. 32

[69] H. Ali, H. Ghadbeigi, and K. Mumtaz, "Effect of Scanning Strategies on Residual Stress and Mechanical Properties of Selective Laser Melted Ti6Al4V," *Materials Science and Engineering: A*, vol. 712, pp. 175–187, 2018. 32

[70] W. Liu, K. M. Saleheen, Z. Tang, H. Wang, G. Al-Hammadi, A. Abdelrahman, Z. Yongxin, S.-G. Hua, and F. Wang, "Review on Scanning Pattern Evaluation in Laser-based Additive Manufacturing," *Optical Engineering*, vol. 60, no. 7, p. 070901, 2021. 32

[71] M. Malỳ, C. Höller, M. Skalon, B. Meier, D. Koutnỳ, R. Pichler, C. Sommitsch, and D. Paloušek, "Effect of Process Parameters and High-temperature Preheating on Residual Stress and Relative Density of Ti-6Al-4V Processed by Selective Laser Melting," *Materials*, vol. 12, no. 6, p. 930, 2019. 32

[72] M. Sun, *Physical Modeling of the Selective Laser Sintering Process*. University of Texas at Austin, 1991. 32

[73] S. Kolossov, E. Boillat, R. Glardon, P. Fischer, and M. Locher, "3D FE Simulation for Temperature Evolution in the Selective Laser Sintering Process," *International Journal of Machine Tools and Manufacture*, vol. 44, no. 2, pp. 117–123, 2004. 33

[74] M. Chiumenti, E. Neiva, E. Salsi, M. Cervera, S. Badia, J. Moya, Z. Chen, C. Lee, and C. Davies, "Numerical Modelling and Experimental Validation in Selective Laser Melting," *Additive Manufacturing*, vol. 18, pp. 171–185, 2017. 33, 35, 38, 70, 119

[75] F. Chen and W. Yan, "High-fidelity Modelling of Thermal Stress for Additive Manufacturing by Linking Thermal-fluid and Mechanical Models," *Materials & Design*, vol. 196, p. 109185, 2020. 33, 59, 119

[76] A. Boschetto, L. Bottini, L. Macera, and F. Veniali, "Post-Processing of Complex SLM Parts by Barrel Finishing," *Applied Sciences*, vol. 10, no. 4, 2020. 33

[77] E. Brusa, R. Sesana, and E. Ossola, "Numerical Modeling and Testing of Mechanical Behavior of AM Titanium Alloy Bracket for Aerospace Applications," *Procedia Structural Integrity*, vol. 5, pp. 753–760, 2017. 33

[78] Z. Xiao, C. Chen, H. Zhu, Z. Hu, B. Nagarajan, L. Guo, and X. Zeng, "Study of Residual Stress in Selective Laser Melting of Ti6Al4V," *Materials & Design*, vol. 193, p. 108846, 2020. 33, 38

[79] K. Bartsch, F. Lange, M. Gralow, and C. Emmelmann, "Novel Approach to Optimized Support Structures in Laser Beam Melting by Combining Process Simulation with Topology Optimization," *Journal of Laser Applications*, vol. 31, no. 2, p. 022302, 2019. 33

[80] P. Nie, O. Ojo, and Z. Li, "Numerical Modeling of Microstructure Evolution during Laser Additive Manufacturing of a Nickel-based Superalloy," *Acta Materialia*, vol. 77, pp. 85–95, 2014. 33

[81] S. D. Proell, W. A. Wall, and C. Meier, "On Phase Change and Latent Heat Models in Metal Additive Manufacturing Process Simulation," *Advanced Modeling and Simulation in Engineering Sciences*, vol. 7, pp. 1–32, 2020. 33, 36, 70

[82] H. Liu, *Numerical Analysis of Thermal Stress and Deformation in Multi-layer Laser Metal Deposition Process*. Missouri University of Science and Technology, 2014. 34, 46

[83] K. Bartsch, I. Herzog, C. Emmelmann, and F. Lange, "A Novel Approach to Support Structures Optimized for Heat Dissipation in SLM by Combining Process Simulation with Topology Optimization," 07 2019. 34

[84] J. A. Goldak and M. Akhlaghi, *Computational Welding Mechanics*. Springer Science & Business Media, 2005. 34

[85] E. L. Papazoglou, N. E. Karkalos, P. Karmiris-Obratański, and A. P. Markopoulos, "On the Modeling and Simulation of slm and sls for Metal and Polymer Powders: a Review," *Archives of Computational Methods in Engineering*, pp. 1–33, 2021. 35, 38, 45

[86] A. Gusarov and J.-P. Kruth, "Modelling of Radiation Transfer in Metallic Powders at Laser Treatment," *International Journal of Heat and Mass Transfer*, vol. 48, no. 16, pp. 3423–3434, 2005. 35

[87] H. S. Carslaw and J. C. Jaeger, "Conduction of Heat in Solids," Clarendon Press, Tech. Rep., 1959. 35

[88] J. Ning, D. E. Sievers, H. Garmestani, and S. Y. Liang, "Analytical Modeling of In-process Temperature in Powder Bed Additive Manufacturing Considering Laser Power Absorption, Latent Heat, Scanning Strategy, and Powder Packing," *Materials*, vol. 12, no. 5, p. 808, 2019. 35

[89] H. Cline and T. Anthony, "Heat Treating and Melting Material with a Scanning Laser or Electron Beam," *Journal of Applied Physics*, vol. 48, no. 9, pp. 3895–3900, 1977. 35

[90] D. Pitassi, E. Savoia, V. Fontanari, A. Molinari, V. Luchin, G. Zappini, and M. Benedetti, "Finite Element Thermal Analysis of Metal Parts Additively Manufactured via Selective Laser Melting," *Finite Element Method—Simulation, Numerical Analysis and Solution Techniques*, pp. 123–154, 2018. 36

[91] I. A. Roberts, C. Wang, R. Esterlein, M. Stanford, and D. Mynors, "A Three-dimensional Finite Element Analysis of the Temperature Field During Laser Melting of Metal Powders in Additive Layer Manufacturing," *International Journal of Machine Tools and Manufacture*, vol. 49, no. 12-13, pp. 916–923, 2009. 36, 45, 64, 97

[92] E. R. Denlinger, J. Irwin, and P. Michaleris, "Thermomechanical Modeling of Additive Manufacturing Large Parts," *Journal of Manufacturing Science and Engineering*, vol. 136, no. 6, 2014. 36, 119

[93] ANSYS, "ANSYS Advanced Analysis Guide," 2005, [Accessed on September 16, 2021]. 36

[94] M. Chiumenti, X. Lin, M. Cervera, W. Lei, Y. Zheng, and W. Huang, "Numerical Simulation and Experimental Calibration of Additive Manufacturing by Blown Powder Technology. Part I: Thermal Analysis," *Rapid Prototyping Journal*, 2017. 36, 42

[95] M. Faden, A. König-Haagen, and D. Brüggemann, "An Optimum Enthalpy Approach for Melting and Solidification with Volume Change," *Energies*, vol. 12, no. 5, p. 868, 2019. 36

[96] J. Ning, D. E. Sievers, H. Garmestani, and S. Y. Liang, "Analytical Thermal Modeling of Metal Additive Manufacturing by Heat Sink Solution," *Materials*, vol. 12, no. 16, p. 2568, 2019. 36, 42, 59

[97] N. Hodge, R. Ferencz, and J. Solberg, "Implementation of a Thermomechanical Model for the Simulation of Selective Laser Melting," *Computational Mechanics*, vol. 54, no. 1, pp. 33–51, 2014. 36, 42

[98] P. Conti, F. Cianetti, and P. Pilerci, "Parametric Finite Elements Model of SLM Additive Manufacturing Process," *Procedia Structural Integrity*, vol. 8, pp. 410–421, 2018. 36, 37

[99] S. Yagi and D. Kunii, "Studies on Effective Thermal Conductivities in Packed Beds," *AIChE Journal*, vol. 3, no. 3, pp. 373–381, 1957. 37, 70

[100] A. Foroozmehr, M. Badrossamay, E. Foroozmehr, and S. Golabi, "Finite Element Simulation of Selective Laser Melting Process Considering Optical Penetration Depth of Laser in Powder Bed," *Materials & Design*, vol. 89, pp. 255–263, 2016. 37

[101] B. Schoinochoritis, D. Chantzis, and K. Salonitis, "Simulation of Metallic Powder Bed Additive Manufacturing Processes with the Finite Element Method: A Critical Review," *Proceedings of the Institution of Mechanical Engineers, Part B: Journal of Engineering Manufacture*, vol. 231, 01 2015. 37

[102] S. S. Sih and J. W. Barlow, "Emissivity of Powder Beds," in *1995 International Solid Freeform Fabrication Symposium*, 1995. 38, 74

[103] K. Zeng, D. Pal, N. Patil, and B. Stucker, "A New Dynamic Mesh Method Applied to the Simulation of Selective Laser Melting," *24th International SFF Symposium - An Additive Manufacturing Conference, SFF 2013*, pp. 549–559, 01 2013. 39, 42, 45

[104] X. Song, S. Feih, W. Zhai, C.-N. Sun, F. Li, R. Maiti, J. Wei, Y. Yang, V. Oancea, L. R. Brandt *et al.*, "Advances in Additive Manufacturing Process Simulation: Residual Stresses and Distortion Predictions in Complex Metallic Components," *Materials & Design*, vol. 193, p. 108779, 2020. 42, 87

[105] COMSOL, "Heat Transfer Module: User's Guide," 2018. 43, 44, 47, 51

[106] B. M. Marques, C. M. Andrade, D. M. Neto, M. C. Oliveira, J. L. Alves, and L. F. Menezes, "Numerical Analysis of Residual Stresses in Parts Produced by Selective Laser Melting Process," *Procedia Manufacturing*, vol. 47, pp. 1170–1177, 2020. 45, 119

[107] "Lecture notes in Structural Mechanics," [Accessed on September 8, 2021]. [Online]. Available: http://web.mit.edu/16.20/homepage/3_Constitutive/Constitutive.html 46

[108] Walter Frei. (2016) Thermal Modeling of Phase-Change Materials with Hysteresis. [Accessed on March 16, 2021]. [Online]. Available: https://www.comsol.com/blogs/thermal-modeling-of-phase-change-materials-with-hysteresis/ 55

[109] Z. Fan and F. Liou, "Numerical Modeling of the Additive Manufacturing (AM) Processes of Titanium Alloy," *Titanium alloys–towards achieving enhanced properties for diversified applications*, pp. 3–28, 2012. 57, 119

[110] M. Boivineau, C. Cagran, D. Doytier, V. Eyraud, M.-H. Nadal, B. Wilthan, and G. Pottlacher, "Thermophysical Properties of Solid and Liquid Ti-6Al-4V (TA6V) Alloy," *International journal of thermophysics*, vol. 27, no. 2, pp. 507–529, 2006. 57

[111] Mats Danielsson. (2018) How to Activate Material in Simulations of Manufacturing Processes. [Accessed on April 23, 2021]. [Online]. Available: https://www.comsol.com/blogs/how-to-activate-material-in-simulations-of-manufacturing-processes 58

[112] P. Hagqvist, F. Sikström, and A.-K. Christiansson, "Emissivity Estimation for High Temperature Radiation Pyrometry on Ti-6Al-4V," *Measurement*, vol. 46, no. 2, pp. 871–880, 2013. 59, 119

[113] COMSOL, "COMSOL Multiphysics: Reference Manual," 2019. 64

[114] A. Schmon, K. Aziz, and G. Pottlacher, "Density of Liquid Ti-6Al-4V," in *EPJ Web of Conferences*, vol. 151. EDP Sciences, 2017, p. 04003. 70, 119

[115] S. S. Xue and J. W. Barlow, "Models for the Prediction of the Thermal Conductivities of Powders," in *1991 International Solid Freeform Fabrication Symposium*, 1991. 70, 119

[116] K. C. Mills, "Ti: Ti-6 Al-4 V (IMI 318)," in *Recommended Values of Thermophysical Properties for Selected Commercial Alloys*, ser. Woodhead Publishing Series in Metals and Surface Engineering, K. C. Mills, Ed. Woodhead Publishing, 2002, pp. 211–217. 76

[117] R. Patrício, "Relatório Técnico Final: ADVANSS - Advanced Additive Manufacturing for High-Recurrence Satellites," 2020. 82

[118] B. Vrancken, "Study of residual stresses in selective laser melting," 2016. 92, 120

[119] Ganeriwala, Rishi Kumar, "Multiphysics Modeling of Selective Laser Sintering/Melting," Ph.D. dissertation, University of California, Berkeley, 2015. 99

[120] Matweb. Material Property Data: Titanium Ti-6Al-4V ELI (Grade 23). [Accessed on May 27, 2021]. [Online]. Available: http://www.matweb.com/search/DataSheet.aspx?MatGUID=c9a1da836836434d8caa78c23dfeb10f 119

[121] P. E. Carrion, N. Shamsaei, S. Daniewicz, and R. Moser, "Fatigue Behavior of Ti-6Al-4V ELI Including Mean Stress Effects," *International Journal of Fatigue*, vol. 99, pp. 87–100, 2017. 119

[122] Matweb. Material Property Data: Argon, Ar. [Accessed on March 16, 2021]. [Online]. Available: http://www.matweb.com/search/DataSheet.aspx?MatGUID=c9a1da836836434d8caa78c23dfeb10f 119

[123] Engineering ToolBox. (2003) Ratios of Specific Heat of Gases. [Accessed on March 16, 2021]. [Online]. Available: https://www.engineeringtoolbox.com/specific-heat-ratio-d_608.html 119

[124] Matweb. (2021) Material property data: Aisi type 316l stainless steel. [Accessed on August 13, 2021]. [Online]. Available: http://www.matweb.com/search/DataSheet.aspx?MatGUID=1336be6d0c594b55afb5ca8bf1f3e042 120

[125] "AISI 316L (S31603) Stainless Steel," [Accessed on August 13, 2021]. [Online]. Available: https://www.makeitfrom.com/material-properties/AISI-316L-S31603-Stainless-Steel 120

[126] G. Mohr, S. Nowakowski, S. J. Altenburg, C. Maierhofer, and K. Hilgenberg, "Experimental Determination of the Emissivity of Powder Layers and Bulk Material in Laser Powder Bed Fusion Using Infrared Thermography and Thermocouples," *Metals*, vol. 10, no. 11, p. 1546, 2020. 120

[127] L. Chen, H. Li, S. Liu, S. Shen, T. Zhang, Y. Huang, G. Zhang, Y. Zhang, B. He, and C. Yang, "Simulation of Surface Deformation Control during Selective Laser Melting of AlSi10Mg Powder using an External Magnetic Field," *AIP Advances*, vol. 9, no. 4, p. 045012, 2019. 120

[128] M. Leitner, T. Leitner, A. Schmon, K. Aziz, and G. Pottlacher, "Thermophysical Properties of Liquid Aluminum," *Metall. Mater. Trans. A*, vol. 48, no. 6, pp. 3036–3045, 2017. 120

[129] M. Tang, "Inclusions, Porosity, and Fatigue of AlSi10Mg Parts Produced by Selective Laser Melting," Ph.D. dissertation, Carnegie Mellon University, 05 2017. 120

[130] L. Hitzler, C. Janousch, J. Schanz, M. Merkel, B. Heine, F. Mack, W. Hall, and A. Öchsner, "Direction and Location Dependency of Selective Laser Melted AlSi10Mg Specimens," *Journal of Materials Processing Technology*, vol. 243, pp. 48–61, 2017. 120

Appendix A

Material Properties

Property	Powder	Solid	Liquid	Unit	Ref.
T_{pc}	-	1878	1928	K	[62]
L_{pc}	-	286	286	J g^{-1}	[62]
ρ	3100	4430	3800	kg m^{-3}	[92] [114]
k	0.33	6 [1]	33.4 [1]	W m^{-1} K^{-1}	[115]
C_{p_0}	688.5	688.5	688.5	J kg^{-1} K^{-1}	[109]
ε	0.35	0.35	0.35	1	[112] [106]
η	0.73	0.73	0.73	1	[23]
α_T	-	9×10^{-6}	-	K^{-1}	[75]
E	-	113.8	-	GPa	[120]
ν	-	0.34	-	1	[92] [106]
σ_y	-	992	-	MPa	[121]

Table A.1: Properties of Ti-6Al-4V.

Property	Value	Unit	Ref.
ρ	1.6	kg m^{-3}	[122]
k	0.016	W m^{-1} K^{-1}	[74]
C_p	520	J kg^{-1} K^{-1}	[122]
γ	1.7	1	[123]

Table A.2: Properties of argon.

Property	Value	Unit
ρ	7850	kg m^{-3}
k	44.5	W m^{-1} K^{-1}
C_p	475	J kg^{-1} K^{-1}
α_T	12.3×10^{-6}	K^{-1}
E	205	GPa
ν	0.28	1

Table A.3: Properties of the AISI 4340-made platform.

[1] replaced by Equation 5.5.

Property	Powder	Solid	Liquid	Unit	Ref.
T_{pc}	-	1648	1673	K	[124]
L_{pc}	-	290	290	J g^{-1}	[125]
ρ	5600.5	8000	7500	kg m^{-3}	[124]
k	0.6	24.8 [2]	24.8 [2]	W m^{-1} K^{-1}	COMSOL Library
C_{p_0}	747	747	747	J kg^{-1} K^{-1}	COMSOL Library
ε	0.25	0.25	0.25	1	[126]
η	0.64	0.64	0.64	1	[23]
α_T	-	16×10^{-6}	-	K^{-1}	COMSOL Library
E	-	193	-	GPa	[124]
ν	-	0.28	-	1	[118]

Table A.4: Properties of 316L.

Property	Powder	Solid	Liquid	Unit	Ref.
T_{pc}	-	831	867	K	[127]
L_{pc}	-	423	423	J g^{-1}	[127]
ρ	1869.5	2670	2390	kg m^{-3}	[127] [128]
k	1.32	110	170	W m^{-1} K^{-1}	[127]
C_{p_0}	1155	1155	1155	J kg^{-1} K^{-1}	[127]
ε	0.36	0.36	0.36	1	[127]
η	0.32	0.32	0.32	1	[129]
α_T	-	23.9×10^{-6}	-	K^{-1}	[127]
E	-	70	-	GPa	[130]
ν	-	0.33	-	1	[130]

Table A.5: Properties of AlSi10Mg.

[2] temperature-dependent function given by Equation 6.1.

Appendix B

MATLAB Code

B.1 Cylinder

```
function out = model
tic
import com.comsol.model.*
import com.comsol.model.util.*
model = ModelUtil.create('Model');

%Iterations and subplots
iterations = 1000;
sp_1 = 2;
sp_2 = 5;
%Parameters
timestep = 0.01;
timelast = 50; %[s]
path = "Files";
tk = 0.01; %[cm]
rc = 1; %[cm]
hcam = 80; %[cm]
rcam = 40; %[cm]
model.param.set('t_step', num2str(timestep), 'Time step');
model.param.set('t_last', num2str(timelast), 'Last time');
model.param.set('tk', num2str(tk), 'Layer thickness');
model.param.set('rc', num2str(rc), 'Cylinder radius');
model.param.set('hcam', num2str(hcam), 'Chamber height');
model.param.set('rcam', num2str(rcam), 'Chamber radius');
model.param.set('T_a', '300[K]', 'Initial temperature');
model.param.set('SorL_init', '1', 'Initial state');
```

```
model.param.set('vel', '200[mm/s]', 'Velocity magnitude');
model.param.set('P', '300[W]', 'Laser power');
model.param.set('factor', '1', 'Absorption factor');
model.param.set('R_g', '0.01[cm]', 'Standard deviation');
%Argon properties
model.param.set('rho_a', '0.0016[g/cm^3]', 'Density');
model.param.set('Cp_a', '520[J/kg/K]', 'Specific heat capacity');
model.param.set('k_a', '0.016[W/m/K]', 'Thermal conductivity');
model.param.set('gamma_a', '1.7', 'Ratio of specific heats');
%Ti-6Al-4V properties
model.param.set('emissivity', '0.35', 'Emissivity');
model.param.set('T_m', '1928[K]', 'Melting temperature');
model.param.set('T_s', '1878[K]', 'Solidification temperature');
model.param.set('T_t', 'T_m+dT/2', 'Solid to liquid phase change');
model.param.set('T_b', 'T_s-dT/2', 'Liquid to solid phase change');
model.param.set('dT', '5', 'Temperature interval');
model.param.set('L', '286[J/g]', 'Latent heat of fusion');
model.param.set('rho_t', '4.43[g/cm^3]', 'Density');
model.param.set('rho_p', '0.7*rho_t+0.3*rho_a', 'Powder density');
model.param.set('Cpo', '688.5[J/kg/K]', 'Specific heat capacity');
model.param.set('k_s', '6[W/m/K]', 'Solid thermal conductivity');
model.param.set('k_l', '33.4[W/m/K]', 'Liquid thermal conductivity'
    );
model.param.set('k_p', '0.7*k_s+0.3*k_a', 'Powder thermal
    conductivity');
model.param.set('nu_t', '0.34', 'Poissons ratio');
model.param.set('E_t', '113.8[GPa]', 'Youngs modulus');
model.param.set('CTE_t', '9e-6[1/K]', 'Coef. thermal expansion');

model.component.create('comp1', true);
model.component('comp1').geom.create('geom1', 2);
model.component('comp1').geom('geom1').axisymmetric(true);
model.component('comp1').geom('geom1').lengthUnit('cm');

```

```
%Functions
model.component('comp1').func.create('step1', 'Step');
model.component('comp1').func('step1').set('smooth', 'dT');
model.component('comp1').func.create('an1', 'Analytic');
model.component('comp1').func('an1').label('Enthalpy Function,
    Solid to Liquid');
model.component('comp1').func('an1').set('funcname', 'H_StoL');
model.component('comp1').func('an1').set('expr', 'Cp0*T+L*step1((T-
    T_m[1/K]))');
model.component('comp1').func('an1').set('args', {'T'});
model.component('comp1').func('an1').set('argunit', 'K');
model.component('comp1').func('an1').set('fununit', 'J/kg');
model.component('comp1').func('an1').set('plotargs', {'T' '1800[K]'
    '2000[K]'});
model.component('comp1').func.create('an2', 'Analytic');
model.component('comp1').func('an2').label('Enthalpy Function,
    Liquid to Solid');
model.component('comp1').func('an2').set('funcname', 'H_LtoS');
model.component('comp1').func('an2').set('expr', 'Cp0*T+L*step1((T-
    T_s[1/K]))');
model.component('comp1').func('an2').set('args', {'T'});
model.component('comp1').func('an2').set('argunit', 'K');
model.component('comp1').func('an2').set('fununit', 'J/kg');
model.component('comp1').func('an2').set('plotargs', {'T' '1800[K]'
    '2000[K]'});
model.component('comp1').func.create('int1', 'Interpolation');
model.component('comp1').func('int1').active(false);
model.component('comp1').func.create('int2', 'Interpolation');
model.component('comp1').func('int2').active(false);
model.component('comp1').func.create('int3', 'Interpolation');
model.component('comp1').func('int3').active(false);
%Variables
model.component('comp1').variable.create('var1');
model.component('comp1').variable('var1').set('r_f', 'vel*t');
```

```
87 model.component('comp1').variable('var1').set('HeatFlux', '(2*P*
       factor/(pi*R_g^2))*exp(-(2*(r-r_f)^2/R_g^2))');
88
89 %Domain ODEs and DAEs: Phase Changes
90 model.component('comp1').physics.create('dode', 'DomainODE', 'geom1
       ');
91 model.component('comp1').physics('dode').field('dimensionless').
       field('SorL');
92 model.component('comp1').physics('dode').field('dimensionless').
       component({'SorL'});
93 model.component('comp1').physics('dode').prop('ShapeProperty').set(
       'order', 0);
94 model.component('comp1').physics('dode').prop('Units').set('
       CustomSourceTermUnit', 1);
95 model.component('comp1').physics('dode').feature('dode1').set('f',
       'SorL-nojac(if(T>T_t,0,if(T<T_b,1,SorL)))');
96 model.component('comp1').physics('dode').feature('dode1').set('da',
        0);
97 model.component('comp1').physics('dode').feature('init1').set('SorL
       ', 'SorL_init');
98 %Heat Transfer
99 model.component('comp1').physics.create('ht', '
       HeatTransferInSolidsAndFluids', 'geom1');
100 model.component('comp1').physics('ht').selection.all;
101 model.component('comp1').physics('ht').prop('PhysicalModelProperty'
       ).set('Tref', 'T_a');
102 model.component('comp1').physics('ht').feature('init1').set('Tinit'
       , 'T_a');
103 model.component('comp1').physics('ht').create('init2', 'init', 2);
104 model.component('comp1').physics('ht').feature('init2').active(
       false);
105 model.component('comp1').physics('ht').feature('solid1').set('k', {
       'if(r>r_f && SorL==1, k_p, SorL*k_s+(1-SorL)*k_l)'; '0'; '0'; '0
       '; 'if(r>r_f && SorL==1, k_p, SorL*k_s+(1-SorL)*k_l)'; '0'; '0';
```

```
    'o'; 'if(r>r_f && SorL==1, k_p, SorL*k_s+(1-SorL)*k_l)'});
106 model.component('comp1').physics('ht').feature('solid1').set('rho',
    'if(r>r_f && SorL==1, rho_p, rho_t)');
107 model.component('comp1').physics('ht').feature('solid1').set('Cp',
    'SorL*d(H_StoL(T),T)+(1-SorL)*d(H_LtoS(T),T)');
108 model.component('comp1').physics('ht').feature('fluid1').set('u',
    [0; 0; 0]);
109 model.component('comp1').physics('ht').create('dbp1', '
    DepositedBeamPower', 1);
110 model.component('comp1').physics('ht').feature('dbp1').set('e', [0;
     0; -1]);
111 model.component('comp1').physics('ht').feature('dbp1').set('Qb', '
    HeatFlux');
112 model.component('comp1').physics('ht').create('sar1', '
    SurfaceToAmbientRadiation', 1);
113 model.component('comp1').physics('ht').feature('sar1').set('
    epsilon_rad', 'emissivity');
114 model.component('comp1').physics('ht').feature('sar1').set('Tamb',
    'T_a');
115 %Structural Mechanics
116 model.component('comp1').physics.create('solid', 'SolidMechanics',
    'geom1');
117 model.component('comp1').physics('solid').prop('
    StructuralTransientBehavior').set('StructuralTransientBehavior',
     'Quasistatic');
118 model.component('comp1').physics('solid').create('init2', 'init',
    2);
119 model.component('comp1').physics('solid').feature('init2').active(
    false);
120 model.component('comp1').physics('solid').feature('lemm1').set('nu'
    , 'nu_t');
121 model.component('comp1').physics('solid').feature('lemm1').set('E',
     'E_t');
122 model.component('comp1').physics('solid').create('fix1', 'Fixed',
```

```
    1);
model.component('comp1').physics('solid').feature('lemm1').create('
    act1', 'Activation', 2);
model.component('comp1').physics('solid').feature('lemm1').feature(
    'act1').set('activation_expression', 'r<r_f && SorL==1');
model.component('comp1').physics('solid').feature('lemm1').create('
    act2', 'Activation', 2);
model.component('comp1').physics('solid').feature('lemm1').feature(
    'act2').active(false);
%Multiphysics: Thermal Expansion
model.component('comp1').multiphysics.create('te1', '
    ThermalExpansion', 2);
model.component('comp1').multiphysics('te1').set('
    minput_strainreferencetemperature', 'T_t');
model.component('comp1').multiphysics('te1').set('Heat_physics', '
    ht');
model.component('comp1').multiphysics('te1').set('Solid_physics', '
    solid');
model.component('comp1').multiphysics('te1').set('alpha', {'CTE_t';
     'o'; 'o'; 'o'; 'CTE_t'; 'o'; 'o'; 'o'; 'CTE_t'});
%Build chamber
model.geom('geom1').feature.create('r1', 'Rectangle');
model.geom('geom1').feature('r1').set('size', [rcam hcam]);
model.geom('geom1').feature('r1').set('pos', [0 -hcam/2]);
d_a = mphselectbox(model, 'geom1', [rcam+1/4 hcam/2+1/4; -rcam-1/4
    -hcam/2-1/4]'-[-rc-1/4 -tk/4; rc+1/4 tk*(iterations+1/4)]', '
    domain')
%Material: argon
model.component('comp1').material.create('mat1', 'Common');
model.component('comp1').material('mat1').label('Argon');
model.component('comp1').material('mat1').propertyGroup('def').set(
    'density', 'rho_a');
model.component('comp1').material('mat1').propertyGroup('def').set(
    'heatcapacity', 'Cp_a');
```

```
143 model.component('comp1').material('mat1').propertyGroup('def').set(
        'ratioofspecificheat', 'gamma_a');
144 model.component('comp1').material('mat1').propertyGroup('def').set(
        'thermalconductivity', {'k_a' '0' '0' '0' 'k_a' '0' '0' '0' 'k_a
        '});
145 %Material: Ti-6Al-4V
146 model.component('comp1').material.create('mat2', 'Common');
147 model.component('comp1').material('mat2').label('Ti-6Al-4V');
148 model.component('comp1').material('mat2').propertyGroup('def').set(
        'density', 'rho_t');
149 model.component('comp1').material('mat2').propertyGroup('def').set(
        'heatcapacity', 'Cpo');
150 model.component('comp1').material('mat2').propertyGroup('def').set(
        'youngsmodulus', 'E_t');
151 model.component('comp1').material('mat2').propertyGroup('def').set(
        'poissonsratio', 'nu_t');
152 model.component('comp1').material('mat2').propertyGroup('def').set(
        'thermalconductivity', {'k_t' '0' '0' '0' 'k_t' '0' '0' '0' 'k_t
        '});
153 model.component('comp1').material('mat2').propertyGroup('def').set(
        'coefficientofthermalexpansion', 'CTE_t');
154 %Mesh
155 model.component('comp1').mesh.create('mesh1');
156 model.component('comp1').mesh('mesh1').autoMeshSize(3);
157 %Study
158 model.study.create('std1');
159 model.study('std1').create('time', 'Transient');
160 model.sol.create('sol1');
161 model.sol('sol1').study('std1');
162 model.sol('sol1').attach('std1');
163 model.sol('sol1').create('st1', 'StudyStep');
164 model.sol('sol1').create('v1', 'Variables');
165 model.sol('sol1').create('t1', 'Time');
166 model.sol('sol1').feature('t1').create('se1', 'Segregated');
```

```
model.sol('sol1').feature('t1').create('ps1', 'PreviousSolution');
model.sol('sol1').feature('t1').feature('se1').create('ss1', '
    SegregatedStep');
model.sol('sol1').feature('t1').feature('se1').create('solid1', '
    SegregatedStep');
%Time step
model.study('std1').feature('time').set('tlist', 'range(0,t_step,
    t_last)');
model.sol('sol1').attach('std1');
model.sol('sol1').feature('v1').set('clist', {'range(0,t_step,
    t_last)' 't_step*t_last [s]'});
model.sol('sol1').feature('t1').set('tlist', 'range(0,t_step,t_last
    )');
model.sol('sol1').feature('t1').feature('se1').feature('ssDef').set
    ('segvar', {'comp1_T'});
model.sol('sol1').feature('t1').feature('se1').feature('ss1').set('
    segvar', {'comp1_SorL'});
model.sol('sol1').feature('t1').feature('se1').feature('solid1').
    set('segvar', {'comp1_u'});
model.sol('sol1').feature('t1').feature('ps1').set('prevcomp', {'
    comp1_SorL'});

nn = 1;
for n = 1:iterations
    tag1 = model.geom('geom1').feature.uniquetag('r');
    model.geom('geom1').feature.create(tag1, 'Rectangle');
    model.geom('geom1').feature(tag1).set('size', {rc tk});
    model.geom('geom1').feature(tag1).set('pos', [0 tk*(n-1)]);
    %Defining boundaries
    b_laser = mphselectbox(model, 'geom1', [rc*(-5/4) tk*(n-1/4);
        rc*(5/4) tk*(n+1/4)]', 'boundary')
    b_bottom = mphselectbox(model, 'geom1', [rc*(-5/4) -tk/4; rc
        *(5/4) tk/4]', 'boundary')
    %Defining domains
```

```
190     d_ti = mphselectbox(model, 'geom1', [rc*(-5/4) -tk/4; rc*(5/4)
            tk*(n+1/4)]', 'domain')
191     d_ti_current = mphselectbox(model, 'geom1', [rc*(-5/4) tk*(n
            -5/4); rc*(5/4) tk*(n+1/4)]', 'domain')
192     d_ti_past = mphselectbox(model, 'geom1', [rc*(-5/4) -tk/4; rc
            *(5/4) tk*(n-3/4)]', 'domain')
193     %Selections
194     model.material('mat1').selection.set(d_a);
195     model.material('mat2').selection.set(d_ti);
196     model.physics('dode').selection.set(d_ti);
197     model.physics('dode').selection.remove(d_a);
198     model.physics('ht').feature('fluid1').selection.set(d_a);
199     model.physics('solid').selection.set(d_ti);
200     model.physics('solid').selection.remove(d_a);
201     model.multiphysics('te1').selection.set(d_ti);
202     model.multiphysics('te1').selection.remove(d_a);
203     model.physics('ht').feature('dbp1').selection.set(b_laser);
204     model.physics('ht').feature('sar1').selection.set(b_laser);
205     model.physics('solid').feature('fix1').selection.set(b_bottom);
206     model.physics('solid').feature('lemm1').feature('act1').
            selection.set(d_ti_current);
207     %Set temperature and displacement field as initial conditions
208     if n == 1
209         model.component('comp1').physics('ht').feature('init1').set(
                'Tinit', 'T_a');
210         model.component('comp1').physics('solid').feature('init1').
                set('u', {'0' '0' '0'});
211     else
212         model.component('comp1').func('int1').active(true);
213         model.component('comp1').func('int1').set('source', 'file');
214         imp_filenameT = sprintf('%s_%d.txt',[path,'temp'],n-1)
215         model.component('comp1').func('int1').set('filename',
                imp_filenameT);
216         model.component('comp1').func('int1').importData;
```

```
217         model.component('comp1').func('int1').set('argunit', 'cm');
218         model.component('comp1').func('int1').set('fununit', 'K');
219         model.component('comp1').func('int2').active(true);
220         model.component('comp1').func('int2').set('source', 'file');
221         imp_filenamerD = sprintf('%s_%d.txt',[path,'r_disp'],n-1)
222         model.component('comp1').func('int2').set('filename',
              imp_filenamerD);
223         model.component('comp1').func('int2').importData;
224         model.component('comp1').func('int2').set('argunit', 'cm');
225         model.component('comp1').func('int2').set('fununit', 'cm');
226         model.component('comp1').func('int3').active(true);
227         model.component('comp1').func('int3').set('source', 'file');
228         imp_filenamezD = sprintf('%s_%d.txt',[path,'z_disp'],n-1)
229         model.component('comp1').func('int3').set('filename',
              imp_filenamezD);
230         model.component('comp1').func('int3').importData;
231         model.component('comp1').func('int3').set('argunit', 'cm');
232         model.component('comp1').func('int3').set('fununit', 'cm');
233         model.component('comp1').physics('ht').feature('init1').set(
              'Tinit', 'T_a');
234         model.component('comp1').physics('solid').feature('init1').
              set('u', {'0' '0' '0'});
235         model.component('comp1').physics('ht').feature('init2').
              active(true);
236         model.component('comp1').physics('ht').feature('init2').set(
              'Tinit', 'int1(r,z)');
237         model.component('comp1').physics('ht').feature('init2').
              selection.set(d_ti_past);
238         model.component('comp1').physics('ht').feature('init2').
              selection.set(d_a);
239         model.component('comp1').physics('solid').feature('init2').
              active(true);
240         model.component('comp1').physics('solid').feature('init2').
              set('u', {'int2(r,z)' '0' 'int3(r,z)'});
```

```
241         model.component('comp1').physics('solid').feature('init2').
                selection.set(d_ti_past);
242         model.component('comp1').physics('solid').feature('lemm1').
                feature('act2').active(true);
243         model.component('comp1').physics('solid').feature('lemm1').
                feature('act2').set('activation_expression', ['z<tk*',
                num2str(n-1),' && SorL==1']);
244         model.component('comp1').physics('solid').feature('lemm1').
                feature('act2').selection.set(d_ti_past);
245     end
246     %Mesh
247     model.mesh('mesh1').run;
248     fprintf('Running, iteration No.%d',n)
249
250     model.sol('sol1').runAll;
251
252     %Temperature data of all the layers for t=last (pg1)
253     tag2 = model.result.uniquetag('pg');
254     model.result.create(tag2, 'PlotGroup2D');
255     model.result(tag2).create('surf1', 'Surface');
256     model.result(tag2).feature('surf1').set('expr', 'T');
257     level_1 = timelast/timestep+1;
258     model.result(tag2).setIndex('looplevel', level_1, 0);
259     model.result(tag2).run;
260     %Export temperature data of all the layers for t=last
261     tag3 = model.result.export.uniquetag('plot');
262     model.result.export.create(tag3, tag2, 'surf1', 'Plot');
263     exp_filenameT = sprintf('%s_%d.txt',[path,'temp'],n)
264     model.result.export(tag3).set('filename', exp_filenameT);
265     model.result.export(tag3).run;
266
267     %Displacement field of all the layers for t=last (pg2)
268     tag4 = model.result.uniquetag('pg');
269     model.result.create(tag4, 'PlotGroup2D');
```

```
270     model.result(tag4).create('surf1', 'Surface');
271     model.result(tag4).feature('surf1').set('expr', 'u');
272     model.result(tag4).feature('surf1').label('Displacement R');
273     model.result(tag4).feature('surf1').set('const', {'solid.
            refpntr' '0' 'Reference point for moment computation, r
            coordinate'; 'solid.refpntphi' '0' 'Reference point for
            moment computation, phi coordinate'; 'solid.refpntz' '0' '
            Reference point for moment computation, z coordinate'});
274     model.result(tag4).feature('surf1').set('resolution', 'normal')
            ;
275     model.result(tag4).create('surf2', 'Surface');
276     model.result(tag4).feature('surf2').set('expr', 'w');
277     model.result(tag4).feature('surf2').label('Displacement Z');
278     model.result(tag4).feature('surf2').set('const', {'solid.
            refpntr' '0' 'Reference point for moment computation, r
            coordinate'; 'solid.refpntphi' '0' 'Reference point for
            moment computation, phi coordinate'; 'solid.refpntz' '0' '
            Reference point for moment computation, z coordinate'});
279     model.result(tag4).feature('surf2').set('resolution', 'normal')
            ;
280     model.result(tag4).setIndex('looplevel', level_1, 0);
281     %Export r-displacement of all the layers for t=last
282     tag5 = model.result.export.uniquetag('plot');
283     model.result.export.create(tag5, tag4, 'surf1', 'Plot');
284     exp_filenamerD = sprintf('%s_%d.txt',[path,'r_disp'],n)
285     model.result.export(tag5).set('filename', exp_filenamerD);
286     model.result.export(tag5).run;
287     %Export z-displacement of all the layers for t=last
288     tag6 = model.result.export.uniquetag('plot');
289     model.result.export.create(tag6, tag4, 'surf2', 'Plot');
290     exp_filenamezD = sprintf('%s_%d.txt',[path,'z_disp'],n)
291     model.result.export(tag6).set('filename', exp_filenamezD);
292     model.result.export(tag6).run;
293
```

```
294     %von Mises stress (pg3)
295     tag7 = model.result.uniquetag('pg');
296     model.result.create(tag7, 'PlotGroup2D');
297     model.result(tag7).create('surf1', 'Surface');
298     model.result(tag7).feature('surf1').set('expr', 'solid.mises');
299     model.result(tag7).feature('surf1').set('descr', 'von Mises
            stress');
300     model.result(tag7).feature('surf1').set('unit', 'MPa');
301     model.result(tag7).setIndex('looplevel', level_1, 0);
302     model.result(tag7).feature('surf1').create('def1', 'Deform');
303     model.result(tag7).feature('surf1').create('filt1', 'Filter');
304     model.result(tag7).feature('surf1').feature('filt1').set('expr'
            , 'solid.isactive');
305     model.result(tag7).run;
306
307     %Plots
308     if rem(n,100) == 0
309         figure(1)
310         subplot(sp_1,sp_2,nn)
311         mphgeom(model,'geom1','edgelabels','on')
312         drawnow
313         figure(2)
314         subplot(sp_1,sp_2,nn)
315         mphplot(model,'pg1','rangenum',1)
316         drawnow
317         figure(3)
318         subplot(sp_1,sp_2,nn)
319         mphplot(model,'pg2','rangenum',1)
320         drawnow
321         figure(4)
322         subplot(sp_1,sp_2,nn)
323         mphplot(model,'pg3','rangenum',1)
324         drawnow
325         nn=nn+1;
```

```
326     end
327     disp(sprintf('End of iteration No.%d',n))
328 end
329 toc
330 out = model;
```

B.2 Dog-bone Cylinder

```
1  function out = model
2  tic
3  import com.comsol.model.*
4  import com.comsol.model.util.*
5  model = ModelUtil.create('Model');
6
7  %Iterations and subplots
8  iterations = 2000;
9  sp_1 = 4;
10 sp_2 = 5;
11 %Parameters
12 timestep = 0.01;
13 timelast = 60; %[s]
14 timelastit = 20; %[h]
15 path = "Files";
16 tk = 0.005; %[cm]
17 hp = 2; %[cm]
18 hcam = 40; %[cm]
19 rcam = 15; %[cm]
20 hc = 10; %[cm]
21 rc = 0.6; %[cm]
22 model.param.set('t_step', num2str(timestep), 'Time step');
23 model.param.set('t_last', num2str(timelast), 'Last time');
24 model.param.set('t_lastit', num2str(timelastit), 'Last time of the
       last iteration');
```

```
model.param.set('tk', num2str(tk), 'Layer thickness');
model.param.set('hp', num2str(hp), 'Platform thickness');
model.param.set('hc', num2str(hc), 'Cylinder height');
model.param.set('rc', num2str(rc), 'Cylinder radius');
model.param.set('hcam', num2str(hcam), 'Camera height');
model.param.set('rcam', num2str(rcam), 'Camera radius');
model.param.set('T_a', '300[K]', 'Initial temperature');
model.param.set('T_pf', '700[K]', 'Platform temperature');
model.param.set('T_pb', '700[K]', 'Powder bed temperature');
model.param.set('Tamb', '293[K]', 'Ambient temperature');
model.param.set('SorL_init', '1', 'Initial material state');
model.param.set('vel', '3[cm/s]', 'Velocity magnitude');
model.param.set('P', '100[W]', 'Laser power');
model.param.set('factor', '1', 'Absorption factor');
model.param.set('R_g', '0.01[cm]', 'Standard deviation');
%Argon properties
model.param.set('rho_a', '0.0016[g/cm^3]', 'Density');
model.param.set('Cp_a', '520[J/kg/K]', 'Specific heat capacity');
model.param.set('k_a', '0.016[W/m/K]', 'Thermal conductivity');
model.param.set('gamma_a', '1.7', 'Ratio of specific heats');
%Ti-6Al-4V properties
model.param.set('emissivity', '0.35', 'Emissivity');
model.param.set('T_m', '1928[K]', 'Melting temperature');
model.param.set('T_s', '1878[K]', 'Solidification temperature');
model.param.set('T_t', 'T_m+dT/2', 'Solid to liquid phase change');
model.param.set('T_b', 'T_s-dT/2', 'Liquid to solid phase change');
model.param.set('dT', '5', 'Temperature interval');
model.param.set('L', '286[J/g]', 'Latent heat of fusion');
model.param.set('rho_s', '4.43[g/cm^3]', 'Solid density');
model.param.set('rho_l', '3.8[g/cm^3]', 'Liquid density');
model.param.set('rho_p', '0.7*rho_s+0.3*rho_a', 'Powder density');
model.param.set('Cpo', '688.5[J/kg/K]', 'Specific heat capacity');
model.param.set('k_p', '0.33[W/m/K]', 'Powder thermal conductivity'
    );
```

```
model.param.set('nu_t', '0.34', 'Poissons ratio');
model.param.set('E_t', '113.8[GPa]', 'Youngs modulus');
model.param.set('CTE_t', '9e-6[1/K]', 'Coef. thermal expansion');

model.component.create('comp1', true);
model.component('comp1').geom.create('geom1', 2);
model.component('comp1').geom('geom1').axisymmetric(true);
model.component('comp1').geom('geom1').lengthUnit('cm');

%Functions
model.func.create('step1', 'Step');
model.func('step1').set('smooth', 'dT');
model.func.create('an1', 'Analytic');
model.func('an1').label('Enthalpy Function, Solid to Liquid');
model.func('an1').set('funcname', 'H_StoL');
model.func('an1').set('expr', 'Cp0*T+L*step1((T-T_m[1/K]))');
model.func('an1').set('args', {'T'});
model.func('an1').set('argunit', 'K');
model.func('an1').set('fununit', 'J/kg');
model.func('an1').set('plotargs', {'T' '1800[K]' '2000[K]'});
model.func.create('an2', 'Analytic');
model.func('an2').label('Enthalpy Function, Liquid to Solid');
model.func('an2').set('funcname', 'H_LtoS');
model.func('an2').set('expr', 'Cp0*T+L*step1((T-T_s[1/K]))');
model.func('an2').set('args', {'T'});
model.func('an2').set('argunit', 'K');
model.func('an2').set('fununit', 'J/kg');
model.func('an2').set('plotargs', {'T' '1800[K]' '2000[K]'});
model.func.create('int1', 'Interpolation');
model.func('int1').active(false);
model.func.create('int2', 'Interpolation');
model.func('int2').active(false);
model.func.create('int3', 'Interpolation');
model.func('int3').active(false);
```

```
92  model.func.create('pw1', 'Piecewise');
93  model.func('pw1').set('funcname', 'k_t');
94  model.func('pw1').set('arg', 'T');
95  model.func('pw1').setIndex('pieces', 0, 0, 0);
96  model.func('pw1').setIndex('pieces', 'T_top', 0, 1);
97  model.func('pw1').setIndex('pieces', '0.0168*T+0.9586', 0, 2);
98  model.func('pw1').setIndex('pieces', 'T_top', 1, 0);
99  model.func('pw1').setIndex('pieces', 10000, 1, 1);
100 model.func('pw1').setIndex('pieces', 33.4, 1, 2);
101 model.func('pw1').set('argunit', 'K');
102 model.func('pw1').set('fununit', 'W/m/K');
103 %Variables
104 model.component('comp1').variable.create('var1');
105 model.component('comp1').variable('var1').set('r_f', 'vel*t');
106 model.component('comp1').variable('var1').set('HeatFlux', '(2*P*
        factor/(pi*R_g^2))*exp(-(2*(r-r_f)^2/R_g^2))');
107
108 %Domain ODEs and DAEs: Phase Changes
109 model.component('comp1').physics.create('dode', 'DomainODE', 'geom1
        ');
110 model.component('comp1').physics('dode').field('dimensionless').
        field('SorL');
111 model.component('comp1').physics('dode').field('dimensionless').
        component({'SorL'});
112 model.component('comp1').physics('dode').prop('ShapeProperty').set(
        'order', 0);
113 model.component('comp1').physics('dode').prop('Units').set('
        CustomSourceTermUnit', 1);
114 model.component('comp1').physics('dode').feature('dode1').set('f',
        'SorL-nojac(if(T>T_t,0,if(T<T_b,1,SorL)))');
115 model.component('comp1').physics('dode').feature('dode1').set('da',
         0);
116 model.component('comp1').physics('dode').feature('init1').set('SorL
        ', 'SorL_init');
```

```
117 %Heat Transfer
118 model.component('comp1').physics.create('ht', '
    HeatTransferInSolidsAndFluids', 'geom1');
119 model.component('comp1').physics('ht').selection.all;
120 model.component('comp1').physics('ht').prop('PhysicalModelProperty'
    ).set('Tref', 'T_a');
121 model.component('comp1').physics('ht').create('init2', 'init', 2);
122 model.component('comp1').physics('ht').feature('init2').set('Tinit'
    , 'T_pb');
123 model.component('comp1').physics('ht').create('init3', 'init', 2);
124 model.component('comp1').physics('ht').feature('init3').set('Tinit'
    , 'T_pf');
125 model.component('comp1').physics('ht').feature('solid1').set('k', {
    'if(r>r_f && SorL==1, k_p, k_t(T))'; 'o'; 'o'; 'o'; 'if(r>r_f &&
     SorL==1, k_p, k_t(T))'; 'o'; 'o'; 'o'; 'if(r>r_f && SorL==1,
    k_p, k_t(T))'});
126 model.component('comp1').physics('ht').feature('solid1').set('rho',
     'if(r>r_f && SorL==1, rho_p, SorL*rho_s+(1-SorL)*rho_l)');
127 model.component('comp1').physics('ht').feature('solid1').set('Cp',
    'SorL*d(H_StoL(T),T)+(1-SorL)*d(H_LtoS(T),T)');
128 model.component('comp1').physics('ht').create('solid2', '
    SolidHeatTransferModel', 2);
129 model.component('comp1').physics('ht').feature('solid2').active(
    false);
130 model.component('comp1').physics('ht').feature('solid2').set('k', {
    'k_t(T)'; 'o'; 'o'; 'o'; 'k_t(T)'; 'o'; 'o'; 'o'; 'k_t(T)'});
131 model.component('comp1').physics('ht').feature('solid2').set('rho',
     'SorL*rho_s+(1-SorL)*rho_l');
132 model.component('comp1').physics('ht').feature('solid2').set('Cp',
    'SorL*d(H_StoL(T),T)+(1-SorL)*d(H_LtoS(T),T)');
133 model.component('comp1').physics('ht').create('solid3', '
    SolidHeatTransferModel', 2);
134 model.component('comp1').physics('ht').feature('solid3').set('k', {
    'k_p'; 'o'; 'o'; 'o'; 'k_p'; 'o'; 'o'; 'o'; 'k_p'});
```

```
135 model.component('comp1').physics('ht').feature('solid3').set('rho',
        'rho_p');
136 model.component('comp1').physics('ht').feature('solid3').set('Cp',
        'd(H_StoL(T),T)');
137 model.component('comp1').physics('ht').create('solid4', '
        SolidHeatTransferModel', 2);
138 model.component('comp1').physics('ht').feature('fluid1').set('u',
        [0.001; 0; 0.001]); %[m/s]
139 model.component('comp1').physics('ht').create('dbp1', '
        DepositedBeamPower', 1);
140 model.component('comp1').physics('ht').feature('dbp1').set('e', [0;
         0; -1]);
141 model.component('comp1').physics('ht').feature('dbp1').set('Qb', '
        HeatFlux');
142 model.component('comp1').physics('ht').create('sar1', '
        SurfaceToAmbientRadiation', 1);
143 model.component('comp1').physics('ht').feature('sar1').set('
        epsilon_rad', 'emissivity');
144 model.component('comp1').physics('ht').feature('sar1').set('Tamb',
        'T_a');
145 model.component('comp1').physics('ht').create('temp1', '
        TemperatureBoundary', 1);
146 model.component('comp1').physics('ht').feature('temp1').set('To', '
        Tamb');
147 %Structural Mechanics
148 model.component('comp1').physics.create('solid', 'SolidMechanics',
        'geom1');
149 model.component('comp1').physics('solid').prop('
        StructuralTransientBehavior').set('StructuralTransientBehavior',
         'Quasistatic');
150 model.component('comp1').physics('solid').create('init2', 'init',
        2);
151 model.component('comp1').physics('solid').feature('init2').active(
        false);
```

```
152 model.component('comp1').physics('solid').create('fix1', 'Fixed',
        1);
153 model.component('comp1').physics('solid').feature('lemm1').create('
        act1', 'Activation', 2);
154 model.component('comp1').physics('solid').feature('lemm1').feature(
        'act1').set('activation_expression', 'r<r_f && SorL==1');
155 model.component('comp1').physics('solid').feature('lemm1').create('
        act2', 'Activation', 2);
156 model.component('comp1').physics('solid').feature('lemm1').feature(
        'act2').active(false);
157 %Multiphysics: Thermal Expansion
158 model.component('comp1').multiphysics.create('te1', '
        ThermalExpansion', 2);
159 model.component('comp1').multiphysics('te1').set('
        minput_strainreferencetemperature', 'T_pf');
160 model.component('comp1').multiphysics('te1').set('Heat_physics', '
        ht');
161 model.component('comp1').multiphysics('te1').set('Solid_physics', '
        solid');
162 %Build chamber
163 model.component('comp1').geom('geom1').feature.create('r1', '
        Rectangle');
164 model.component('comp1').geom('geom1').feature('r1').set('size', [
        rcam hcam]);
165 model.component('comp1').geom('geom1').feature('r1').set('pos', [0
        0]);
166 %Material: argon
167 model.component('comp1').material.create('mat1', 'Common');
168 model.component('comp1').material('mat1').label('Argon');
169 model.component('comp1').material('mat1').propertyGroup('def').set(
        'density', 'rho_a');
170 model.component('comp1').material('mat1').propertyGroup('def').set(
        'heatcapacity', 'Cp_a');
171 model.component('comp1').material('mat1').propertyGroup('def').set(
```

```
    'ratioofspecificheat', 'gamma_a');
model.component('comp1').material('mat1').propertyGroup('def').set(
    'thermalconductivity', {'k_a' '0' '0' '0' 'k_a' '0' '0' '0' 'k_a
    '});
%Dog-bone Cylinder
model.component('comp1').geom('geom1').create('imp1', 'Import');
model.component('comp1').geom('geom1').feature('imp1').set('type',
    'native');
model.component('comp1').geom('geom1').feature('imp1').set('
    filename', [path,'dbc_geom2D_alt.mphtxt']);
model.component('comp1').geom('geom1').feature('imp1').importData;
model.component('comp1').geom('geom1').create('ls1', 'LineSegment')
    ;
model.component('comp1').geom('geom1').feature('ls1').active(false)
    ;
model.component('comp1').geom('geom1').create('ls2', 'LineSegment')
    ;
model.component('comp1').geom('geom1').feature('ls2').active(false)
    ;
model.component('comp1').geom('geom1').create('pard1', '
    PartitionDomains');
model.component('comp1').geom('geom1').feature('pard1').active(
    false);
model.component('comp1').geom('geom1').create('pard2', '
    PartitionDomains');
model.component('comp1').geom('geom1').feature('pard2').active(
    false);
%Material: Ti-6Al-4V
model.component('comp1').material.create('mat2', 'Common');
model.component('comp1').material('mat2').label('Ti-6Al-4V');
model.component('comp1').material('mat2').propertyGroup('def').set(
    'density', 'rho_s');
model.component('comp1').material('mat2').propertyGroup('def').set(
    'heatcapacity', 'Cpo');
```

```
model.component('comp1').material('mat2').propertyGroup('def').set('youngsmodulus', 'E_t');
model.component('comp1').material('mat2').propertyGroup('def').set('poissonsratio', 'nu_t');
% model.material('mat2').propertyGroup('def').set('thermalconductivity', {'k_t(T)' '0' '0' '0' 'k_t(T)' '0' '0' '0' 'k_t(T)'});
model.component('comp1').material('mat2').propertyGroup('def').set('thermalexpansioncoefficient', 'CTE_t');
%Material: Steel AISI 4340
model.component('comp1').material.create('mat3', 'Common');
model.component('comp1').material('mat3').label('Steel AISI 4340');
model.component('comp1').material('mat3').set('family', 'steel');
model.component('comp1').material('mat3').propertyGroup('def').set('heatcapacity', '475[J/(kg*K)]');
model.component('comp1').material('mat3').propertyGroup('def').set('density', '7850[kg/m^3]');
model.component('comp1').material('mat3').propertyGroup('def').set('thermalconductivity', {'44.5[W/(m*K)]' '0' '0' '0' '44.5[W/(m*K)]' '0' '0' '0' '44.5[W/(m*K)]'});
model.component('comp1').material('mat3').propertyGroup('def').set('thermalexpansioncoefficient', '12.3e-6[1/K]');
model.component('comp1').material('mat3').propertyGroup('def').set('youngsmodulus', '205e9[Pa]');
model.component('comp1').material('mat3').propertyGroup('def').set('poissonsratio', '0.28');
%Platform
model.component('comp1').geom('geom1').feature.create('r2', 'Rectangle');
model.component('comp1').geom('geom1').feature('r2').set('size', [rcam hp]);
model.component('comp1').geom('geom1').feature('r2').set('pos', [0 -hp]);
%Mesh
```

```
model.component('comp1').mesh.create('mesh1');
model.component('comp1').mesh('mesh1').autoMeshSize(6);
%Study
model.study.create('std1');
model.study('std1').create('time', 'Transient');
model.sol.create('sol1');
model.sol('sol1').study('std1');
model.sol('sol1').attach('std1');
model.sol('sol1').create('st1', 'StudyStep');
model.sol('sol1').create('v1', 'Variables');
model.sol('sol1').create('t1', 'Time')
model.sol('sol1').feature('t1').create('se1', 'Segregated');
model.sol('sol1').feature('t1').create('ps1', 'PreviousSolution');
model.sol('sol1').feature('t1').feature('se1').create('ss1', '
    SegregatedStep');
model.sol('sol1').feature('t1').feature('se1').create('solid1', '
    SegregatedStep');
model.sol('sol1').feature('t1').feature('se1').feature('ssDef').set
    ('segvar', {'comp1_T'});
model.sol('sol1').feature('t1').feature('se1').feature('ss1').set('
    segvar', {'comp1_SorL'});
model.sol('sol1').feature('t1').feature('se1').feature('solid1').
    set('segvar', {'comp1_u'});
model.sol('sol1').feature('t1').feature('ps1').set('prevcomp', {'
    comp1_SorL'});

nn = 1;
for n = 1:iterations
    model.component('comp1').geom('geom1').feature('ls1').active(
        true);
    model.component('comp1').geom('geom1').feature('ls1').set('
        selresult', true);
    model.component('comp1').geom('geom1').feature('ls1').set('
        specify1', 'coord');
```

```
235     model.component('comp1').geom('geom1').feature('ls1').set('
            coord1', [0 tk*n]);
236     model.component('comp1').geom('geom1').feature('ls1').set('
            specify2', 'coord');
237     model.component('comp1').geom('geom1').feature('ls1').set('
            coord2', [rcam tk*n]);
238     model.component('comp1').geom('geom1').feature('pard1').active(
            true);
239     model.component('comp1').geom('geom1').feature('pard1').
            selection('domain').set('imp1(1)', 1);
240     model.component('comp1').geom('geom1').feature('pard1').
            selection('domain').set('r1(1)', 1);
241     model.component('comp1').geom('geom1').feature('pard1').
            selection('vertexsegment').named('ls1');
242     if n > 1
243         model.component('comp1').geom('geom1').feature('ls2').active
                (true);
244         model.component('comp1').geom('geom1').feature('ls2').set('
                selresult', true);
245         model.component('comp1').geom('geom1').feature('ls2').set('
                specify1', 'coord');
246         model.component('comp1').geom('geom1').feature('ls2').set('
                coord1', [0 tk*(n-1)]);
247         model.component('comp1').geom('geom1').feature('ls2').set('
                specify2', 'coord');
248         model.component('comp1').geom('geom1').feature('ls2').set('
                coord2', [rcam tk*(n-1)]);
249         model.component('comp1').geom('geom1').feature('pard2').
                active(true);
250         model.component('comp1').geom('geom1').feature('pard2').
                selection('domain').set('pard1(1)', 2);
251         model.component('comp1').geom('geom1').feature('pard2').
                selection('vertexsegment').named('ls2');
252     end
```

```
253     model.component('comp1').geom('geom1').run;
254     %Defining boundaries
255     b_laser = mphselectbox(model, 'geom1', [rc*(-5/4) tk*(n-1/4);
            rc*5/4 tk*(n+1/4)]', 'boundary')
256     b_bottom = mphselectbox(model, 'geom1', [rc*(-5/4) -tk/4; rc
            *5/4 tk/4]', 'boundary')
257     b_top = mphselectbox(model, 'geom1',[-rcam-1/4 hcam-1/4; rcam
            +1/4 hcam+1/4]', 'boundary')
258     b_lat = mphselectbox(model, 'geom1',[rcam-1/4 -1e-2; rcam+1/4
            hcam+1/4]', 'boundary')
259     b_temp = [b_top b_lat]
260     %Defining domains
261     d_ti = mphselectbox(model, 'geom1', [rc*(-5/4) -tk/4; rc*5/4 tk
            *(n+1/4)]', 'domain')
262     d_ti_current = mphselectbox(model, 'geom1', [rc*(-5/4) tk*(n
            -5/4); rc*5/4 tk*(n+1/4)]', 'domain')
263     d_ti_past = mphselectbox(model, 'geom1', [rc*(-5/4) -tk/4; rc
            *5/4 tk*(n-3/4)]', 'domain')
264     d_pf = mphselectbox(model, 'geom1', [-rcam-0.5 -hp-0.5; rcam
            +0.5 1e-5]', 'domain')
265     d_a = mphselectbox(model, 'geom1', [-rcam-1/4 tk*(n-1/4); rcam
            +1/4 hcam+1/4]', 'domain')
266     d_pb = mphselectbox(model, 'geom1', [-rcam-1/4 -1/4; rcam+1/4
            tk*(n+1/4)]', 'domain')
267     d_struct = [d_ti d_pf]
268     d_ti_p_current = mphselectbox(model, 'geom1', [rcam*(-5/4) tk*(
            n-5/4); rcam*5/4 tk*(n+1/4)]', 'domain')
269     d_init = [d_ti_past d_pf]
270     %Selections
271     model.component('comp1').material('mat1').selection.set(d_a);
272     model.component('comp1').material('mat2').selection.set(d_pb);
273     model.component('comp1').material('mat3').selection.set(d_pf);
274     model.component('comp1').physics('dode').selection.set(d_ti);
275     model.component('comp1').physics('ht').feature('fluid1').
```

```
        selection.set(d_a);
276     model.component('comp1').physics('ht').feature('solid3').
        selection.set(d_pb);
277     model.component('comp1').physics('ht').feature('solid3').
        selection.remove(d_ti_current);
278     model.component('comp1').physics('ht').feature('solid3').
        selection.remove(d_ti_past);
279     model.component('comp1').physics('ht').feature('solid4').
        selection.set(d_pf);
280     model.component('comp1').physics('ht').feature('init2').
        selection.set(d_ti_p_current);
281     model.component('comp1').physics('ht').feature('init3').
        selection.set(d_pf);
282     model.component('comp1').physics('solid').selection.set(
        d_struct);
283     model.component('comp1').multiphysics('te1').selection.set(
        d_struct);
284     model.component('comp1').physics('ht').feature('dbp1').
        selection.set(b_laser);
285     model.component('comp1').physics('ht').feature('sar1').
        selection.set(b_laser);
286     model.component('comp1').physics('ht').feature('temp1').
        selection.set(b_temp);
287     model.component('comp1').physics('solid').feature('fix1').
        selection.set(b_bottom);
288     model.component('comp1').physics('solid').feature('lemm1').
        feature('act1').selection.set(d_ti_current);
289     %Time step
290     if n < iterations
291         model.study('std1').feature('time').set('tlist', 'range(0,
            t_step,t_last)');
292         model.sol('sol1').attach('std1');
293         model.sol('sol1').feature('v1').set('clist', {'range(0,
            t_step,t_last)' 't_step*t_last [s]'});
```

```
294         model.sol('sol1').feature('t1').set('tlist', 'range(0,t_step
                ,t_last)');
295     else
296         %Maximum Operation
297         model.component('comp1').cpl.create('maxop1', 'Maximum');
298         model.component('comp1').cpl('maxop1').selection.set(d_ti);
299         model.study('std1').feature('time').set('tunit', 'h');
300         model.study('std1').feature('time').set('tlist', 'range(0,
                t_step,t_lastit)');
301         model.sol('sol1').attach('std1');
302         model.sol('sol1').feature('v1').set('clist', {'range(0,
                t_step,t_lastit)' 't_step*t_lastit'});
303         model.sol('sol1').feature('t1').set('tlist', 'range(0,t_step
                ,t_lastit)');
304         %Stop Condition
305         model.sol('sol1').feature('t1').create('st1', 'StopCondition
                ');
306         model.sol('sol1').feature('t1').feature('st1').setIndex('
                stopcondterminateon', 'true', 0);
307         model.sol('sol1').feature('t1').feature('st1').setIndex('
                stopcondActive', true, 0);
308         model.sol('sol1').feature('t1').feature('st1').setIndex('
                stopconddesc', 'Stop expression 1', 0);
309         model.sol('sol1').feature('t1').feature('st1').setIndex('
                stopcondarr', 'comp1.maxop1(comp1.T) <= 293[K]', 0);
310         %Activate warning
311         model.sol('sol1').feature('t1').feature('st1').set('
                stopcondwarn', true);
312     end
313     %Set temperature and displacement field as initial conditions
314     if n == 1
315         model.component('comp1').physics('ht').feature('init1').set(
                'Tinit', 'T_a');
316         model.component('comp1').physics('solid').feature('init1').
```

```
            set('u', {'0' '0' '0'});
317     else
318         model.func('int1').active(true);
319         model.func('int1').set('source', 'file');
320         imp_filenameT = sprintf('%s_%d.txt',[path,'temp'],n-1)
321         model.func('int1').set('filename', imp_filenameT);
322         model.func('int1').importData;
323         model.func('int1').set('argunit', 'cm');
324         model.func('int1').set('fununit', 'K');
325         model.func('int2').active(true);
326         model.func('int2').set('source', 'file');
327         imp_filenamerD = sprintf('%s_%d.txt',[path,'r_disp'],n-1)
328         model.func('int2').set('filename', imp_filenamerD);
329         model.func('int2').importData;
330         model.func('int2').set('argunit', 'cm');
331         model.func('int2').set('fununit', 'cm');
332         model.func('int3').active(true);
333         model.func('int3').set('source', 'file');
334         imp_filenamezD = sprintf('%s_%d.txt',[path,'z_disp'],n-1)
335         model.func('int3').set('filename', imp_filenamezD);
336         model.func('int3').importData;
337         model.func('int3').set('argunit', 'cm');
338         model.func('int3').set('fununit', 'cm');
339         model.component('comp1').physics('ht').feature('init1').set(
              'Tinit', 'int1(r,z)');
340         model.component('comp1').physics('solid').feature('init1').
              set('u', {'0' '0' '0'});
341         model.component('comp1').physics('ht').feature('solid2').
              active(true);
342         model.component('comp1').physics('ht').feature('solid2').
              selection.set(d_ti_past);
343         model.component('comp1').physics('solid').feature('init2').
              active(true);
344         model.component('comp1').physics('solid').feature('init2').
```

```
            set('u', {'int2(r,z)' '0' 'int3(r,z)'});
345         model.component('comp1').physics('solid').feature('init2').
                selection.set(d_init);
346         model.component('comp1').physics('solid').feature('lemm1').
                feature('act2').active(true);
347         model.component('comp1').physics('solid').feature('lemm1').
                feature('act2').set('activation_expression', ['z<tk*',
                num2str(n-1),' && SorL==1']);
348         model.component('comp1').physics('solid').feature('lemm1').
                feature('act2').selection.set(d_ti_past);
349     end
350     %Mesh
351     model.component('comp1').mesh('mesh1').run;
352     fprintf('Running, n=%d\n',n)
353
354     model.sol('sol1').runAll;
355
356     level_1 = timelast/timestep+1;
357     %Temperature data of all the layers for t=last (pg1)
358     tag2 = model.result.uniquetag('pg');
359     model.result.create(tag2, 'PlotGroup2D');
360     model.result(tag2).create('surf1', 'Surface');
361     model.result(tag2).feature('surf1').set('expr', 'T');
362     if n < iterations
363         model.result(tag2).setIndex('looplevel', level_1, 0);
364     else
365         model.result(tag2).setIndex('looplevel', 'interp', 0);
366     end
367     model.result(tag2).run;
368     %Export temperature data of all the layers for t=last
369     tag3 = model.result.export.uniquetag('plot');
370     model.result.export.create(tag3, tag2, 'surf1', 'Plot');
371     exp_filenameT = sprintf('%s_%d.txt',[path,'temp'],n)
372     model.result.export(tag3).set('filename', exp_filenameT);
```

```
373     model.result.export(tag3).run;
374
375     %Displacement field of all the layers for t=last (pg2)
376     tag4 = model.result.uniquetag('pg');
377     model.result.create(tag4, 'PlotGroup2D');
378     model.result(tag4).create('surf1', 'Surface');
379     model.result(tag4).feature('surf1').set('expr', 'u');
380     model.result(tag4).feature('surf1').label('Displacement R');
381     model.result(tag4).feature('surf1').set('const', {'solid.
          refpntr' '0' 'Reference point for moment computation, r
          coordinate'; 'solid.refpntphi' '0' 'Reference point for
          moment computation, phi coordinate'; 'solid.refpntz' '0' '
          Reference point for moment computation, z coordinate'});
382     model.result(tag4).feature('surf1').set('resolution', 'normal')
          ;
383     model.result(tag4).create('surf2', 'Surface');
384     model.result(tag4).feature('surf2').set('expr', 'w');
385     model.result(tag4).feature('surf2').label('Displacement Z');
386     model.result(tag4).feature('surf2').set('const', {'solid.
          refpntr' '0' 'Reference point for moment computation, r
          coordinate'; 'solid.refpntphi' '0' 'Reference point for
          moment computation, phi coordinate'; 'solid.refpntz' '0' '
          Reference point for moment computation, z coordinate'});
387     model.result(tag4).feature('surf2').set('resolution', 'normal')
          ;
388     if n < iterations
389         model.result(tag4).setIndex('looplevel', level_1, 0);
390     else
391         model.result(tag4).setIndex('looplevel', 'interp', 0);
392     end
393     model.result(tag4).run;
394     %Export r-displacement of all the layers for t=last
395     tag5 = model.result.export.uniquetag('plot');
396     model.result.export.create(tag5, tag4, 'surf1', 'Plot');
```

```
397     exp_filenamerD = sprintf('%s_%d.txt',[path,'r_disp'],n)
398     model.result.export(tag5).set('filename', exp_filenamerD);
399     model.result.export(tag5).run;
400     %Export z-displacement of all the layers for t=last
401     tag6 = model.result.export.uniquetag('plot');
402     model.result.export.create(tag6, tag4, 'surf2', 'Plot');
403     exp_filenamezD = sprintf('%s_%d.txt',[path,'z_disp'],n)
404     model.result.export(tag6).set('filename', exp_filenamezD);
405     model.result.export(tag6).run;
406
407     %von Mises stress (pg3)
408     tag7 = model.result.uniquetag('pg');
409     model.result.create(tag7, 'PlotGroup2D');
410     model.result(tag7).create('surf1', 'Surface');
411     model.result(tag7).feature('surf1').set('expr', 'solid.mises');
412     model.result(tag7).feature('surf1').set('descr', 'von Mises
            stress');
413     model.result(tag7).feature('surf1').set('unit', 'MPa');
414     if n < iterations
415        model.result(tag7).setIndex('looplevel', level_1, 0);
416     else
417        model.result(tag7).setIndex('looplevel', 'interp', 0);
418     %Export von Mises stresses of the final part for t=last
419     tag8 = model.result.export.uniquetag('plot');
420     model.result.export.create(tag8, tag7, 'surf1', 'Plot');
421     exp_filenamevM = sprintf('%s_%d.txt',[path,'vM_stresses'],n)
422     model.result.export(tag8).set('filename', exp_filenamevM);
423     model.result.export(tag8).run;
424     end
425     model.result(tag7).feature('surf1').create('def1', 'Deform');
426     model.result(tag7).feature('surf1').create('filt1', 'Filter');
427     model.result(tag7).feature('surf1').feature('filt1').set('expr'
            , 'solid.isactive');
428     model.result(tag7).run;
```

```
429
430     %Plots
431     if rem(n,100) == 0
432         figure(1)
433         subplot(sp_1,sp_2,nn)
434         mphgeom(model,'geom1','edgelabels','on')
435         drawnow
436         figure(2)
437         subplot(sp_1,sp_2,nn)
438         mphplot(model,'pg1','rangenum',1)
439         drawnow
440         figure(3)
441         subplot(sp_1,sp_2,nn)
442         mphplot(model,'pg2','rangenum',1)
443         drawnow
444         figure(4)
445         subplot(sp_1,sp_2,nn)
446         mphplot(model,'pg3','rangenum',1)
447         drawnow
448         nn=nn+1;
449     end
450     fprintf('End of n=%d\n',n)
451 end
452 mphshowerrors(model)
453 toc
454 out = model;
```

Appendix C

Fatigue Results

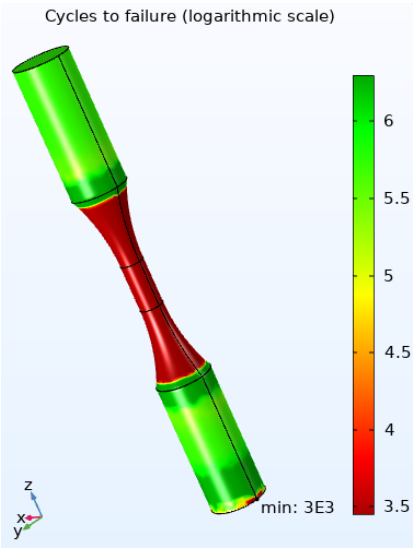

(a) Load1.

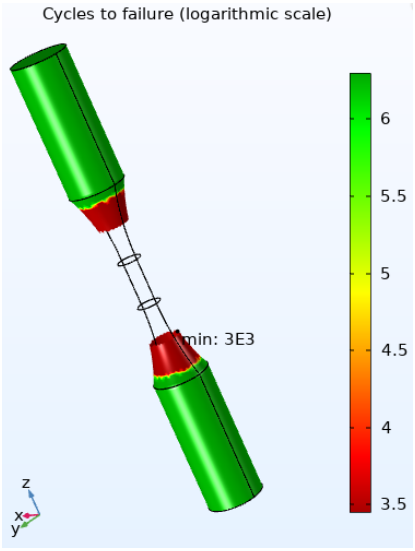

(b) Load2.

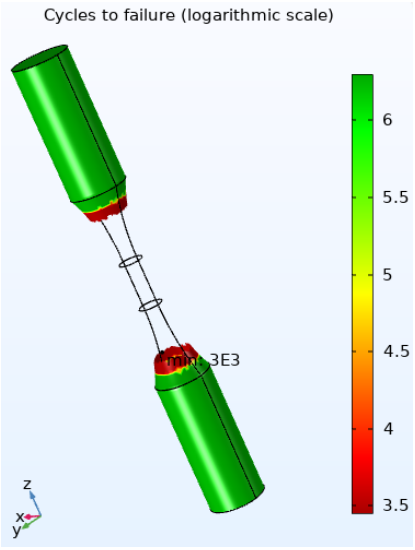

(c) Load3.

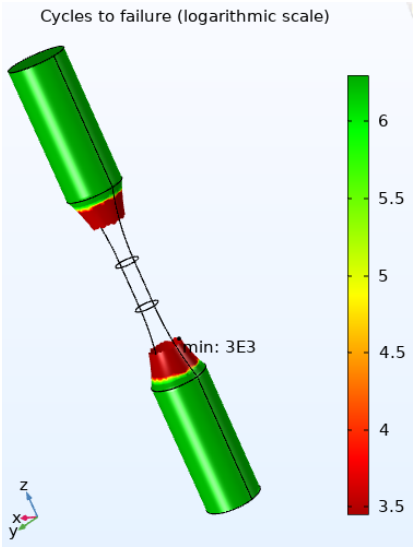

(d) Load4.

Figure C.1: Cycles to failure for each cyclic loading. [The middle part of the dog-bone cylinder lacks colour contour because the stress amplitude witnessed in that area exceeds the stresses defined by the S-N curves.]